A STUDY OF SHOCK ANALYSIS USING THE FINITE ELEMENT METHOD VERIFIED WITH EULER-BERNOULLI BEAM THEORY; MECHANICAL EFFECTS DUE TO PULSE WIDTH VARIATION OF SHOCK INPUTS; AND EVALUATION OF SHOCK RESPONSE OF A MIXED FLOW FAN

A Thesis

presented to

the Faculty of California Polytechnic State University,

San Luis Obispo

In Partial Fulfillment

of the Requirements for the Degree

Master of Science in Mechanical Engineering

by

David Jonathan González Campos

July 2014

COMMITTEE MEMBERSHIP

TITLE:	A Study Of Shock Analysis Using The Finite Element Method Verified With Euler-Bernoulli Beam Theory; Mechanical Effects Due To Pulse Width Variation Of Shock Inputs; And Evaluation Of Shock Response Of A Mixed Flow Fan
AUTHOR:	David Jonathan González Campos
DATE SUBMITTED:	July 2014
COMMITTEE CHAIR:	Xi Wu, PhD Associate Professor of Mechanical Engineering
COMMITTEE MEMBER:	James Meagher, PhD Professor of Mechanical Engineering
COMMITTEE MEMBER:	Hemanth Porumamilla, PhD Associate Professor of Mechanical Engineering

ABSTRACT

A Study Of Shock Analysis Using The Finite Element Method Verified With Euler-Bernoulli Beam Theory; Mechanical Effects Due To Pulse Width Variation Of Shock Inputs; And Evaluation Of Shock Response Of A Mixed Flow Fan

David Jonathan González Campos

For many engineers that use finite element analysis or FEA, it is very important to know how to properly model and obtain accurate solutions for complicated loading conditions such as shock loading. Transient acceleration loads, such as shocks, are not as common as static loads. Analyzing these types of problems is less understood, which is the basis for this study. FEA solutions are verified using classical theory, as well as experimental results. The complex loading combination of shock and high speed rotation is also studied. Ansys and its graphic user interface, Workbench Version 14.5, are the programs used to solve these types of problems. Classical theory and Matlab codes, as well as experimental results, are used to verify finite element solutions for a simple structure, such as a cantilevered beam. The discrepancy of these FEA results is found to be 2.3%. The Full Method and the Mode Superposition Method in Ansys are found to be great solution tools for shock loading conditions, including complex acceleration and force conditions. The Full Method requires less pre-processing but solutions could take days, as opposed to hours, to complete in comparison with the Mode Superposition Method, depending on the 3D Model. The Mode Superposition Method requires more time and input by the user but solves relatively quickly. Furthermore, a new representation of critical pulse width of the shock inputs is presented. Experimental and finite element analyses of a complete mixed flow fan undergoing ballistic shock is also completed; deformation results due to shock loading, combined with rotation and aerodynamic loading, account for 32.3% of the total deformation seen from experimental testing. Solution methods incorporated in Ansys, and validation of FEA results using theory, have great potential implications as powerful tools for engineering students and practicing engineers.

Keywords: shock analysis, impulse analysis, dynamic response, finite element analysis (FEA), ansys workbench, shock experiment, deformation, impeller, acceleration, pulse width, 3d model.

ACKNOWLEDGMENTS

I would like to express my gratitude to Dr. Patrick Lawless, VP of Engineering and Production at Xcelaero Corporation, for his valuable support which made this research possible. I would like to thank Sean Harvey, Lead Technical Services Engineer at ANSYS, Inc., for his continuous assistance with ANSYS models. I would also like to thank my graduate coordinator, Dr. Xi Wu, for her patience, encouragement and mentorship throughout my graduate studies at California Polytechnic State University, San Luis Obispo. I would like to express my special appreciation and thanks to my parents for instilling in me a sense of perseverance and to my wife for her amazing support throughout my graduate work.

TABLE OF CONTENTS

Page

LIST OF TABLES

LIST OF FIGURES

NOMENCLATURE

Symbol/Abbreviation	Description
A	Cross section of the beam
A_n	A constant
B_n	A constant
C	A constant
D	Diameter
E	Young's modulus of elasticity
Hz	Hertz
Gpa	Gigapascal
I	Bending moment of inertia
M	Bending moment
N	Newtons
P	Concentrated load
R	Radius
T	Thickness of the beam
Y(x)	Displacement in space
W(t)	Displacement in time
V	Shear force
EI	Flexural rigidity or bending stiffness
CG	Center of gravity
FEA	Finite element analysis

FBH	Front bearing housing
GB	Gigabytes
IGV	Inlet guide vanes
LE	Leading edges
OD	Outside diameter
P	Normal force
P_0	Contact pressure
NSK	A bearing manufacturer
RPM	Revolution per minute
RAM	Random access memory
TE	Trailing edges
TMA	Time to maximum acceleration
V	V equation, explicit
W	Watts
a	Radius of contact
e	Natural log
f_n	Natural frequency
g	Gravity
in	Inches
l	Length of the cantilevered beam
lbf	Pound force
m	Mass, Meters
m_l	Mass per unit length

m_t	Total mass
mm	Millimeter
ms	Milliseconds
t	Time
tan	Tangent
cos	Cosine
cosh	Hyperbolic cosine
psi	Pounds per square inch
sin	Sine
sinh	Hyperbolic sine
w	Width of the beam
β	A constant
Δ	Delta equation, explicit
θ	Angle theta
ρ	Density
ρ_c	Radius of curvature
ε	Strain
σ	Stress
κ	Curvature of the beam
ν	Poisson's ratio
α	Deflection
ω_n	Circular natural frequency

CHAPTER 1

INTRODUCTION TO THE STUDY

1.1 Problem Formulation

Shocks are a prevalent loading condition that occur every day and affect simple mechanical parts, complete mechanical assemblies such as military tanks, commercial products, and even humans. Engineers use tools such as finite element modeling to analyze complex parts and assemblies. More validation of analyses with experiments are necesary to master the solution process of these complicated problems.

1.2 Purpose of the Study

The purposes of this study are to analyze shock loading using finite elements, validate the process and results using simple and continuous structures, investigate the mechanical effects due to variation pulse width in the acceleration input, and complete a transient analysis of a mixed flow fan undergoing ballistic shock using knowledge gained from analyses of a simple continuous structure.

The shock input is a half sine acceleration excitation; this type of input is very representative of impulse loading for structures undergoing shocks such as those mentioned above; other inputs also used for modeling real life shocks include "the decaying sinusoidal acceleration, and the complex oscillatory-type motion [16]."

1.3 Limitations of the Study

Theoretical and finite element analysis were conducted at standard ambient conditions and using constant isotropic material properties. Mechanical effects of shock loading for the mixed flow fan are compared in terms of radial and axial deformations that would cause total closure of the impeller tip clearance.

1.4 Literature Review

An extensive amount of sources were reviewed for the completion of this study on shock loading; for brevity, only the most prominent sources are included in this literature review. The areas that these sources cover include, but are not limited to, background information on shock loading, theory and governing equations for basic structures such as cantilivered beams, experiments involving natural frequencies and acceleration inputs, finite element modeling using Ansys Workbench, and Hertz contact theory and analysis. Understanding shock loading and modeling this condition using finite elements was accomplished by learning to solve the governing equations of basic structures such as beams, validating results with experimental data, and running FE models of simple and complex structures.

In " Euler-Bernoulli Beams" [5] Terje Haukaas derives the governing beam differential equation for Euler-Bernoulli type beams using equilibrium and section integration, material law, and kinematics. In "Vibrations of Cantilever Beam, Deflection, Frequency, and Research Uses" [7] Scott Whitney clearly states the steps to arrive at the general solution of the beam equation for a cantilevered beam. These are the primary sources for deriving and solving the governing beam equation. These provide natural frequencies and mode shapes of cantilevered beams which are compared to experimental solutions.

In "Forced Vibration of a Cantilever Beam" [4] C. E. Repetto, *et. al*, present modal experimental results for a 0.50 m long PVC beam that is held vertically, and excited by a wave driver; the transverse natural frequencies are measured to be $\omega = 7.79, 36.44, 97.39,$ and $185.35\ s^{-1}$. Except for the fundamental frequency which was influenced significantly by gravity effects and damping, these results were found to be within 9% error compared to their theoretical results and within 10% error when compared to the theoretical results in this report. In this experiment, using a ferrous metal would have eliminated any damping that occurs with the PVC material and would have simplified the experimental and

analytical comparisons. The same Euler-Bernoulli governing differential equations are used in the dynamic solution of beams undergoing forced vibration, specifically shock loading.

In "Stress, Strain, and Structural Dynamics: An Interactive Handbook of Formulas, Solutions, and Matlab Toolboxes" [12] Bingen Yang provides a program for the dynamic analysis of beams; he explains how to set up beam types, boundary and initial conditions, damping, response time, and output control. The program can solve for mode shapes of Euler-Bernoulli beams; it can solve for the beam's response in time and space as well as its internal forces. Modal damping can also be specified to filter out higher frequencies in the response. Input of external forces is also possible using this program. Static analysis of Euler-Bernoulli beams is also covered which provides useful background information prior to evaluating dynamic analysis. The governing equations and analytical solution derivations are also included. The theoretical response for a cantilevered beam undergoing shock is obtained; the finite element analysis of the same model, as presented in this report, closely matches the theoretical reponse. This resource is extremely valuable in validating the FEA cantilevered beam model and is the basis for analyzing comlex parts and assemblies. One of these assemblies is a glass panel and steel fork assembly.

In "Finite Element Simulations with ANSYS Workbench 14" [1] Huei-Huang Lee presents an Ansys tutorial based on a glass planel and lifting fork which provided the basic knowledge for FEA transient analysis of shock loading of this system. When the glass panel is moved up or down with accelerations of approximately 4 g, the tips of the glass panel deflect for some amount of time; for this system it is important to know when the deflections have decayed so the glass panel can be inserted into the processing machine. Every step is carefully detailed from beginning to end including screen shots of each step. Geometry and material properties for the glass panel and the steel fork are provided. The contact is specified as bonded, the glass is mapped meshed and the steel fork is meshed with a thin sweep using solid shell elements. Step controls, damping, boundary conditions, initial conditions, and post-processing are also clearly described. This source provides an excellent introduction for modeling shock loading using finite

elements. FEA analysis using Ansys proves to be a very capable tool for shock analysis even at the assembly and subassembly levels. A subassembly that was difficult to analyze was the ball bearing.

In "Fundamentals of Machine Component Design" [18] Robert Juvinal and Kurt Marshek present the Hertz contact theory for curved surfaces such as bearings where finite contact points and lines exist. Very high contact stresses can develop in these areas and often times it involves a cyclic type loading where loading and unloading occurs with high frequency. Surface fatigue develops and eventually leads to fatigue failure. The authors describe the applicable equations in term of Poisson's ratio, Young modulus, and radii of the applicable parts. The assumptions that apply are listed as well as the type of stresses involved on the surfaces as well as beneath them. Other factors to consider are also discussed such as thermal expantion and hydrodynamic pressure. However, it is necessary to find information on deflection formulas in other sources.

Understanding shock loading and modeling this condition using finite elements is accomplished by learning to solve the governing equations of basic structures such as beams, validating results with experimental data, and running FE models of simple and complex structures. Experimental data was found for a cantilevered beam; this was analyzed and compared to theoretical results. Then a test case involving a glass panel exposed all the different parts of modeling complex structrues using an FEA code such as Ansys Workbench. A mixed flow machine is the largest and most complex assembly analyzed with finite elements; Hertz contact theory is also used to analyze complex components such as ball bearings. Every reference is vital in building the knowledge base and tools for understanding and solving engineering problems involving shock loading.

CHAPTER 2

PREVALENCE OF SHOCK LOADING AND THE EULER-BERNOULLI THEORY

2.1 Background

Mechanical shocks are a very common occurrence in everyday life; examples of shock loading include explosions, car hitting a pothole, reciprocating engine fuel explosions inside cylinders, airplane landing, bolted joints suddenly opening and closing with an impact, high winds can be a source of step loading, earthquakes, drop impact during handling, g forces generated for internal components, high speed fluid entry, etc. "When the load increases to its maximum value over five or six natural periods, it is a quasi-static load. When it does so over a fraction of the period, it is a shock loading. Broader definitions exist, where anything with up to two periods duration is a shock loading [2]."

Figure 1. Ballistic Shock [20].

Shock analysis has become a requirement with specific customer guidelines to follow during the design process as well as in the testing qualification phase of products in many industries, including high performance cooling fans, which is the basis of the last chapter in this report. Thus it is important in the preliminary and critical design phase to appropriately run analytical and finite element models that predict safe operation of these machines. In the qualification phase, specific high level shocks are applied; it is crucial that all components inside the machine withstand these shocks and continue to function satisfactorily and safely. Shock levels inside military aircraft and vehicles are related to human tolerance for acceleration changes. In 1955, Col. John Stapp determined that a person can survive a deceleration of 46.2 g in 1.4 seconds [21]. For acceleration levels of up to 50 g, the input duration should not be any more than 50 ms, otherwise severe injury can occur [22]. This could be one of the limiting factors and the reason why only shocks of low magnitude are allowed inside the crew compartment of military vehicles.

A possible mechanical effect during shock loading is that an impeller or wheel tip deflection is such that it collides with its inlet or inlet shroud for any type of fan or rotating machinery with tight tip clearances. Figure 2 shows a vane axial fan with a tight clearance between the rotating and stationary components. This collision must be prevented to avoid any risk of impeller blade rupture. The dynamics of the rotor and shroud response must be carefully understood to properly design all components while making the right compromises between materials, wall thickness, weight, design features, etc.

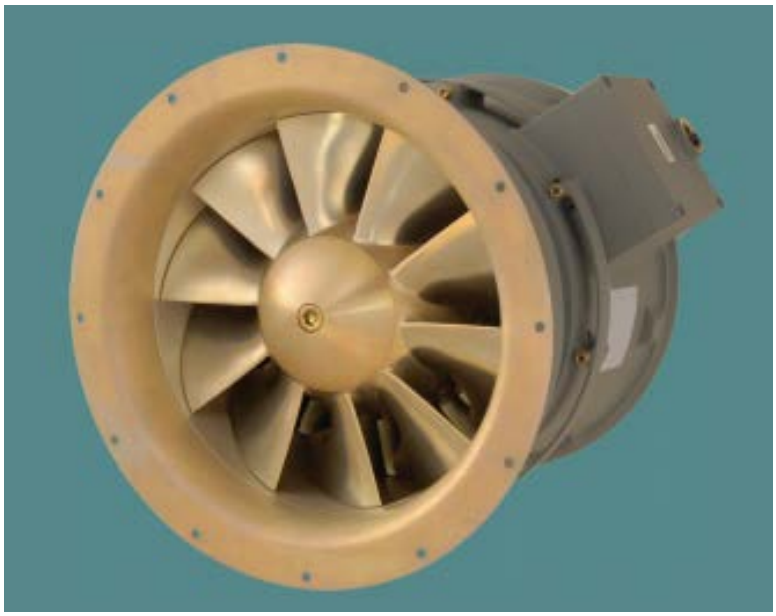

Figure 2. Cyclone 100 Fan by Xcelaero Corporation.

In Section 2.2, equations for the vibration response of a beam are presented and derived. The intention is to use classical theory to solve for the shock response of a cantilevered beam; assumptions are later made to model impeller blades as cantilevered beams. Chapter 3 includes modal and shock analyses for a cantilevered beam using theory, experiment, and the finite element method. In this section, the finite element process is validated by comparing FEA results on a simple structure, to experimental results, and as well as theoretical results from classical beam theory. The desktop computer used to run finite element analyses is equipped with a quad core processor with four physical cores, 18 GB of RAM memory, and a SATA2 7200 RPM hard drive. The FEA program used is Ansys Version 14.5.

In Chapter 4, case studies for shock loading are presented in order to better understand several factors associated with shock response of mechanical systems as modeled in Ansys. These case studies are Glass Panel Undergoing a 4 g Acceleration, The I508 Inlet Guide Vane Housing subjected to 40 g acceleration, and Baseline Impeller Shock Analysis sustaining a 50 g axial impulse loading. Using these case studies, many shock scenarios are modeled and evaluated; comparisons between the Full Method and the Mode Superposition Method solutions are carried

out. The sensitivity studies conducted include using static analysis in place of transient analysis, effectiveness of modeling impeller blades as cantilevered beams, and effects of varying pulse widths of the acceleration input. Finally, in Chapter 5, lessons learned in Chapters 2, 3, and 4 are put into practice in the evaluation of shock loading for a mixed flow fan subjected to a maximum shock of 50 g. Damping effects are neglected in all structural cases considered except in the Glass Panel Case.

2.2 Cantilevered Beam Theory

Static and dynamic response of impeller blades can be modeled as cantilevered beams; the theory of vibration response associated with these types of beams is explored in this section. Figure 3 shows an isometric view of an impeller blade where it shows similar boundary conditions as cantilevered beams. This section presents a derivation description for the formulas that describe the static and dynamic behavior of these types of beams.

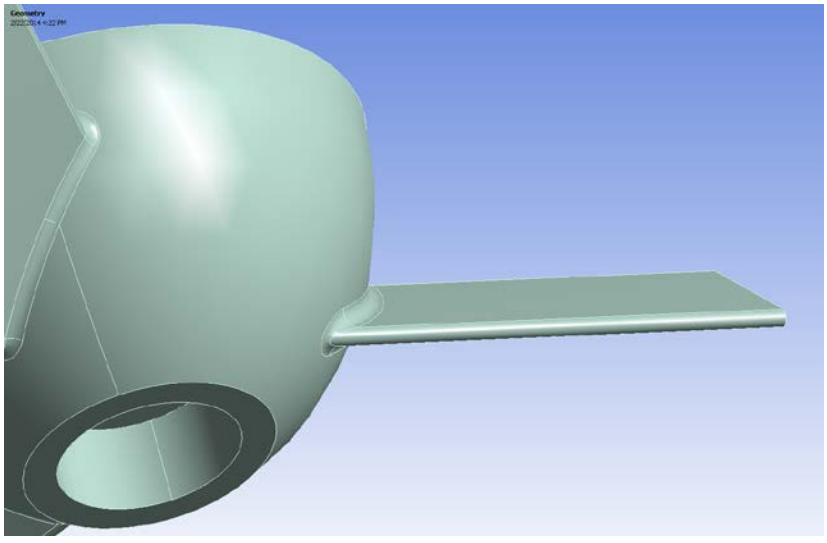

Figure 3. Impeller Blades have similar properties as Cantilevered Beams.

When determining natural frequencies, the "Timoshenko model should be employed for beams and frequencies for which the thickness to length ratio is larger than 10%. Such beams are called stocky beams, while the beams for which the Euler-Bernoulli model is sufficient are called slender ones [9]". Thus it is considered a slender beam if the length is at least ten times the thickness. For slender beams it is acceptable to neglect rotational inertia.

Assumptions:

- Material is homogeneous, isotropic, obeys Hooks Law, and the beam is straight and of uniform cross section.
- "Plane sections remain plane and perpendicular to the neutral axis" [5]. Deformations due to bending are much larger than those due to shear, thus shear deformation effects are neglected [10].
- Deformations are small, $\tan(\theta) \approx \theta$; the beam undergoes small deflections [10].
- Inertia and cross sectional area are constant [7].
- Plane sections perpendicular to the centroidal axis remain plane after deformation [8].
- The motion is purely translational in the vertical direction.
- Rotational Inertia of beam elements is negligibly small compared to translational inertia.

Mathematically, the curvature of the beam undergoing deflection due to an end load can be defined as:

$$\kappa = \frac{1}{\rho_c} \qquad \text{(Eq.1)}$$

In Cartesian coordinates, and as defined in Figure 4, curvature can be approximated as:

$$\kappa \approx \frac{d_\theta}{dx} \qquad \text{(Eq.2)}$$

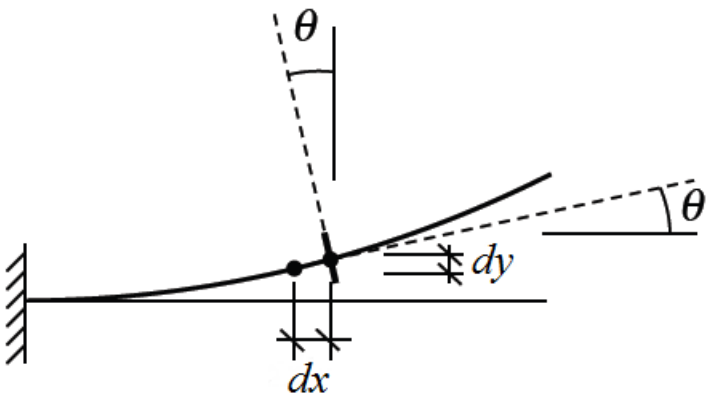

Figure 4. Cantilevered Beam Curvature [5].

This is an approximation, since for a true curvature definition, differentiation should be relative to an axis that "follows the curving beam axis" [5], the tangent of angle θ, is:

$$\tan(\theta) = \frac{dy}{dx} \approx \theta \tag{Eq.3}$$

For small angles, $\tan(\theta) \approx \theta$, so differentiating relative to x is approximately,

$$\frac{d\theta}{dx} \approx \frac{d^2y}{dx^2} \tag{Eq.4}$$

Thus, curvature can be approximated as:

$$\kappa \approx \frac{d^2y}{dx^2} \tag{Eq.5}$$

A more involved approach would involve differentiating the inverse tangent function:

$$\theta = \tan^{-1}\left(\frac{dy}{dx}\right) \tag{Eq.6}$$

Providing,

$$\frac{d_\theta}{dx} = \frac{\frac{d^2y}{dx^2}}{\left(1+\left(\frac{dy}{dx}\right)^2\right)} \tag{Eq.7}$$

When the curvature of the beam is small, $\frac{dy}{dx}$ is small and $\frac{d_\theta}{dx}$ can be approximated as shown in equation (Eq.4), "from mathematics, the exact curvature expression for the exact curvature is" [5]:

$$\kappa \approx \frac{d_\theta}{dx} = \frac{\frac{d^2y}{dx^2}}{\left(1+\left(\frac{dy}{dx}\right)^2\right)^{3/2}} \quad \text{(Eq.8)}$$

Where ρ_c is the beam's radius of the curvature,

$$\varepsilon_x = \frac{y}{\rho_c} \quad \text{(Eq.9)}$$

Per Hook's Law and linear elastic theory:

$$\sigma_x = E\grave{o}_x \quad \text{(Eq.10)}$$

Combining equations (Eq.8), (Eq.9) and (Eq.10):

$$\frac{\sigma_x}{E} = \frac{y}{\rho_c} = y\kappa \quad \text{(Eq.11)}$$

Re-arranging,

$$\kappa = \frac{\sigma_x}{yE} \quad \text{(Eq.12)}$$

From beam theory,

$$\sigma_x = \frac{My}{I} \quad \text{(Eq.13)}$$

Substituting equation (Eq.13) into equation (Eq.12):

$$\kappa = \frac{My}{I}\frac{1}{yE} \quad \text{(Eq.14)}$$

After canceling terms:

$$\kappa = \frac{M}{EI} \tag{Eq.15}$$

Substituting equation (Eq.5) into equation (Eq.15):

$$M = EI\frac{d^2y}{dx^2} \tag{Eq.16}$$

From equilibrium and section integration of a differential section of a loaded beam, the resultant shear force can be defined as the second derivative of the moment in space:

$$\frac{d^2M}{dx^2} = EI\frac{d^4y}{dx^4} \tag{Eq.17}$$

The differential equation that describes the dynamic transverse forced behavior of a cantilevered beam is:

$$m\frac{\partial^2 y}{\partial t^2} + EI\frac{\partial^4 y}{\partial x^4} = f\left(x,t\right) \tag{Eq.18}$$

Equation (Eq.18) above is solved by separation of variables, and using a new set of variables Y and W for clarity,

$$y(x,t) = Y(x)W(t) \tag{Eq.19}$$

Let us solve equation (Eq.18) for a cantilevered beam undergoing free vibration, $f\left(x,t\right) = 0$, thus equation (Eq.18), simplifies to:

$$m\frac{\partial^2 y}{\partial t^2} + EI\frac{\partial^4 y}{\partial x^4} = 0 \tag{Eq.20}$$

Equation (Eq.20) becomes:

$$-m\frac{\partial^2 y(x,t)}{\partial t^2} = EI\frac{\partial^4 y(x,t)}{\partial x^4} \tag{Eq.21}$$

$$-m\frac{\partial^2 (Y(x)W(t))}{\partial t^2} = EI\frac{\partial^4 (Y(x)W(t))}{\partial x^4} \tag{Eq.22}$$

Dividing (Eq.22) by Y(x)W(t) ,

$$-\frac{1}{W(t)}\frac{\partial^2 W(t)}{\partial t^2}=\frac{EI}{mY(x)}\frac{\partial^4 Y(x)}{\partial x^4} \qquad \text{(Eq.23)}$$

Let's define the natural circular frequency as:

$$\omega_n^2=\frac{EI}{m} \qquad \text{(Eq.24)}$$

Both the left and right side of equation (Eq.23) are independent of each other; the left side is differentiated in time and becomes equal to a constant; in a similar way the right side is differentiated in space and equals a constant. "Because each side equals a constant, [equation (Eq.23)] is valid and the method of separation of variables can be used. Let this constant be denoted ω_n^2 "

Defining,

$$\beta^4=\frac{\omega_n^2 m}{EI} \qquad \text{(Eq.25)}$$

When separation of variables is applied, equation (Eq.23), which is a fourth order differential equation, becomes two ordinary differential equations [23]. Equation (Eq.23) and in conjunction with (Eq.25) become:

$$\frac{d^4 Y}{dx^4}-\beta Y(x)=0 \qquad \text{(Eq.26)}$$

And

$$\frac{d^2 W(t)}{dt^2}+\omega_n^2 W(t)=0 \qquad \text{(Eq.27)}$$

Deflection mode shapes are found by solving equations above and using appropriate boundary conditions for a cantilevered beam; such boundary conditions are:

At the clamped end, $y(0)=0$, $\frac{d}{d_x}y(0)=0$ (Eq.28)

At the free end, $$M(\mathrm{l}) = EI\frac{d^2}{dx^2}y(\mathrm{l}) = 0\ ,\quad \mathrm{V}(\mathrm{l}) = EI\frac{d^3}{dx^3}y(\mathrm{l}) = 0 \qquad \text{(Eq.29)}$$

The general solutions for equations (Eq.26) and (Eq.27) are "linear combinations of trigonometric equations" [6, 7]:

$$Y(x) = C_1[\cos(\beta x) + \cosh(\beta x)] + C_2[\cos(\beta x) - \cosh(\beta x)] + C_3[\sin(\beta x) + \sinh(\beta x)] + C_4[\sin(\beta x) - \sinh(\beta x)] \qquad \text{(Eq.30)}$$

$$W(t) = C_5(\sin(\omega t) + C_6\cos(\omega t) \qquad \text{(Eq.31)}$$

After applying boundary conditions to equation (Eq.30) and its derivatives

$$\frac{dY}{dx},\ \frac{d^2Y}{dx^2},\ \text{and}\ \frac{d^3Y}{dx^3} \qquad \text{(Eq.32)}$$

We are able to solve for the C coefficients,

from $$y(0) = 0\ ,\ C_1 = 0 \qquad \text{(Eq.33)}$$

from $$\frac{dy}{dx} = 0\ ,\ \ C_3 = 0 \qquad \text{(Eq.34)}$$

(Eq.30), (Eq.33), and (Eq.34) can be combined, and solved for C_4:

$$C_4 = C_2\frac{-\cos(\beta l) - \cosh(\beta l)}{\sin(\beta l) + \sinh(\beta l)} \qquad \text{(Eq.35)}$$

Combining (Eq.30) and (Eq.35), we obtain:

$$Y(\mathrm{x}) = C_2\{[\cos(\beta x) - \cosh(\beta\,\mathrm{x}] + [\frac{-\cos(\beta l) - \cosh(\beta l)}{\sin(\beta l) + \sinh(\beta l)}][\sin(\beta\,\mathrm{x}) - \sinh(\beta\,\mathrm{x})]\} \qquad \text{(Eq.36)}$$

"in order for the dynamic solution for the displacement to be equal to the static solution, at t=0, C2 must be equal to 1/2.

$$C_2 = \frac{1}{2} \qquad \text{(Eq.37)}$$

Using this value of C_2 in equation (Eq.36), we obtain:

$$Y(0) = 0 \text{ and } Y(l) = -1 \qquad \text{(Eq.38)}$$

Combining equation (Eq.35) with $\frac{d^2Y}{dx^2}$ or $\frac{d^3Y}{dx^3}$, and substituting the trigonometric identities:

$\sin^2 + \cos^2 = 1$ and $\cosh^2 - \sinh^2 = 1$, provide:

$$\cos(\beta l)\cosh(\beta l) = -1 \qquad \text{(Eq.39)}$$

Which is "the frequency equation for a cantilever beam" [7].

This nonlinear equation (Eq.39) "must be solved numerically to determine allowable values of βl, there are an infinite number of solutions corresponding to the possible modes of vibration"[24]. "The system has infinite frequencies. It is continuous, and all continuous systems have infinite number of frequencies [6]." Table 1 below shows values of βl for the first four natural frequencies. "These mode shapes are also called eigenfunctions [6]."

Table 1. βl Values

n	βl
1	1.8751
2	4.6940
3	7.8547
4	10.9955

Using βl values in Table 1, we can now solve for circular natural frequencies using the following explicit equation:

$$\omega_n = (\beta l)^2 \sqrt{\frac{EI}{m_l l^3}} = (\beta l)^2 \sqrt{\frac{EI}{\rho A l^3}} \qquad \text{(Eq.40)}$$

Remember that m is mass per unit length in equation (Eq.40); to use total mass, the equivalent equation would be

$$\omega_n = (\beta l)^2 \sqrt{\frac{EI}{m_t l^3}} \qquad \text{(Eq.41)}$$

The formula for converting circular natural frequency into natural frequency in hertz is:

$$f_n = \frac{\omega_n}{2\pi} \qquad \text{(Eq.42)}$$

Furthermore, "for each frequency there exists a characteristic vibration" [7]. Thus in order to determine the beam's response in space and time due to some initial conditions, the following equation can be used:

$$y(x,t) = Y(x)[A_n \cos(\omega_n t) + B_n \sin(\omega_n t)] \qquad \text{(Eq.43)}$$

"Where A_n depends on the initial position at t=0, and B_n depends on the initial velocity [7]." When the beam initial displacement is zero, $B_n = 0$. A_n can be found using the following integral:

$$A_n = \frac{2}{l}\int_0^l (y(x,t=0)\,\mathrm{Y}(x))\,dx \qquad \text{(Eq.44)}$$

Equation (Eq.44) "can be solved analytically by a computer math program" [7], resulting in the following solution for A_n,

$$A_n = \left[\frac{4Pl}{\mathrm{EIm}\beta^4(\sin(\beta l)\mathrm{e}^{\beta l} + \mathrm{e}^{2\beta l} - 1)}\right]\{3\sin(\beta l)(\mathrm{e}^{2\beta L}+1)\text{-}2(\beta l)^3\mathrm{e}^{\beta l} + \cos(\beta l)[3-(\beta l)^3(\mathrm{e}^{2\beta l}+1) - 3\mathrm{e}^{2\beta l}]\} \qquad \text{(Eq.45)}$$

CHAPTER 3

VALIDATION OF ANSYS MODEL USING ANALYTICAL AND EXPERIMENTAL RESULTS FOR SHOCK AND MODAL ANALYSES OF CANTILEVERED BEAMS

"Models based on beam-like elements with different boundary conditions, can be used to simulate the response of structures in engineering applications" [4] such as bridges, cranes, airplane wings, etc. In this section, the finite element process is validated by comparing FEA results on a simple structure and comparing these with theoretical results from classical beam theory. Modal and shock analyses are carried out in this section. Modal Analysis for impeller blades can be approximated using a much simpler structure such as a cantilevered beam; at the very least, solving for the modal solutions for this kind of beam serves as a good initial step towards defining the mode shapes of impeller blades. Theoretical, experimental, and finite element results will be compared and evaluated. Furthermore, shock analysis of a cantilevered beam is also studied and compared to theoretical results; the same approach is later used for analyzing impellers undergoing shock loading.

The cantilevered beam that will be used for comparison purposes is a PVC beam used by Repetto, Roatta, and Welti in 2012 to experimentally determine the mode shapes at low frequencies. A photograph of this beam during the experiment is shown in Figure 5. This same beam is analyzed theoretically also using the finite element method. Its mechanical properties include a Young's modulus of 3.1×10^{9} Pa and a density of 1420 kg/m^3. The beam's length, $l = 0.502$ m, its width, $w = 1.7 \times 10^{-3}$ m, and its thickness, $T = 0.89 \times 10^{-3}$ m [4]. Bending stiffness, EI, calculates to 3.096×10^{-4} N·m^2. The beam is held vertically downward, including a fixed support at the top and free at the bottom end; this helps in minimizing the directionality effect of gravity. The shaker uses a transverse displacement to load the beam at different resonant frequencies. An interesting independent finding by Repetto, Roatta, and Welti is that resonant frequencies for the boundary conditions shown here "increase due to the stiffening effect of the

beams weight" exerting tension in the structure. Likewise, the opposite outcome is true for the beam held in the opposite configuration. Furthermore, the gravitational effect is "found to mainly influence the systems' response to the fundamental frequency of oscillation [4]".

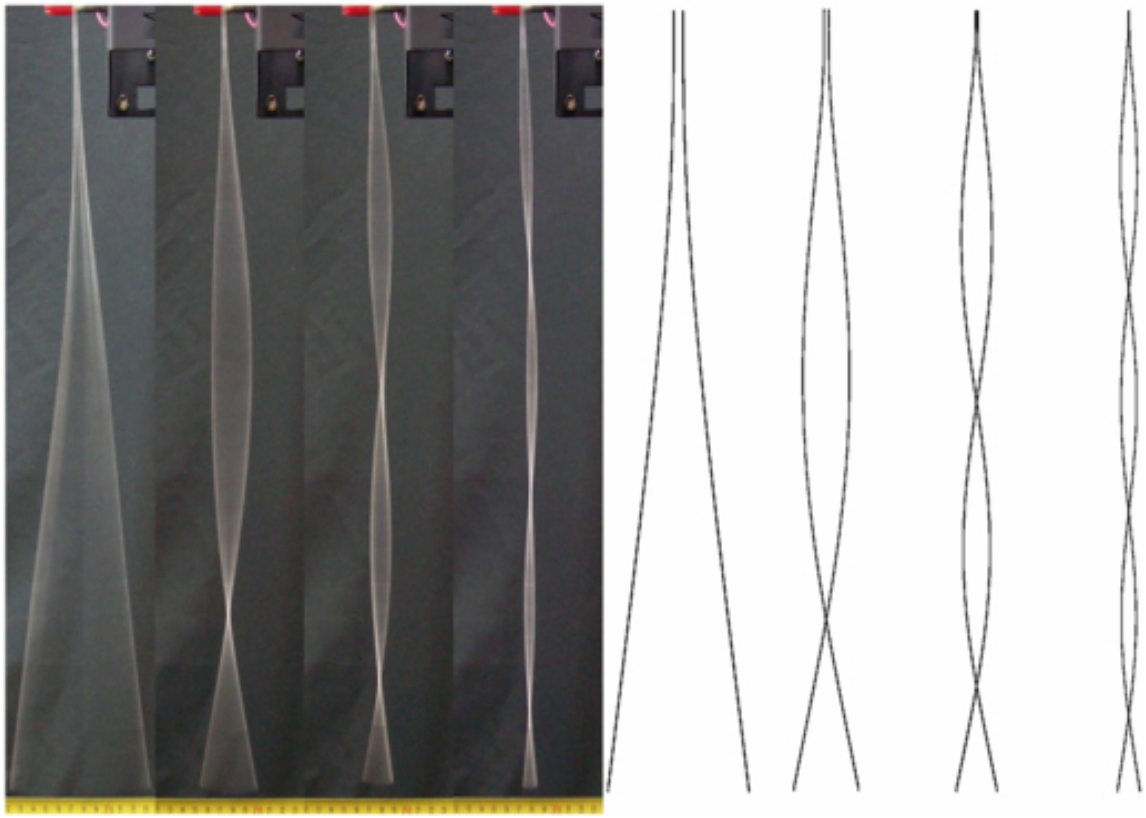

Figure 5. Photograph of the first four resonant frequencies of a PVC Beam used by Repetto, Roatta, and Welti.

3.1 Theoretical Analysis of the PVC Cantilevered Beam

The Euler-Bernoulli beam theory found in the previous section was used to carry out modal analysis of the PVC beam. Results from analysis will be compared to the experimental results. A mathematical code was created in Matlab to solve for the first three eigen values and eigen functions or mode shapes. The core of this program involves solving for equations (Eq. 35) and (Eq. 36) using constants in Table 1. Input values that the code prompts for include the beam's length, width, thickness, modulus of elasticity, and its density. The program uses two FOR loops

to solve for the spatial vertical deflections of the beam as a function of the beam span. Values of the vertical axis are normalized relative to the maximum vertical value calculated for each mode; units for the horizontal axis are meters and the mode frequencies calculated are in hertz. Appendix A includes the Matlab code used to solve and graph the mode shapes of cantilevered beams; results for the PVC beam are included in Figures 6 through 8. This theoretical code has been used successfully in the process of impeller design, to quickly estimate mode shapes of blades, as an efficient preliminary step to study resonance frequencies and construct Campbell diagrams. These theoretical results were also validated using a separate toolbox by Bingen Yang [12].

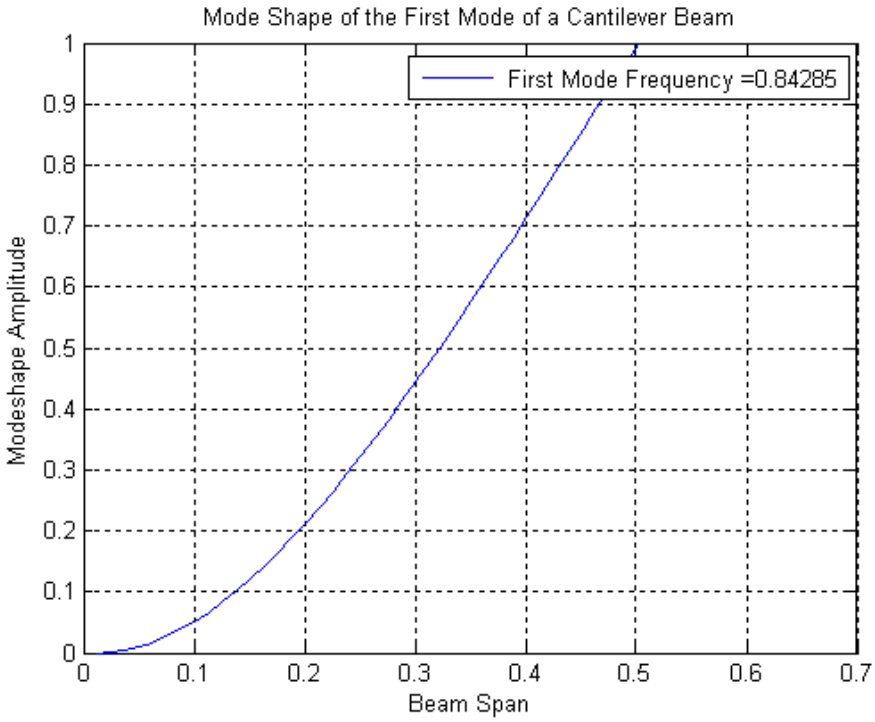

Figure 6. First Mode Shape of the PVC Cantilevered Beam.

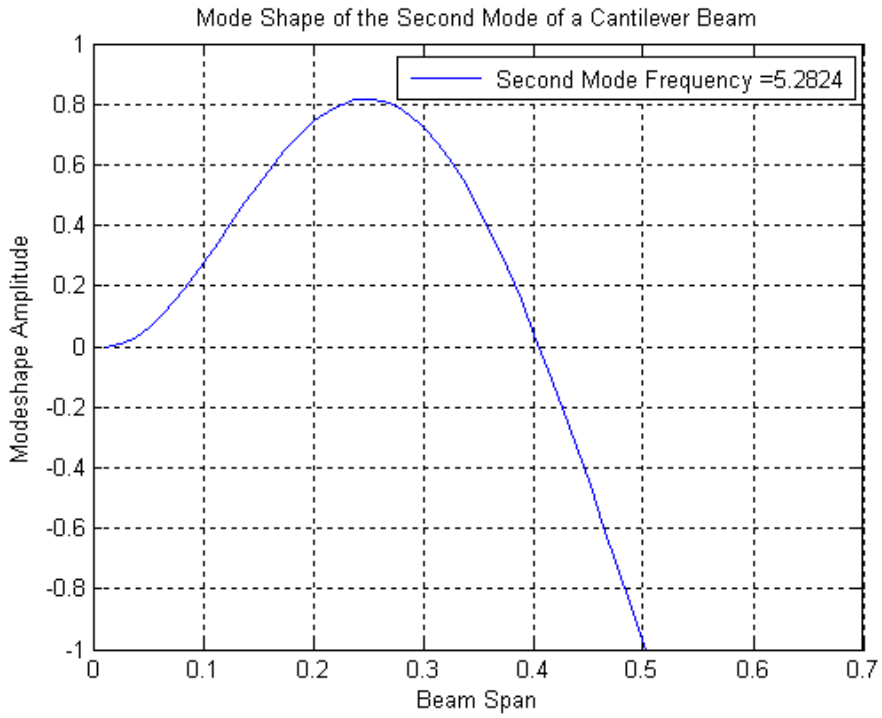

Figure 7. Second Mode Shape of the PVC Cantilevered Beam.

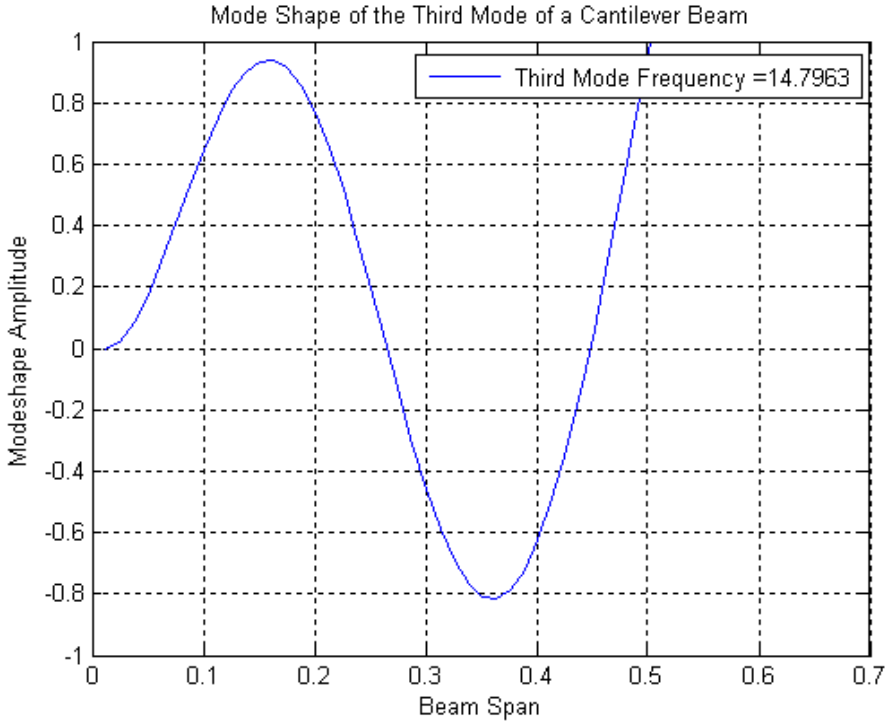

Figure 8. Third Mode Shape of the PVC Cantilevered Beam.

3.2 FEA Analysis of the PVC Cantilevered Beam

FEA results of modal analysis of the PVC beam are included next. Models that are symmetrical across one or more planes sometimes can be divided and reduced to the most elemental form to save computational time. For this case, however, the model is small enough and does not need simplification. Furthermore, using only a section of complete models is not recommended for modal analysis; for instance, deciphering legitimate mode frequencies and mode shapes becomes more involved. The full PVC beam model was used in this modal analysis. The FEA analysis presented here does not take into account the effect of gravity; for this model, it is considered negligible. This FEA model does not include any pre-stressed condition, it includes a native Creo Parametrics model, and the relevant mechanical properties for PVC. Modal results for total deformation are shown in Figures 9 through 11; they include the first in-plane or transverse mode shapes and frequencies. These are also compared to experimental and analytical results in Table 2.

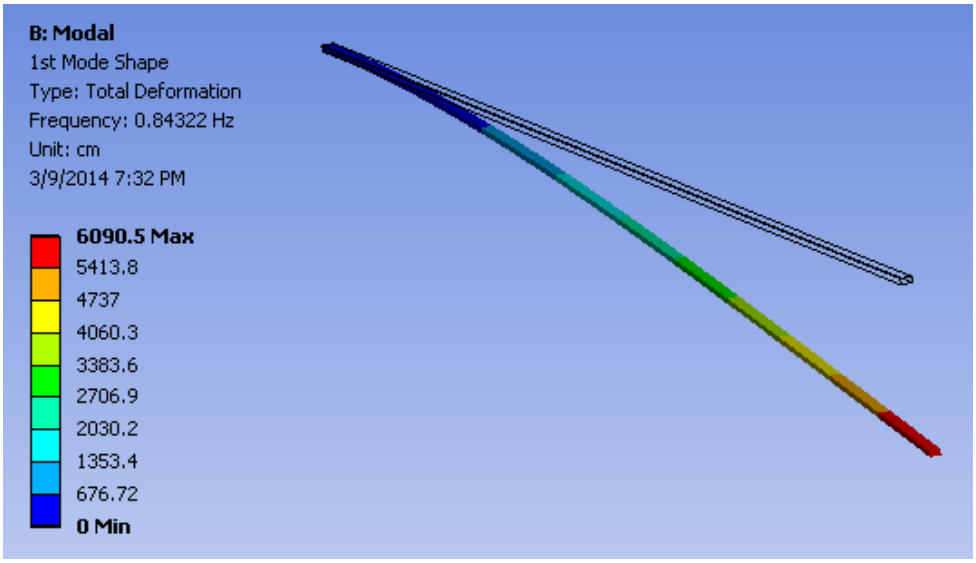

Figure 9. First Mode Shape of the PVC Cantilevered Beam, FEA Model.

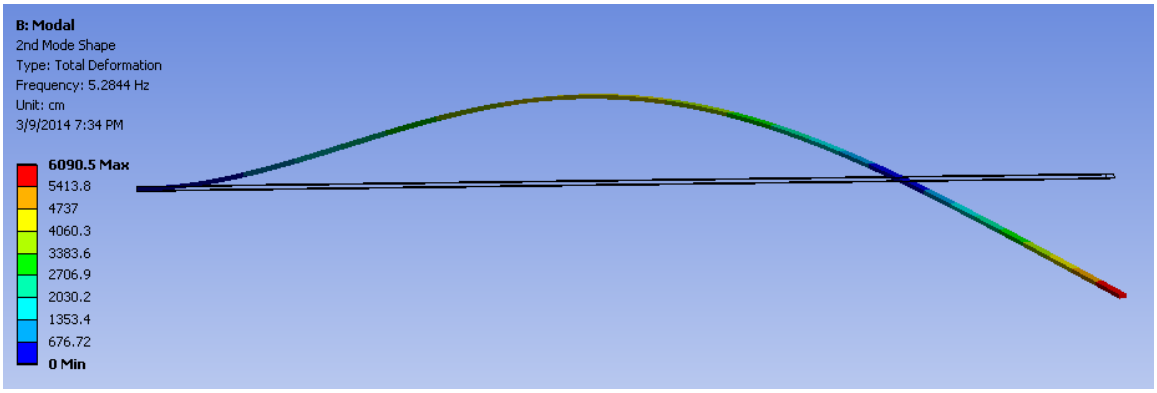

Figure 10. Second Mode Shape of the PVC Cantilevered Beam, FEA Model.

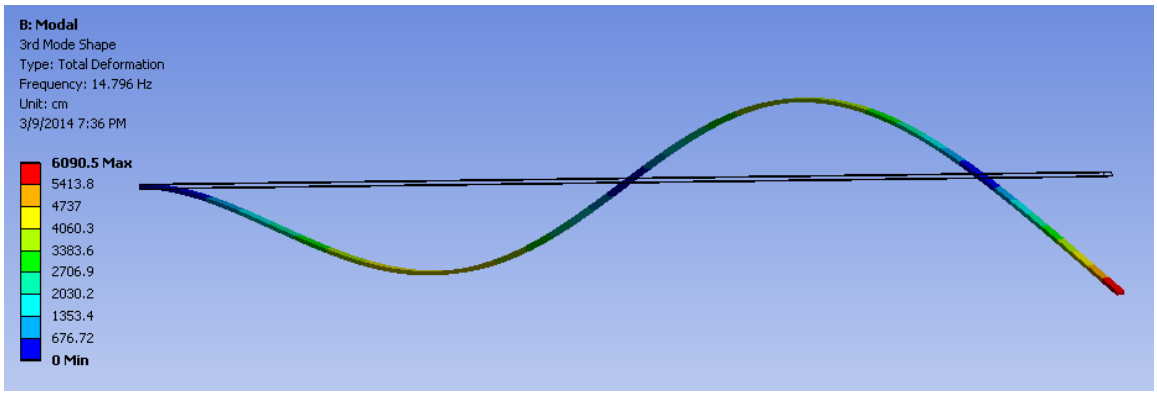

Figure 11. Third Mode Shape of the PVC Cantilevered Beam, FEA Model.

Table 2 includes a comparison between experimental results and theoretical values; the second and third mode frequencies have less than 10% error. However, the fundamental frequency has a discrepancy that is quite large; a probable cause could be that the deflection due to gravity could be stiffening the beam and increasing its first resonance frequency, thereby showing more sensitivity to gravity than the others.

Table 2. Comparison of Mode Shape Results By Different Methods.

Modes Shapes	Repetto, Roatta, Welti Experiment	Theoretical Results 1 Matlab	Theoretical Results 2 Yang's Matlab Toolbox	FEA Results	Experimental Results Relative to Theoretical Results 1 (% Difference)	FEA Results Relative to Theoretical Results 1 (% Difference)
fn (Hz)						
1st	1.24	0.843	0.843	0.843	47.07%	0.00%
2nd	5.80	5.283	5.284	5.284	9.78%	0.02%
3rd	15.50	14.796	14.796	14.796	4.76%	0.00%
ω (/s)						
1st	7.79	5.297	5.298	5.297	47.07%	0.00%
2nd	36.44	33.194	33.202	33.200	9.78%	0.02%
3rd	97.39	92.966	92.965	92.966	4.76%	0.00%

What we want to start defining is how accurate the finite element method solves for the modes and vibration response of simple structures, such as beams. In comparing FEA modal analysis results to the theoretical results from the Matlab code, the last column in Table 2 shows that these two are almost identical, with differences between 0.00% and 0.02%, which validates this process for this cantilevered beam when compared against classical beam theory.

3.3 Shock Analysis of A Cantilevered Beam

Next, we evaluate the dynamic response of a cantilevered beam as modeled by finite element analysis and classical theory. In Chapter 4, impeller blades are modeled as cantilevered beams; thus, these results will be useful in this report. For this case, the cantilevered beam's geometry is as follows: Length = 18 inches long (0.4572 m), width = 2 inches (50.800 mm), and thickness = 0.0775 inches (1.969 mm). Material is aluminum with modulus of elasticity $E = 10.298 \times 10^6$ psi (71.002 Gpa) and a density $\rho = 0.10015$ lbf/in^3 (2272 Kg/m^3). Bending stiffness EI = 798.929 in·lbf (2.2948 N·m) by calculation. A 10 N force is step applied mid-span of the beam, at the center. "The acceleration impulse and the acceleration step are the classical

limiting cases of shock motion [16]." Figure 12 shows the boundary conditions and loading; the beam response is tracked at the free end.

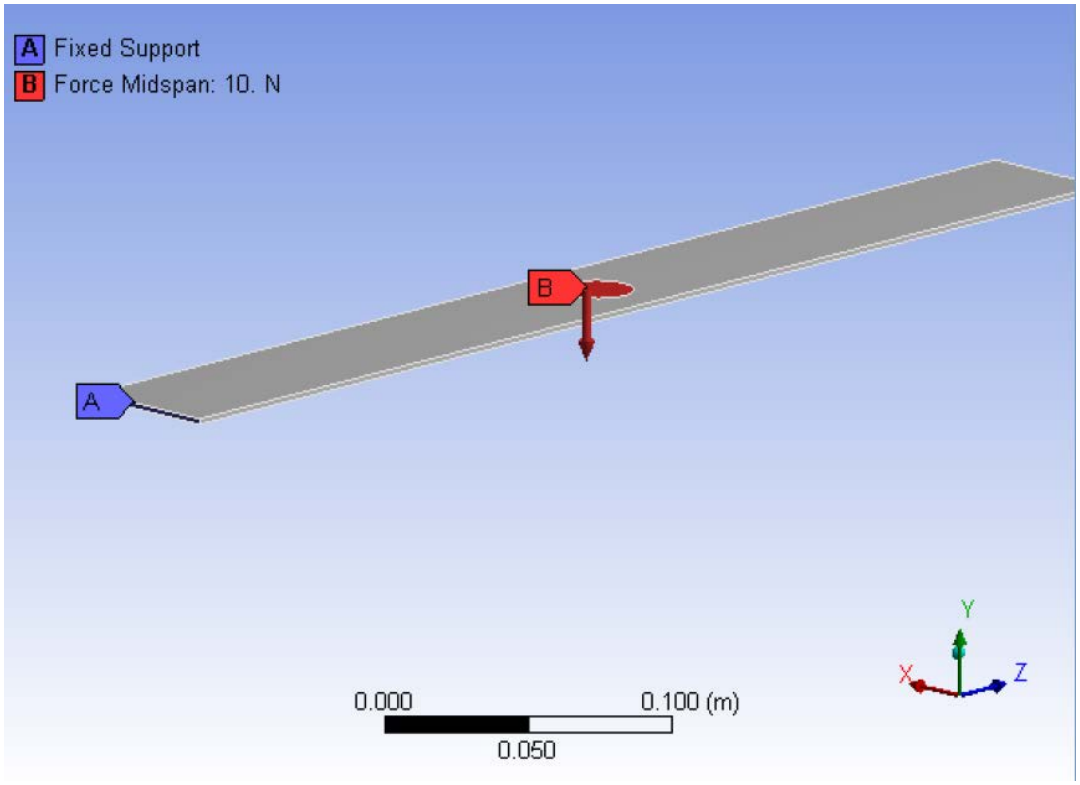

Figure 12. 18 Inch Long Cantilevered Beam with a 10 N Step Load.

The theoretical solution of this problem is carried out using a Matlab toolbox by Bingen Yang [12] for dynamic response of Euler-Bernoulli beams; modal expansion is used to calculate the transient response of the entire beam; here we focus on the response of the free end. Modal expansion is the superposition or addition of all individual modes which contribute to the overall response of the system. "We may interpret the forced vibration of the beam by considering the beam as composed of simple oscillators, where each oscillator consists of the beam restricted to vibrating in one of its natural modes. All these oscillators respond simultaneously, and the total beam vibration is simply the result of the addition (superposition) of all the individual vibrations [13]."

In using the Matlab toolbox for the dynamic response, five input parameters are required: definition of the load time, the location of the concentrated load, magnitude of the load, location of the required response, and the duration of the response or end time. The solution for the theoretical dynamic response of this beam is shown in Figure 13.

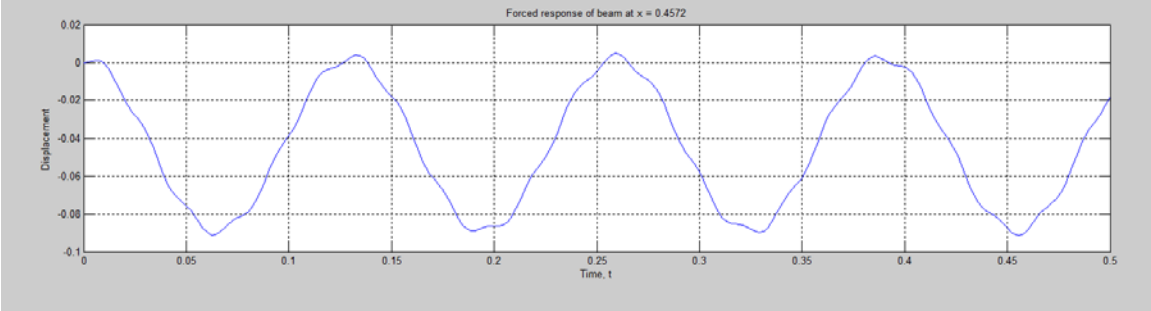

Figure 13. Dynamic Response at the Free End of Cantilevered Beam from Classical Theory.

The finite element model for this case involves solving for a finite number of mode shapes of the beam using the appropriate boundary conditions and then utilizing this solution to run the dynamic model applying the same loading condition as in the theoretical model above. Mesh density is very high in this model with over $532x10^3$ nodes. Significantly fewer nodes can be used without loss of resolution in the solution. However, there is sufficient computing power available so this mesh is kept. Tying the modal to the transient analysis allows for very efficient modeling; this technique is called Mode Superposition and is used for other analysis in this report. During the modal analysis, the first four "in plane" bending modes of the cantilevered beam were found. Together, these modes comprise a participation factor of 89.7% in the transverse, vertical direction deflection, which is the same direction in which loading occurs. This is a sufficiently high participation factor; it is a measure of how much energy usage is accounted for when the structure is driven or excited by the loading condition. Figure 14 shows the Ansys

solution for the vertical deflection of the free end of the beam; the time step is set to 0.003 seconds and the end time of the response is 0.5 seconds.

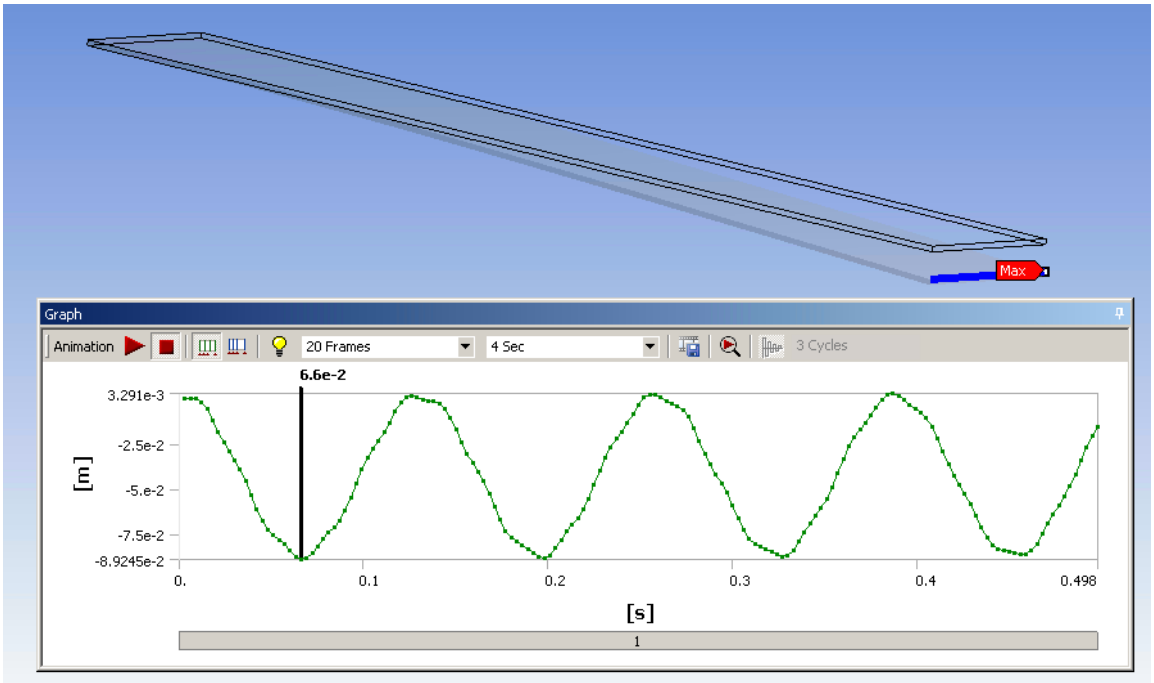

Figure 14. FEA Dynamic Solution for 18 Inch Long Cantilevered Beam with a 10 N Step Load.

Now, let's compare agreement between the finite element method and classical theory results for the 18 inch long aluminum beam undergoing a transient dynamic response. Figure 15 overlays both results from Figures 13 and 14 and shows a very good correlation, which validates this FEA process for analyzing simple structures undergoing impulse loading. Maximum deflection at the first peak from theoretical results is 91.28 mm and from FEA is 89.25 mm, a difference of only 2.3%. Both solutions show very good resolution; they match almost perfectly in the mid range of travel; at the peaks the response shows small discrepancies but overall the trend is the same, showing some high frequency content; structural damping is neglected since it is considered negligible.

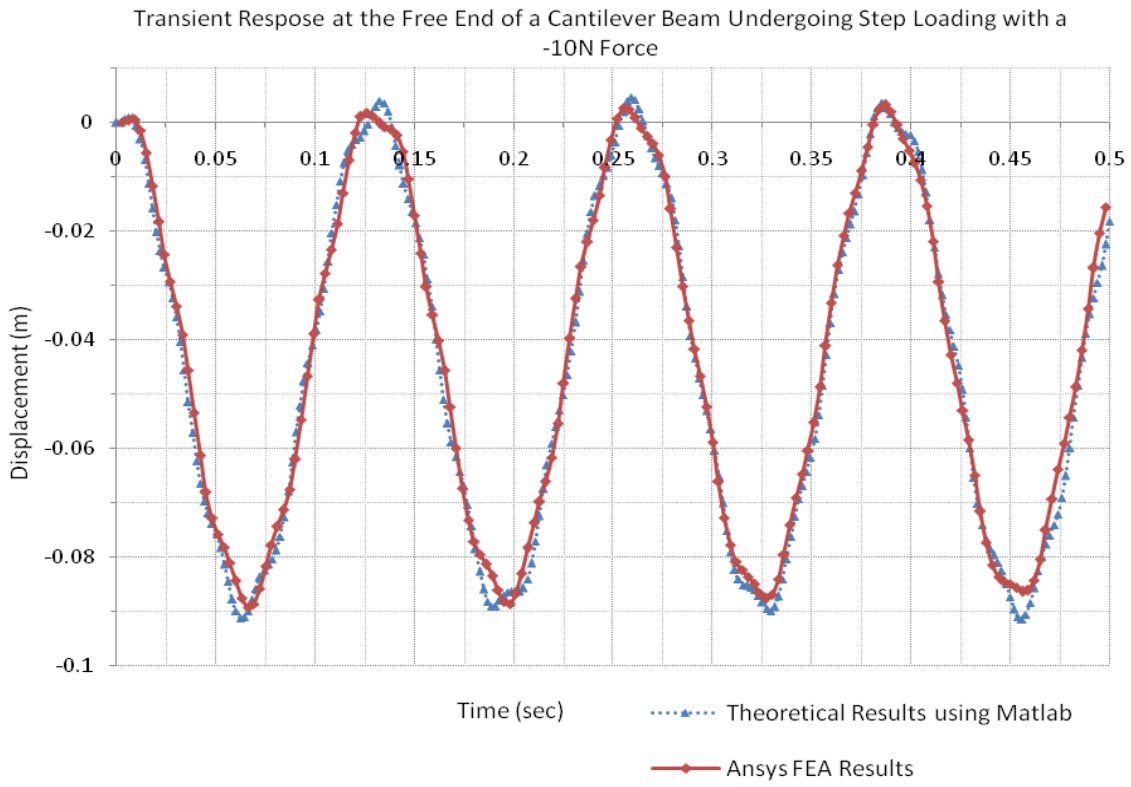

Figure 15. Comparison between FEA and Theoretical Results for an 18 Inch Long Cantilevered Beam.

We have verified how well the Ansys and FEA process works for modeling shock and impulse loading using the cantilevered beam basic structure. We now move on to Chapter 4 to analyze more complex structures and details related to this type of loading. There are three test cases studied in depth, always with the objective of gaining expertise in modeling shock loading in rotating and non rotating components and assemblies.

CHAPTER 4

CASE STUDIES OF SHOCK LOADING

The motivation for conducting these studies is to gain experience with behavior of more complex mechanical systems, using the same acceleration magnitude input, but varying the duration of the pulse. Another objetive is to understand, in relative terms, the implications when simplifying transient shock analysis as static analysis. This simplification is made, sometimes for lack of knowledge in performing transient analyses, or as an initial step to save time, etc. This exercise is found in Huei-Huang Lee's book [1], which provides significant information for conducting shock analysis.

4.1 First Case Study: Glass Panel Undergoing a 4 g Acceleration

Figure 16 shows a glass and forklift assembly. During service, it is important to know how much the tips and edges of the glass sag due to gravity, and also the amount of time it takes for the vibrations to settle during handling to prevent any contact when the glass is inserted into a processing machine. The mechanical properties of this assembly are shown in Tables 3 and 4.

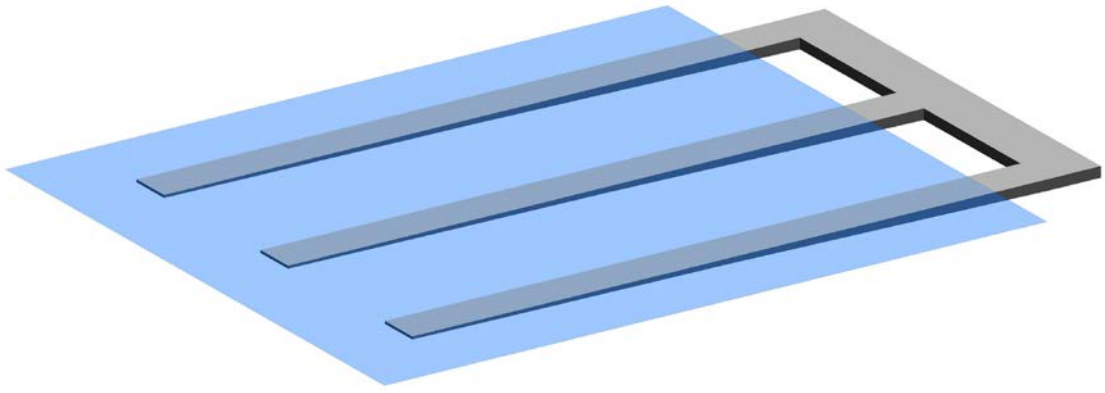

Figure 16. 2.2 m x 2.5 m (7.2 ft x 8.2 ft) Glass Panel on a Lifting Fork.

Table 3. Glass Panel Mechanical Properties.

Glass Panel	
Density (Kg/m^3)	2370
Young's modulus (GPa)	70
Poisson's ratio	0.22

Table 4. Steel Fork Mechanical Properties.

Steel Fork	
Density (Kg/m^3)	7850
Young's modulus (GPa)	200
Poisson's ratio	0.3

The contact type between the glass and fork is bonded and "it should be accurate enough for this case [1]." Mesh on the glass panel was the mapped face meshing type and for the steel fork a sweep method was used with solid shell elements. "When Solid Mesh is selected, workbench will mesh the body with SOLSH190 type elements; it is fully compatible with other types of solid elements, and has extra degrees of freedom to account for bending modes [1]." Figure 17 shows the mesh of the assembly created in Ansys. "As a guideline when a solid body is meshed with only one layer of elements in one direction and the deformation is dominated by bending, the Solid Shell is an appropiate choice [1]."

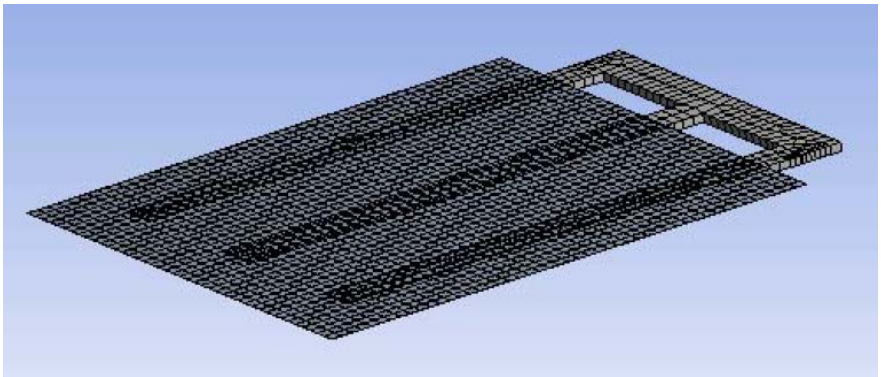

Figure 17. Mesh of Glass Panel and Fork.

A fixed support is assigned at the cross beam of the steel fork, on the back face as shown in Figure 18. This provides a glass response relative to the steel fork rather than an absolute response of both the glass and the fork where it would be difficult to capture the small vibration on the glass due to the large deflections that this assembly experiences. "This way the same effect is attained avoiding getting the analysis overwhelmed numerically [1]."

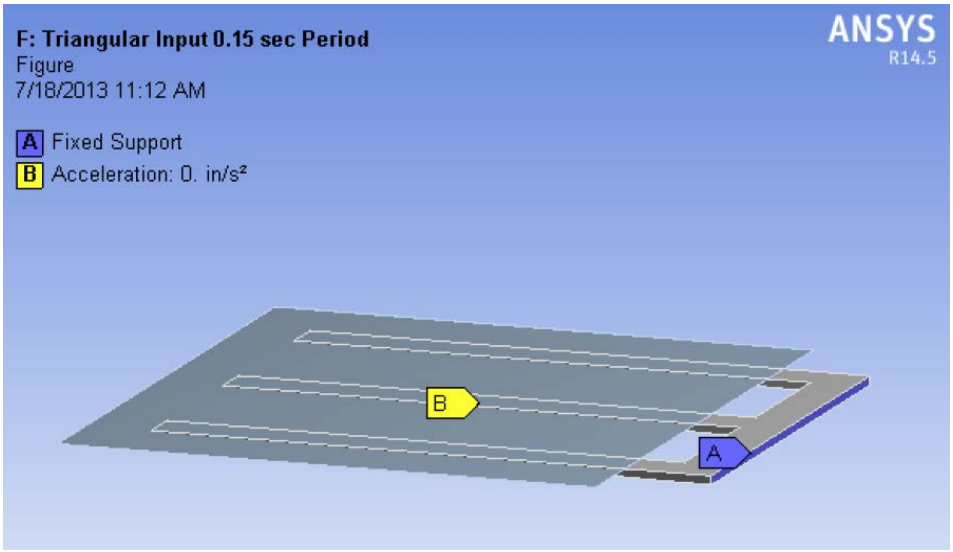

Figure 18. Boundary Conditions of the Assembly.

The acceleration of this assembly, in this exercise, occurs as shown in Table 5 and Figure 19. To minimize vibrations, the assembly reaches maximum acceleration in the middle of the up travel then decelerates until it reaches the top in another 0.15 second. The maximum velocity reached is 6 m/s in 0.15 second; this equates to a maximum acceleration of 40 m/s^2 (1574.8 in/sec^2) then acceleration is reversed to slow down the glass panel as it reaches the top. The same principle and magnitudes are true for lowering the glass panel.

Table 5. Glass Panel Triangular Wave Input, 0.6 Second Period.

Steps	Time [s]	X [in/s²]	Y [in/s²]	Z [in/s²]
1	0.	0.	0.	0.
	0.15		1574.8	
	0.3		0.	
	0.45		-1574.8	
	0.6		0.	
	1.5			

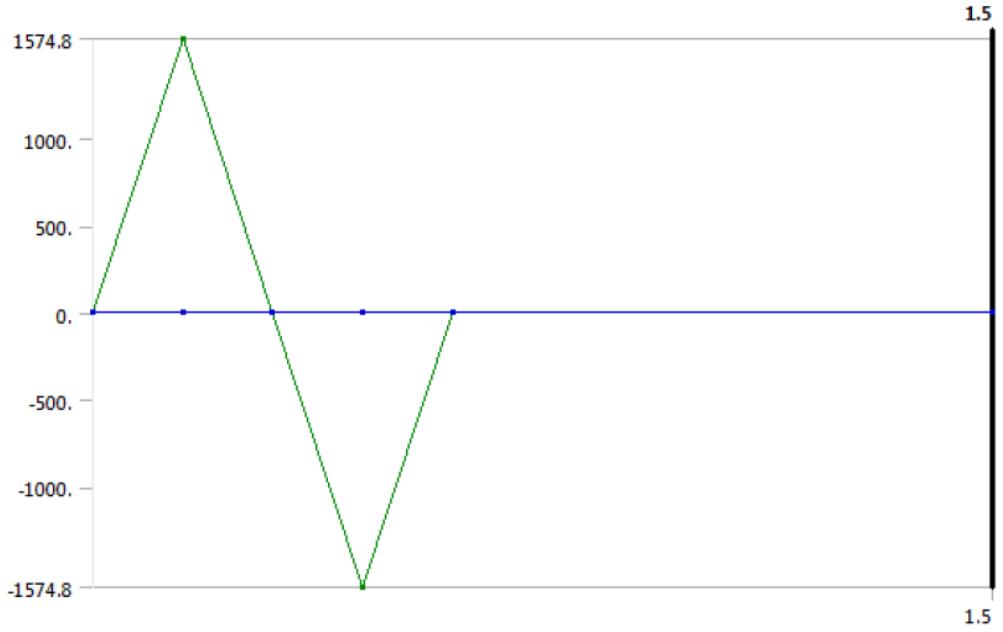

Figure 19. Glass Panel Triangular Wave Input, 0.6 Second Period.

Step end time "is the total simulation time [1]." In the initial run, this is made two times longer than the pulse width to estimate the system's response. The Initial Time Step, as a guideline, should be about 1/20 the natural period of the fundamental mode for sine or triangular type impulses. For example, for sharper acceleration inputs, such as step inputs, this initial time step needs to be tighter at the time the input occurs. The fundamental frequency for the assembly is calculated using the finite element method, ω_n = 8.4 Hz. The natural period τ_n, is simply the inverse of the natural frequency, thus τ_n = 0.119 seconds. The nominal stiffness coefficient selected for the glass panel is 0.002 from experimental results and material properties for the glass panel [1].

A Deformation probe is included at one of the corners sagging over the free end of the fork fingers to track maximum deflections in the transient state. As seen in Figure 20, the maximum peaks in both directions occur before 0.5 seconds; by 1.25 seconds, deflections have dampened to 0.13 inches (3.4 mm). Workbench automatically adjusts the time step according to the response frequency. As the response frequency decreases later in time, the time step also decreases to mantain good definition in the response.

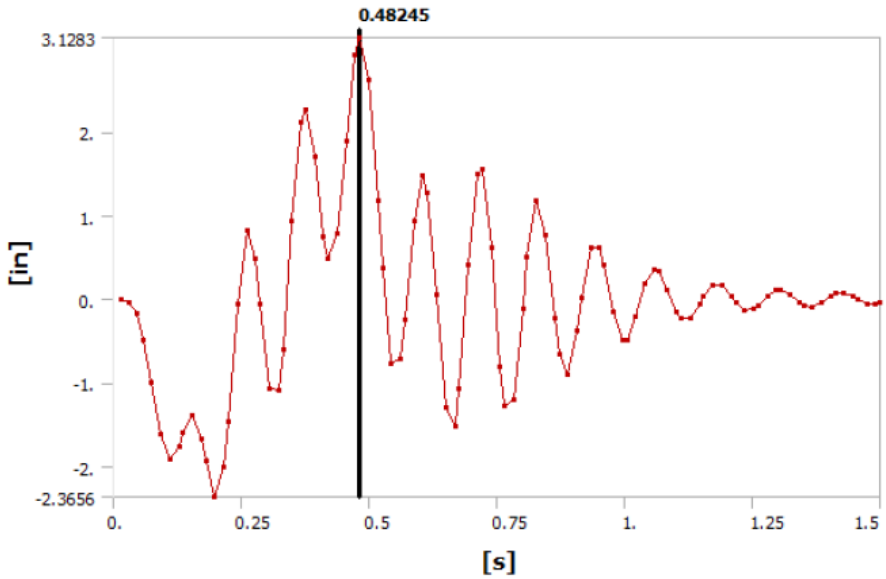

Figure 20. Deformation Probe at the Glass Corner.

4.1.1 Variation of the Pulse Width Sensitivity Study

This is the first study conducted on the sensitivity of varying the pulse width of the acceleration input and tracking variations in tip deflections and stresses. An important parameter to define is the time to maximum acceleration (TMA); this is the time it takes for the input to reach its maximum value. In the case of a half sine acceleration input for example, the TMA would be half of the pulse width. The convergence trend seen in this dynamic case settles when the time to maximum acceleration (TMA) of the input is at least twice the natural period of the glass panel. Table 6 and Figure 21 show that maximum tip deflection reaches a value of approximately 2.0 inches for TMA ratios of 1.9 and higher. For values where this TMA ratio falls below 1.9, it defines progressively sharper shocks where deflections start to increase rapidly. Depending on the specific type of glass, it would most likely break before being able to sustain a shock with a TMA ratio of 0.3 where deflections are calculated above 10 inches. Asuming it does not, and that deformations are linear, Table 6 and Figure 21 describe maximum amplitude of vibration as a function of different pulse widths or TMA ratios.

Table 6. Glass Panel Stress and Deflection Sensitivity to Impulse Duration.

2.2 m X 2.5 m Glass Panel Dynamic Analysis Results. All Runs Used the Same Mesh and a Stiffness Coefficient of 0.002. Natural Period is calculated at 0.119 seconds for the Fundamental Mode of the Glass Structured Restrained by the Steel Fork.				
Time to Maximum Acceleration (s)	Ratio of Time to Maximum Acceleration / Natural Period	Total Input Duration - Triangular Pulse (s)	Maximum Tip Deflection - Vertical Probe (in)	Maximum Equivalent Stress on Glass Surface at Free End of Fork (ksi)
0.015	0.1	0.06	6.09	17.79
0.023	0.2	0.09	9.66	28.32
0.038	0.3	0.15	10.26	31.16
0.075	0.6	0.3	4.93	14.29
0.150	1.3	0.6	3.13	6.74
0.225	1.9	0.9	2.13	4.06
0.300	2.5	1.2	1.96	4.14
0.375	3.2	1.5	2.04	3.59

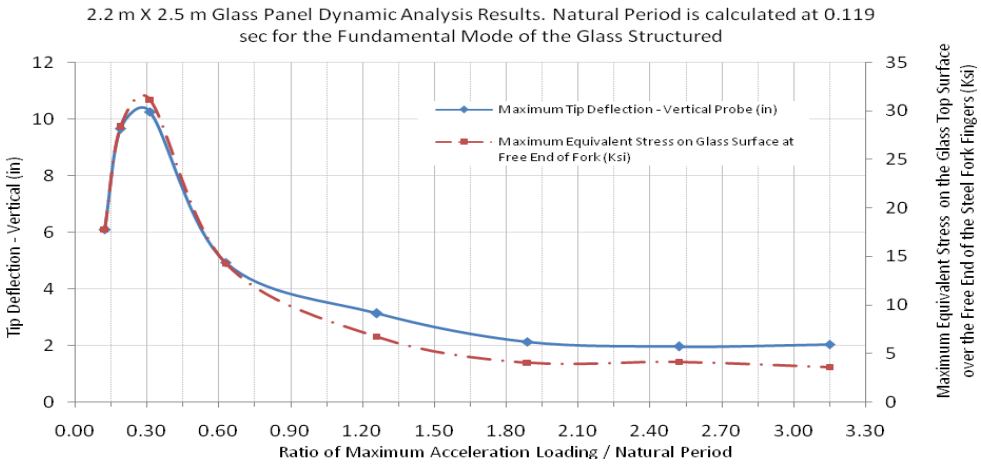

Figure 21. Glass Panel Stress and Deflection Sensitivity to Impulse Duration.

Likewise, stresses also settle at a maximum value between 3.6 and 4.1 ksi on the top surface of the glass panel near the free end of the fork fingers. Figure 22 shows the location where these streses were calculated. The calculated deflections are considered a better response measure for this study since that panel corner point is more easily selected and tracked by Ansys; however, stress values are a good representation of trend; both curves in Figure 21 have very consistent shapes.

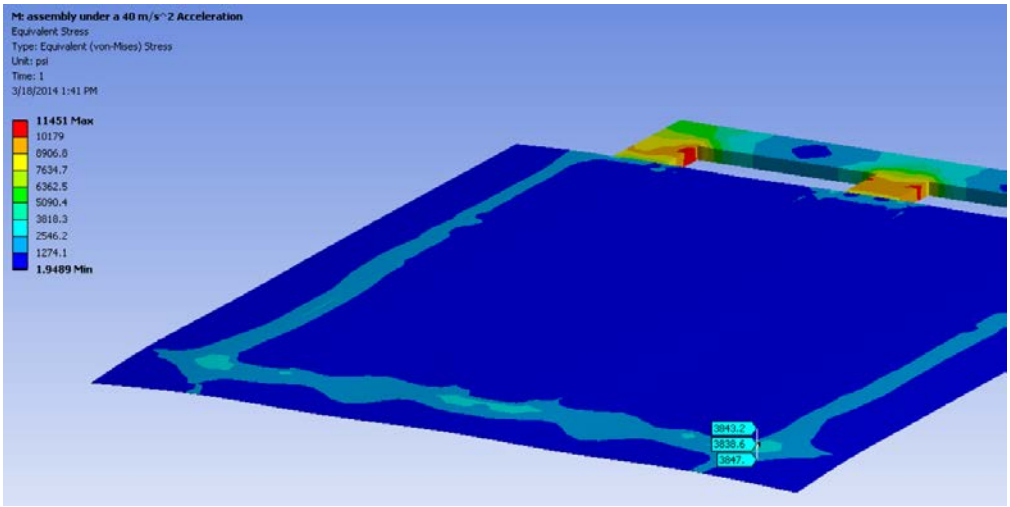

Figure 22. Stresses were evaluated on the Glass at the Corner Support, bottom right.

4.1.2 Transient Analysis vs Static Analysis

Transient analyses, methods A and B in Table 7, are more involved than static analyses; engineers often simplify transient cases as static cases for different reasons. Static models are often used to analyze dynamic systems and their results may not be correct in many cases. Table 7 includes two static analyses, cases D, and E, that are sometimes used to calculate maximum stresses and deflection of dynamic systems; in case E, the resultant force from the weight of the part multiplied with the g value of the acceleration is used and simply exerted on the body; or similarly, in case D, the density of the part is modified so the part weight is representative to what it would be due to a higher value of acceleration. Case C involves using acceleration over a long period of time such as 1 second which does not produce a transient response on the system and a quasistatic result is obtained.

Something worth noting in Table 7 is that stresses and deflections in case C are the stresses and deflections one would expect from a transient analysis, as the pulse width of the input increases to a large value above 0.45 seconds, corresponding to the total input duration of 0.9 seconds in Table 6.

In Table 7, stresses and deflections in Static Cases D and E are shown to be over 3.5X and over 4X lower respectively, when compared to transient analysis Case A. Discrepancies in results can be even more significant when compared with sharper shock inputs such as those with TMA ratios less than 0.6 in Table 6. This is a significant difference, thus running static analyses in place of transient analyses for mechanical evaluation of impulse loading is not considered appropiate. Furthermore, two inputs with the same pulse width but different magnitudes can excite the part differently. This energy content of the input is another parameter that can influence the structural response which would only be evident from a transient analysis.

Table 7. Transient Cases A, B, C vs Static Cases D and E.

Case	Description	Max Stress on Glass Surface over the Free End of the Fork Fingers (ksi)	Max Vertical Deflection At Glass Corner (in)
A	Glass under 4.1 g acceleration, & 0.3 second total triangular input	14.29	4.93
B	Glass under 4.1 g acceleration, & 0.6 second total triangular input	6.74	3.13
C	Glass under 4.1g acceleration, ramped in 1 second	3.85	1.95
D	Static Case - Glass with 4X density for 4X the weight	3.81	1.36
E	Static Case - Glass with 4X force equivalent to 4X the weight	3.84	1.17

4.2 Second Case Study: The I508 Inlet Guide Vane Housing (IGV)

The I508 IGV is the subject in this second case study and it has material callouts for 6061-T6 aluminum. Material specifications used in these analyses are as follows: density is 0.098 lbf/in^3, modulus of elasticity is 10E6 psi, and Poisson's ratio is 0.33. The acceleration input used for this analysis is crash hazard shock involving a half sine 40 g magnitude impulse with a 11 ms pulse width as shown in Figure 23.

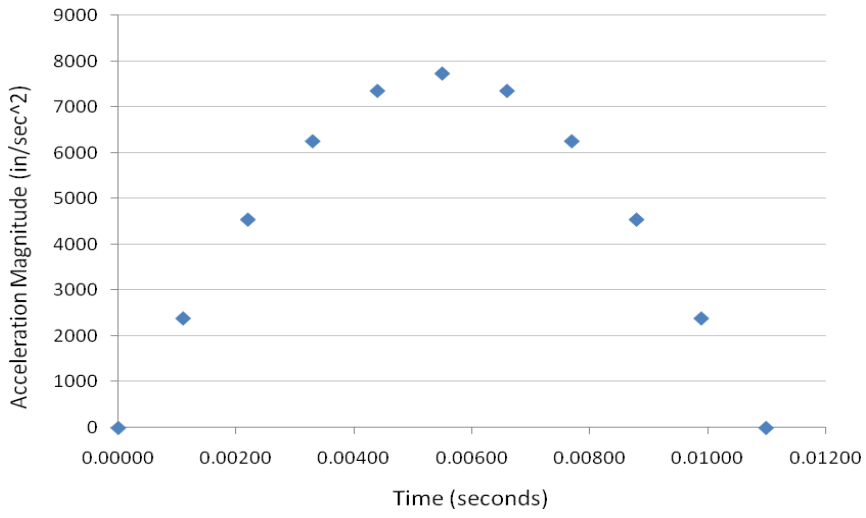

Figure 23. A Crash Hazard Shock, a Half Sine Pulse with 40 g in 11 milliseconds.

4.2.1 IGV Stresses and Deflections vs Direction of Shock

Using a simplified IGV model with a reduced number of vanes, a 40 g impulse load is applied in all three cartesian axes independently to determine which axis has the weakest response to this input. This model with over $90x10^3$ elements and run times of several hours provides useful preliminary results as presented in Table 8. For boundary conditions, a fixed support is placed on the flange of this structure.

This IGV is not a radially symmetric part since there is one cutout for a hose in the back side; therefore, a slight difference exists in response between a shock in the X axis versus the Y axis. Figure 24 shows the simplified IGV model containing only 20 Vanes.

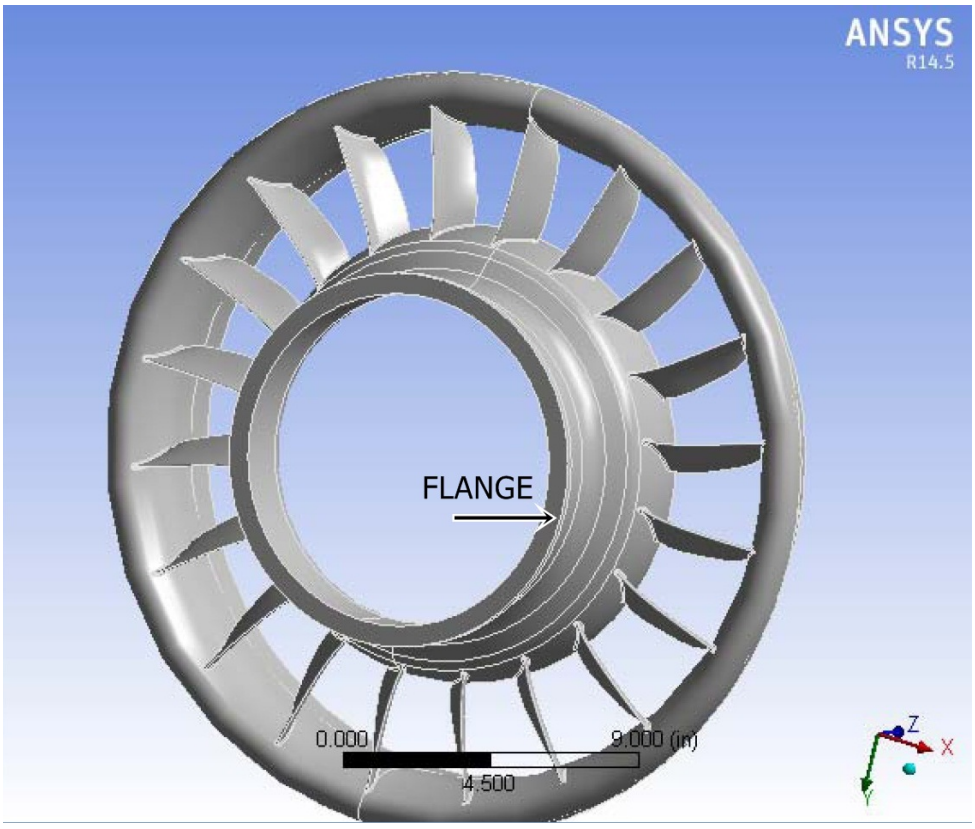

Figure 24. I508 IGV Simplified Model with 20 Vanes.

The weakest response is when the shock is in the axial direction and responses for forward or backward acceleration are identical; thus only evaluations in the Z direction are analyzed in the final model. Stress levels for the axial acceleration are 2.5 times higher relative to lateral acceleration inputs in these preliminary models.

Table 8. Stress and Deformation Results for The I508 Simplified IGV Under 40 g of Acceleration, 20 Vanes, X, Y, and Z Acceleration Inputs.

Analysis Type	Max Stress (ksi)	Max Deformation (in)	Notes
IGV w/40 g Acceleration - 90° to cutout	2.055	0.0015	max stresses at cut out and TE, hub side, concave side, 90° to cutout
IGV w/40 g Acceleration thru hose cutout	2.25	0.0016	max stresses at cut out and TE, hub side, concave side
IGV w/40 g Acceleration in axial direction - Backward	5.318	0.0046	max stresses at on all vanes, TE, shroud side, concave side
IGV w/40 g Acceleration in axial direction - Forward	5.318	0.0046	max stresses at on all vanes, TE, shroud side, concave side

4.2.2 I508 IGV Full Model

These analyses using a complete IGV model have shown that maximum stresses are in the axial direction and maximum radial deflections occur during a shock directed in an axis going through the hose cutout. A summary of all final results are included in Table 9. The 3D model for these analyses include all vanes and features. The model is discretized into $359x10^3$ elements and constrained with a fixed boundary on the flange of the part. As expected, stress results for this full model with a tighter grid are slightly lower, compared with the simplified model from the previous section. These IGV models have a minimum run time of 41 hours.

Table 9. I508 IGV Full Model Under a 40 g Shock, All 37 Vanes, X, Y, and Z Acceleration Inputs.

Shock Direction	Maximum Stress (ksi)	Maximum Total Deflection (in)	Maximum Deflection in the Radial Direction over Impeller (in)	Notes
Axial Shock	4.77	0.00451	0.00017	
Lateral Shock in X	2.10	0.00197	0.00071	perpendicular axis to hose cutout
Lateral Shock in Y	1.95	0.00210	0.00130	axis thru hose cutout

4.2.3 Evaluation of Maximum IGV Stresses and Deflections

Among the stress results from all three coordinate directions shown in Table 9, stresses in the axial direction are the highest at 4.77 ksi; maximum total deflection is 0.0045 inches. This deflection is low because the 11 ms pulse width of the input is much higher relative to the natural period of this structure. Due to the high fundamental frequency of the IGV, the response to this shock is quite similar to a quasistatic loading. Additional deflection may occur due to additional compliance in the other components of the rotor such as the bearings, bearing housings, shaft, impeller hub, etc. Maximum stresses and total deformations are 2.3 and 2.1 times higher, respectively, when compared to results in the orthogonal directions. Stress and deflection distributions are shown in Figures 25 and 26. During this transient state of the shock load in the axial direction, the tendency of the vanes and the outer ring is to rotate in the clockwise direction slightly, as seen from the front of the IGV. Run time for this analysis is 43.05 hours.

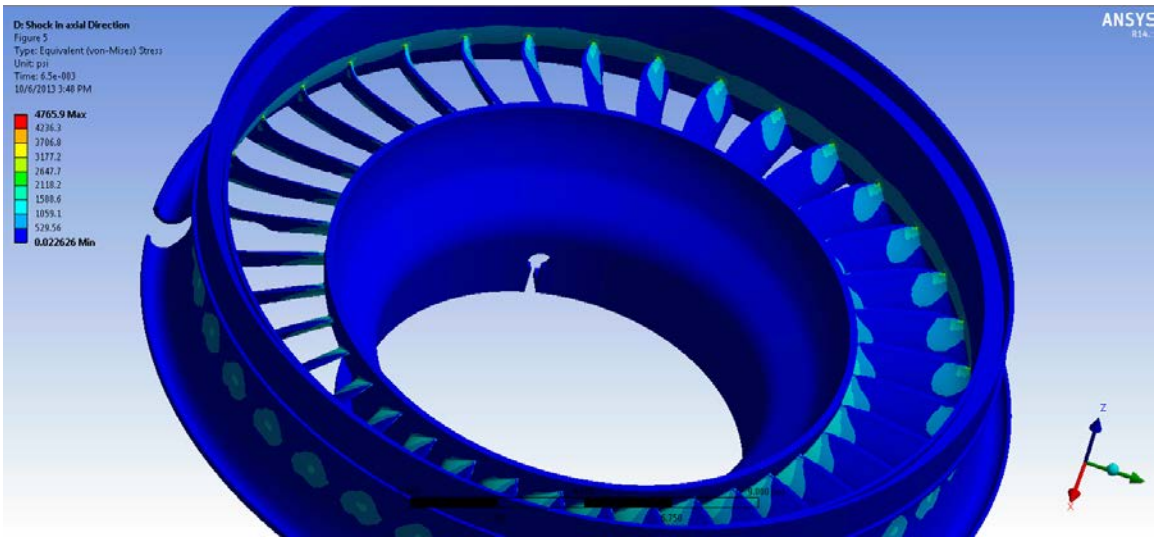

Figure 25. IGV Axial Forward Results, Maximum Stresses = 4.77 ksi.

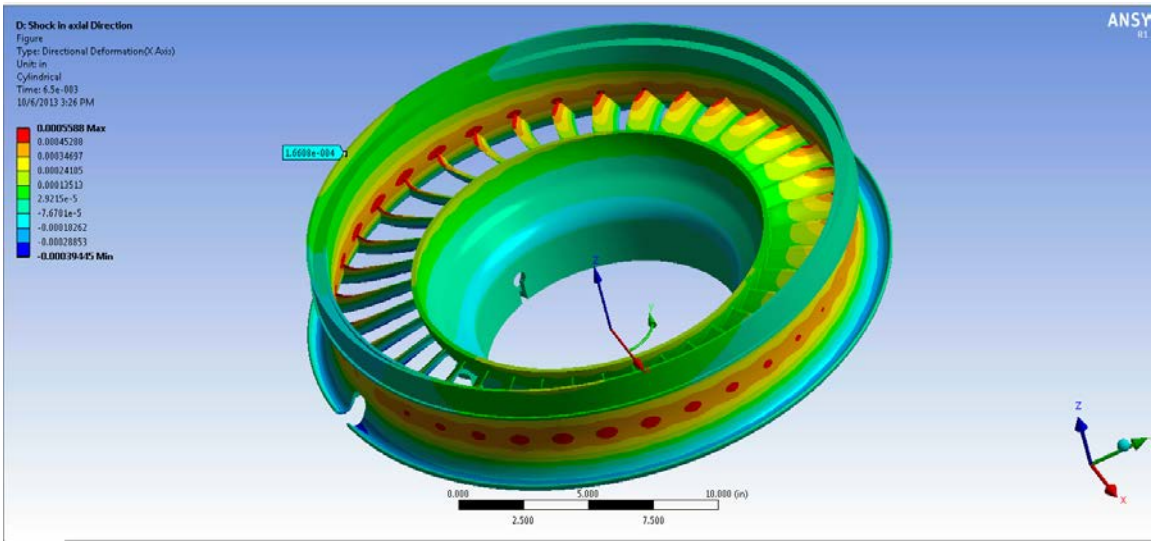

Figure 26. IGV Axial Forward Acceleration,
Maximum Radial Deformation over Impeller Blades = 0.00017 inches.

4.2.4 Sensitivity of Pulse Width, IGV Axial Forward Direction

In this study on the variation of pulse width of the acceleration input, we see a very similar trend when compared with results from the previous case study. Figure 27 and Table 10

show that in the case of this IGV, deflections (solid curve) and stresses (dashed curve) start increasing rapidly for a TMA/Natural-Period ratio of approximately 3.5 and under; in the previous case with the glass panel this ratio was closer to 2.

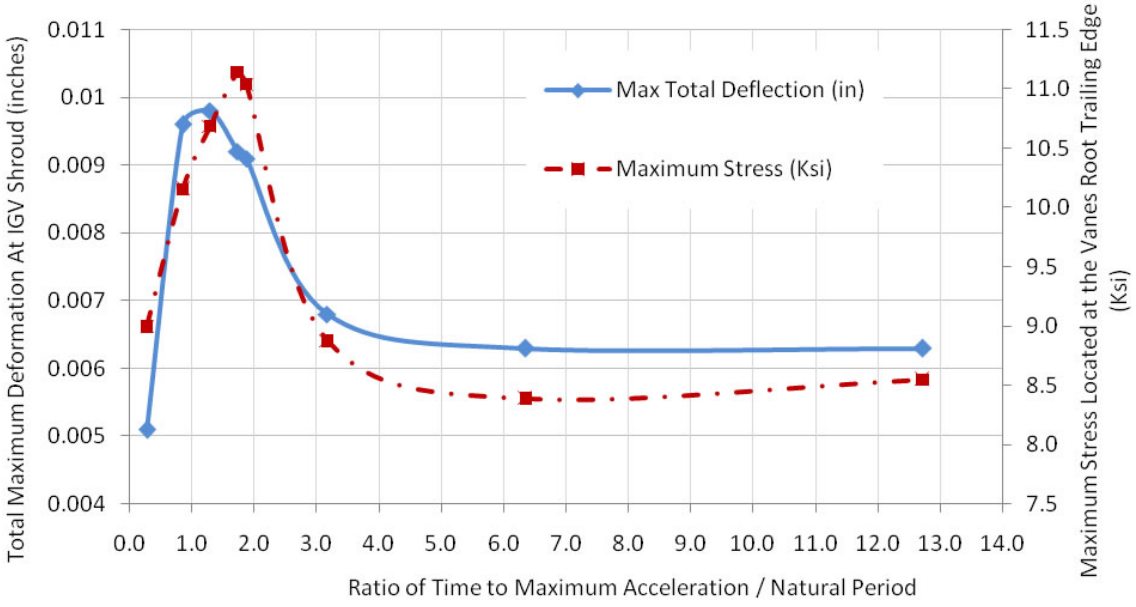

Figure 27. Simplified IGV Stress and Deflection Sensitivity to Impulse Duration, 40 g Forward Shock, τ_n = 1.7 ms.

Table 10. High Resolution Results For the Dynamic Response of a Simplified IGV to a 40 g Axial Forward Acceleration.

Pulse Width (ms)	Time to Maximum Acceleration, TMA (ms)	Ratio TMA / Natural Period	Maximum Stress (ksi)	Maximum Total Deflection (in)	Details
1.0	0.50	0.3	8.998	0.0051	0.25 ms ITS
3.0	1.50	0.9	10.155	0.0096	0.25 ms ITS
4.5	2.25	1.3	10.686	0.0098	0.5 ms ITS
6.0	3.00	1.7	11.140	0.0092	0.5 ms ITS
6.5	3.25	1.9	11.040	0.0091	0.5 ms ITS
11.0	5.50	3.2	8.877	0.0068	same results at 1ms ITS and 0.5ms ITS
22.0	11.00	6.4	8.390	0.0063	0.5 ms ITS
44.0	22.00	12.7	8.550	0.0063	0.5 ms ITS

The maximum deflection that occurs at the outer ring of the IGV is approximately 0.010 inches for a TMA to natural period ratio of 1.3, that corresponds to an acceleration pulse that is 4.5 ms in width. During operation, this part is not expected to experience such a sharp shock loading; but if it did, deflections and stress levels would still be acceptable at a 40 g magnitude. For TMA ratios above 4.0, total deflections approach a constant value of 0.0063 inches. In Table 10, the details of the analyses show the high level of precision for the initial time steps of each solution; the smaller time steps are as little as 0.25 ms and show enough detail in the solutions response. When the pulse width is only a couple of milliseconds wide, a 1 ms time step is too long for the analysis to even run; thus a 0.5 ms and a 0.25 ms run are performed. In all, for the IGV alone, more than 20 runs were completed, with the more complicated meshes taking over 40 hours to solve using a Full Method Solver which is later discussed.

4.3 Third Case Study: Baseline Impeller Shock Analysis

For this last case study, a shock analysis of impellers is performed in more detail. In addition to studying the effect of varying pulse width of the acceleration input, rotation and shock loading effects are studied together and separate using multiple time steps as well as with and without integrating modal analysis. A convergence study is also conducted to ensure no singularities are present. Convergence for this model occurs at around a million nodes; all of the modal and shock analyses in Ansys are completed using over half a million nodes to make these analyses less demanding in terms of duration.

A genetic Baseline impeller is created as a means to efficiently run and share these finite element models with other engineers and professionals, specifically individuals at Ansys, Inc., with whom several technical meetings occurred. This Baseline Impeller only includes three blades, has cyclical symmetry, is relatively small in size, and has a very manageable mesh size. Figure 28 shows an image of this Baseline impeller. Mechanically, this impeller's geometry is

representative of an impeller used in high efficiency fans, air movers, and propulsion machines. Figure 29 is an example of a Propulsor impeller.

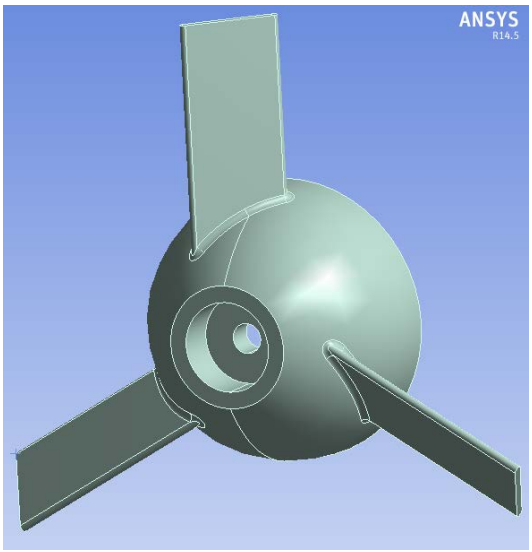

Figure 28. Baseline Impeller, a Representative Impeller Mechanical Model.

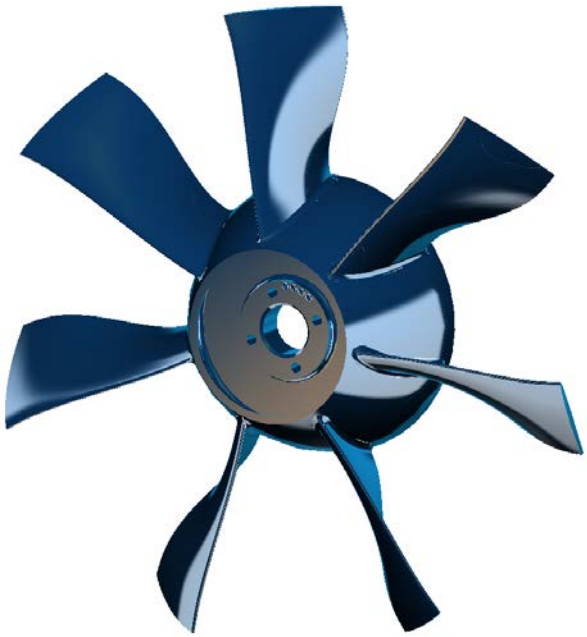

Figure 29. A Production Typical Propulsor Impeller.

The Baseline impeller is analyzed using 6061-T6 aluminum properties: modulus of elasticity, E = 69 Gpa (10E6 Psi), and density, $\rho = 2710$ Kg/m^3 (0.098 lbf/in^3), and Poisson's ratio $\upsilon = 0.33$. Geometric properties include a maximum diameter of 267 mm (10.5 inches), axial length of 63.5 mm (2.5 inches), a volume of 0.29E-3 m^3 (17.79 inches^3), and principal moment of inertia about the rotation axis of 2.13E-3 Kg·m^2 (7.27 lbf·in^2). The width and thickness of the blades are 0.0366 m (1.441 inches) and 0.0036 m (.144 inches) respectively, and the average length of the blade is 0.0851 m (3.350 inches).

The mode shape of the Baseline impeller blades are calculated using two methods. First, the blades are asummed to behave like cantilevered beams and their modes are calculated theoretically; then, the finite element method is used to calculate modes of the blades as integral parts of the impeller. These results are then compared to determine how effective it is to use the cantilevered beam approximation.

Resonance frequencies and mode shape analysis results from classical theory were conducted using the Matlab code included in the Appendix. The thickness to length ratio of the baseline impeller blades is 0.042 or 4.2% which qualifies as a slender beam, and the Euler-Bernoulli theory can be employed. The first three natural frequencies shown in Figures 30 through 32 occur at 400 Hz for the first mode, 2511 Hz for the second mode, and 7033 Hz for the third mode. These are the frequencies for the stand alone blades approximated as cantilevered beams.

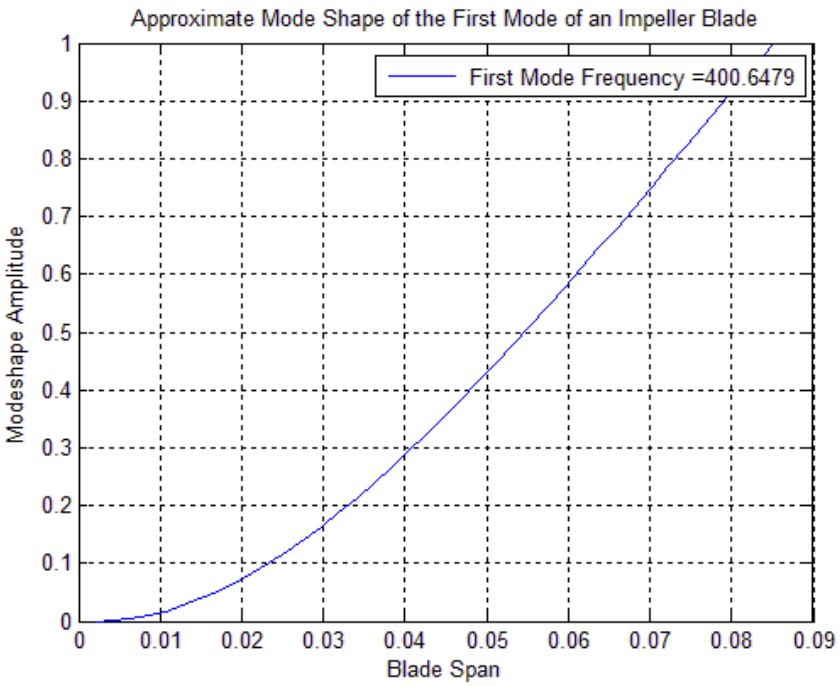

Figure 30. First Resonant Frequency and Mode Shape of the Baseline Impeller Blade Approximated as a Cantilevered Beam.

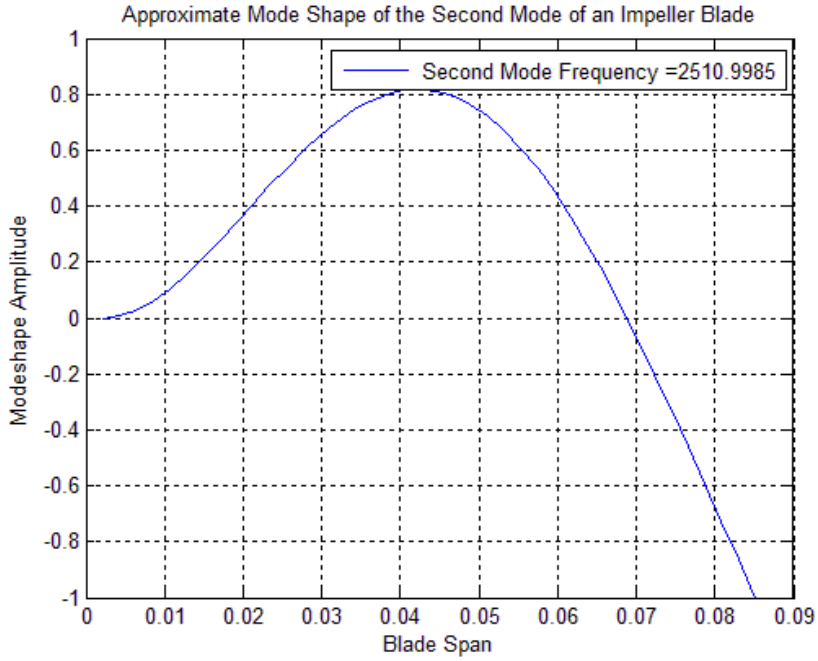

Figure 31. Second Resonant Frequency and Mode Shape of the Baseline Impeller Blade Approximated as a Cantilevered Beam.

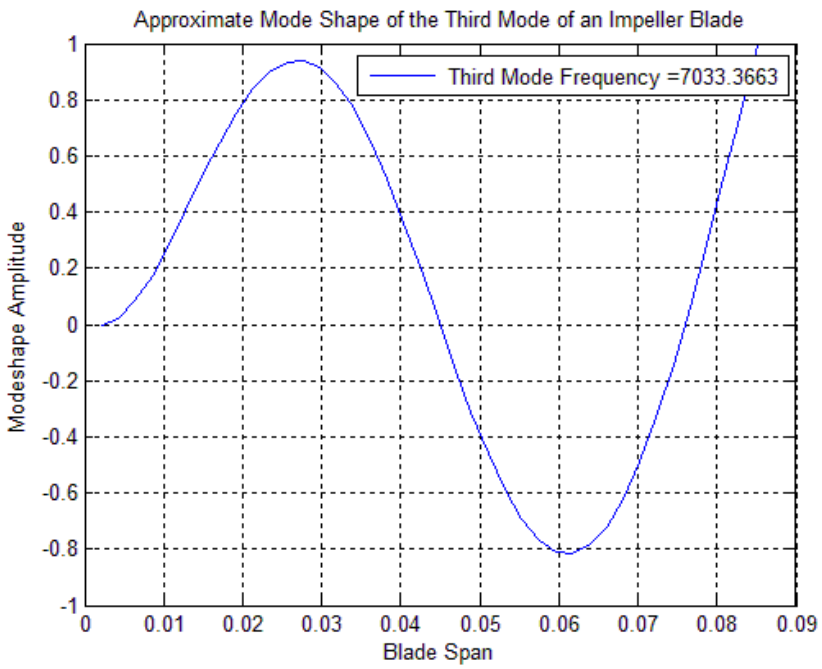

Figure 32. Third Resonant Frequency and Mode Shape of the Baseline Impeller Blade Approximated as a Cantilevered Beam.

Modal analysis of the Baseline Impeller is conducted taking into account the previous modal results from classical beam theory. It becomes easier to find these modes in Ansys where a set of frequency ranges is selected and solved for. The Impeller model in this FEA analyses is constrained at the center bore. Resonant frequency results using finite element analysis for the first, second, and third bending modes are 448 Hz, 2751 Hz, and 7394 Hz respectively and are shown in Figures 33 through 35 below.

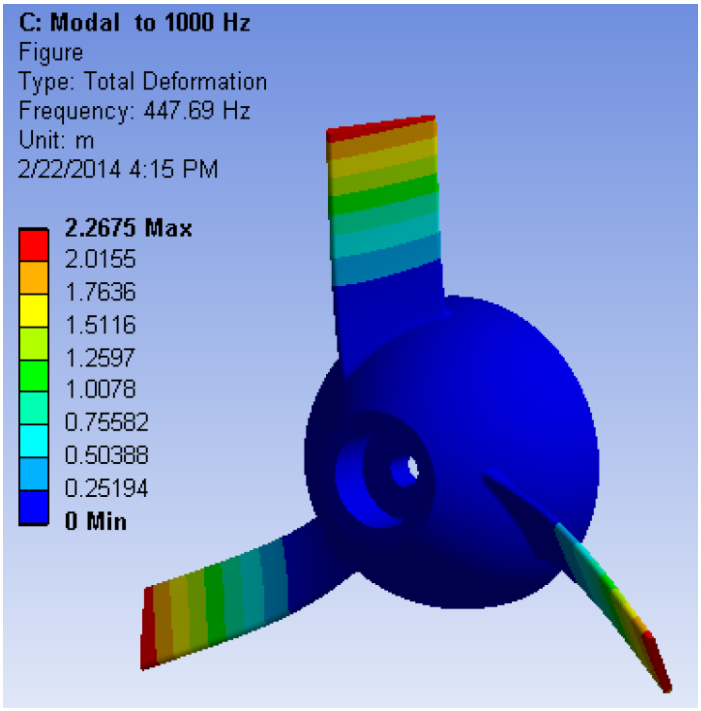

Figure 33. First Bending Mode of Blades at 448 Hz.

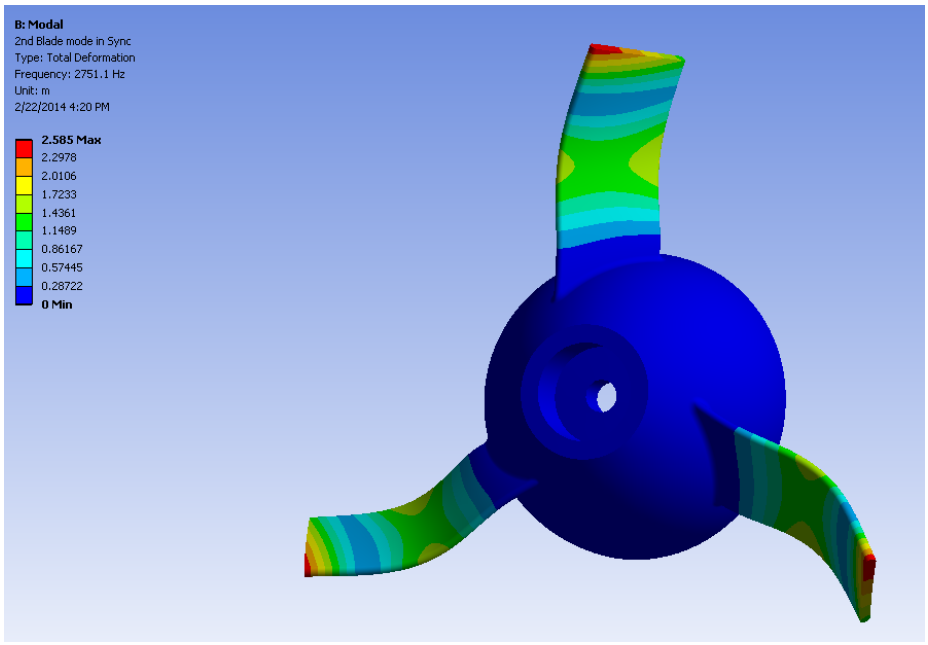

Figure 34. Second Bending Mode of Blades at 2751 Hz.

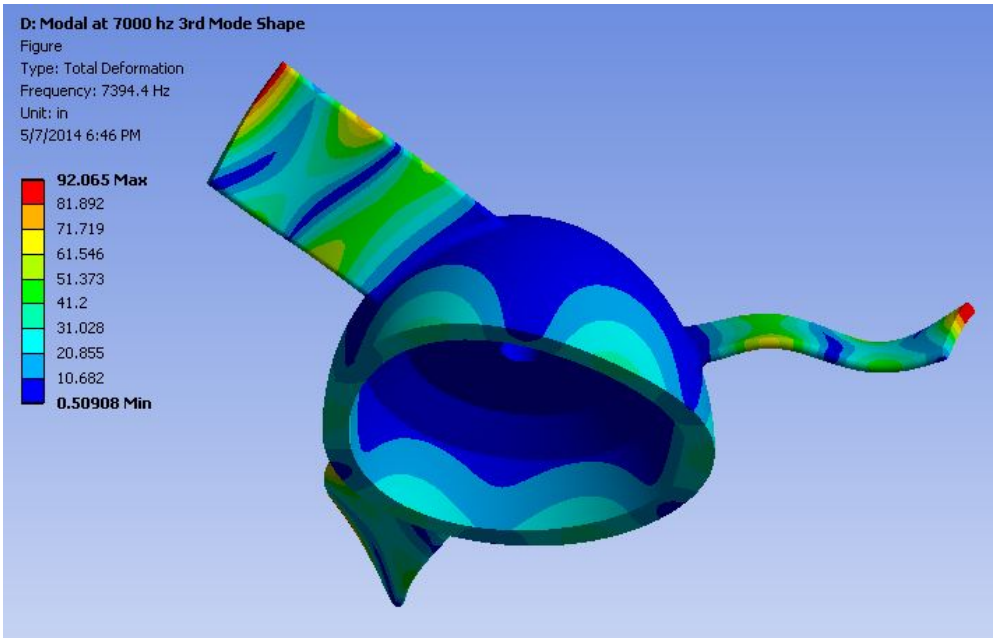

Figure 35. Third Bending Mode of Blades at 7394 Hz.

Performing an initial modal analysis using Matlab and the Euler-Bernoulli beam theory has proven to be very useful and a very efficient preliminary analysis that can be performed on impeller modal analysis prior to a more demanding finite element analysis. Furthermore, Table 11 shows that at least for the first three bending moments, the analytical results are in the range of 10.5% effectiveness or better. Analytical results can be combined with a Campbell diagram as a preliminary design step towards designing an impeller clear of blade resonances at specific operating points in the system. Next, Ansys is used for shock analysis of this Baseline impeller model.

Table 11. Analytical and FEA Modal Results For The Baseline Impeller.

Bending Modes	Analytical Result of Bending Modes of Blades as Cantilevered Beams (Hz)	FEA Blade Bending Mode of Baseline Bladed Impeller (Hz)	Difference Of Analytical Results Relative to FEA Results (%)
1st	400.7	447.7	10.5%
2nd	2511.2	2751.1	8.7%
3rd	7033.4	7394.4	4.9%

4.3.1 Baseline Impeller Shock Analysis By Finite Element Analysis

Shock analysis is studied in depth using the Baseline Impeller model shown in Figure 28. Primarily, this model is designed to study the effects of rotation and shock; these loading types are studied together and independently, as well as in combination with modal analysis which is called Mode Superposition analysis. Secondly, this model is also used to study once again the effect of varying the pulse width of an acceleration shock input and compare with the other systems studied earlier. A half-sine acceleration input of 50 g in Figure 36 shows a graph of this input generated in an Excel worksheet. This becomes the tabular input used in Ansys for a transient analysis.

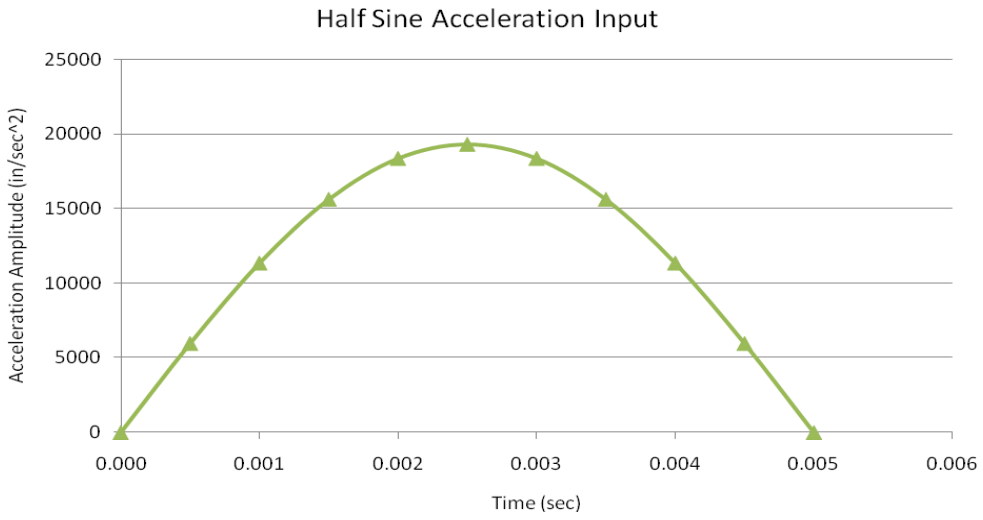

Figure 36. Half Sine Acceleration Shock Input with a Positive Magnitude of 50 g and a Pulse Width of 5 ms.

The Baseline Impeller 3D model is meshed using tetrahedron elements with a higher element count where the geometry has more abrupt transitions and where the highest strain is expected. This mesh is controlled mainly by minimum number elements across any thickness of the part and by curvature in the geometry. The normal angle is set to 45°, minimum number of cells is set to 2, and transition between fine and coarse areas in the model is set to slow for higher

gradient definition. Figure 37 shows the meshed Baseline impeller model which contains 551,830 nodes and 381,866 elements.

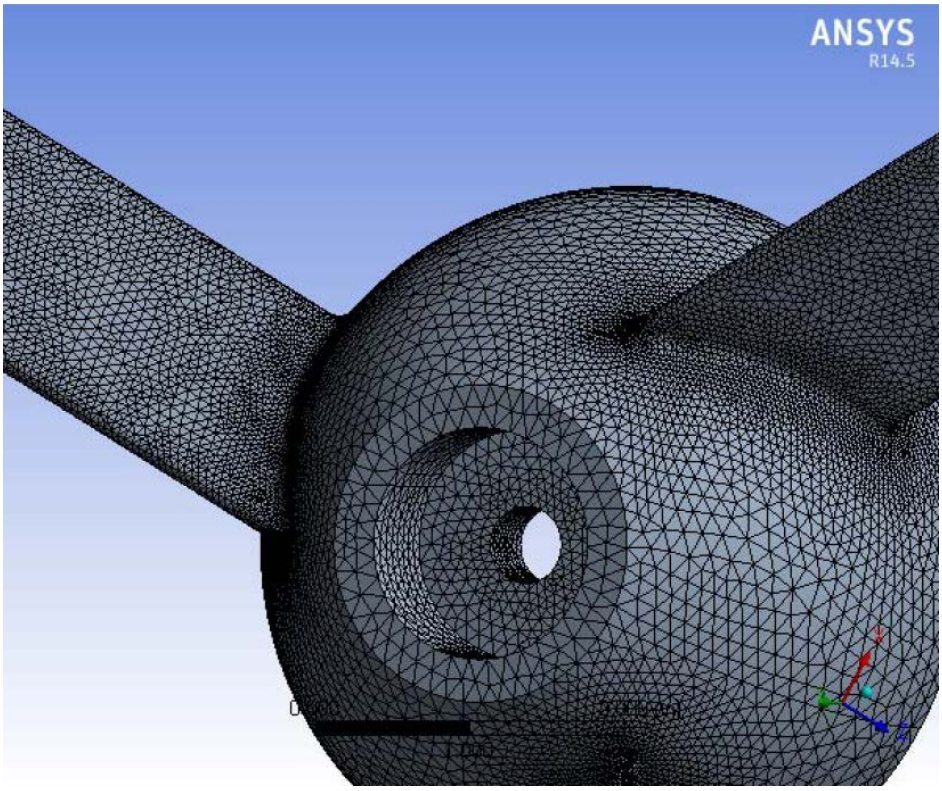

Figure 37. Meshed Baseline Impeller Model.

Let's now consider the shock response of our Baseline Impeller to various pulse widths of the acceleration input. In the analysis settings for transient response, large deflection effects are included, and filtering of the higher frequency content of the reponse is limited by 10%. For these cases, a 10 ms end time response is sufficient to capture all details of the transient reponse as seen in Figure 38. For this case in particular the initial time step is set at 0.2 ms, and the minimum time step is set at 0.1 ms. For the sharper shock inputs these time steps are decreased even further for better definition in the response. Figure 39 shows the maximum deformation of the impeller blades that occurs at 1.8 ms of the response, the same point in time shown in Figure 38 and

marked by the solid vertical line. Shadows of the undeformed blades can also be seen in Figure 39.

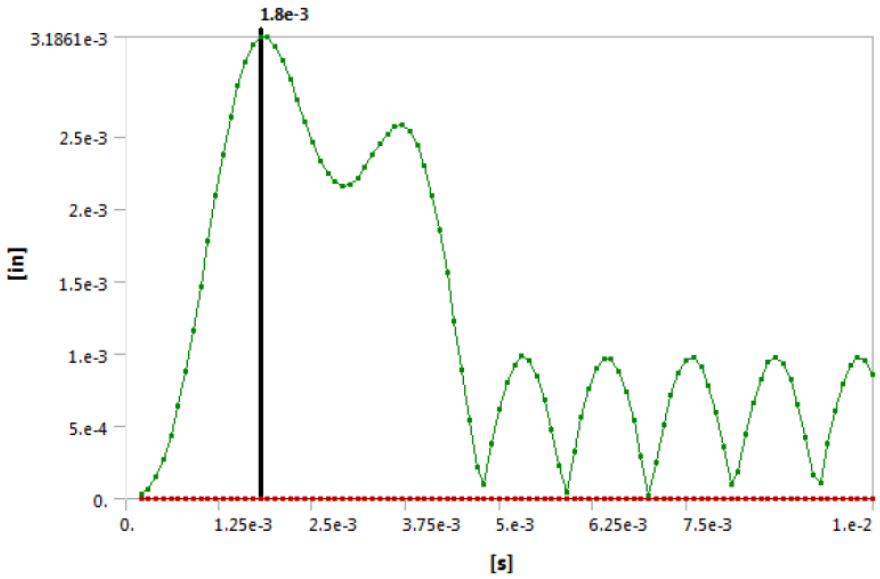

Figure 38. Maximum Baseline Impeller Response at the Blade Tips for a 50 g, 5 ms Input.

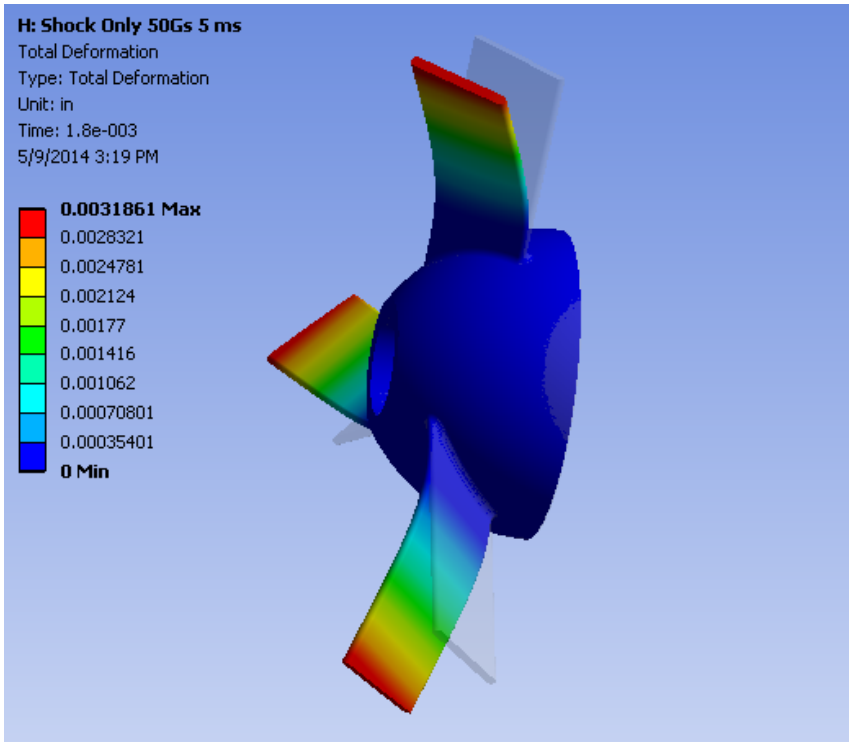

Figure 39. Baseline Impeller Undergoing a 50 g, 5 ms Shock Input, Deformed and Undeformed Blades Shown.

In this third and last study of effects of pulse width variations, the trend is similar to the previous systems. It has a peak, then gradually decreases until it converges to a minimum value for deformation and stress. Maximum values for total deformation always occur at the blade tips. For this case study we continue to track and compare deformation values as opposed to stress values which are included for reference only.

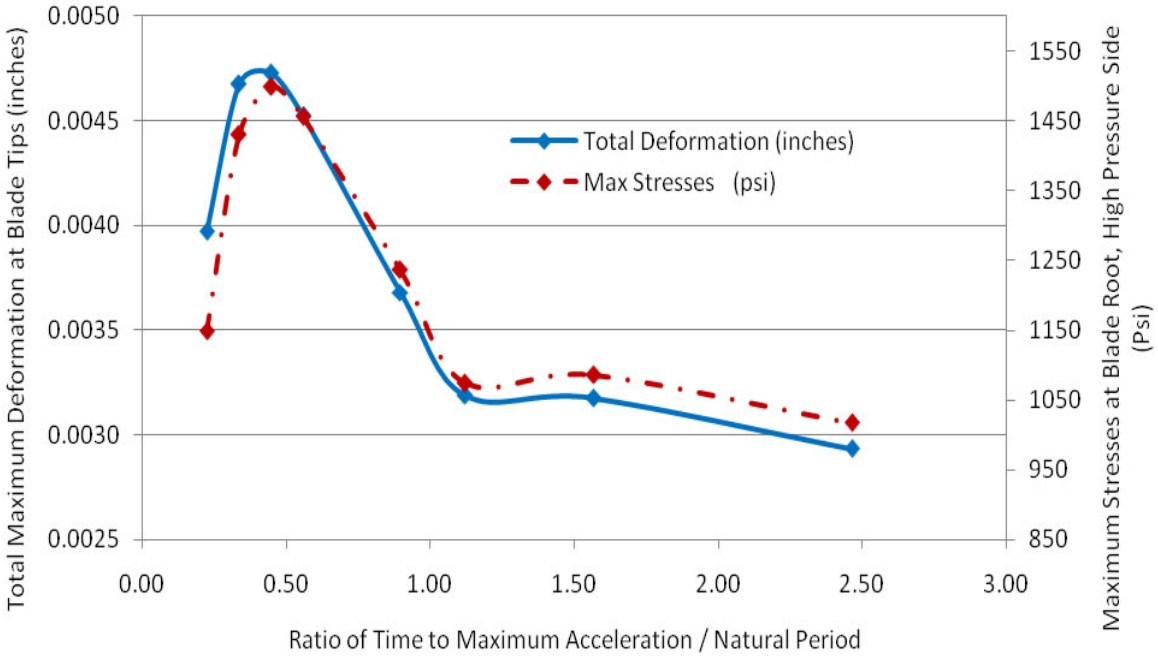

Figure 40. Baseline Impeller Sensitivity to Pulse Width, 50 g Shock, τ_n = 2.2 ms.

In this particular case, maximum total deflection of the impeller blade tips occurs during an acceleration pulse width of 2 ms, which corresponds to a TMA/Natural-Period Ratio of 0.45; for reference, the maximum total deflection at this point is 0.0047 inches as shown in Figure 40 and Table 12. Similarly, and from a separate study by J. Luo, *et. al* on a head actuator assembly subjected to the same type of input, the highest amplitude for the transient response occurs when pulse frequency is 0.66 of the natural frequency [15].

Maximum total deformation and stress values start to increase when this ratio is under 1.00. This Baseline Impeller was not designed to operate inside a real machine, but it does have representative mechanical characteristics as those from a real impeller in production; deformation and stress values are for relative comparison purposes but they are low when compared to the strength of 6061-T6 aluminum.

Table 12. Table of Values for Figure 41.

Pulse Width (ms)	Time to Maximum Input Acceleration (ms)	TMA/ Natural-Period Ratio	Max Stresses (psi)	Total Deformation (in)
1.0	0.50	0.22	1148	0.00397
1.5	0.75	0.34	1430	0.00467
2.0	1.00	0.45	1499	0.00473
2.5	1.25	0.56	1455	0.00453
4.0	2.00	0.90	1236	0.00368
5.0	2.50	1.12	1074	0.00319
7.0	3.50	1.57	1085	0.00317
11.0	5.50	2.46	1017	0.00293

4.3.2 Baseline Impeller Undergoing Rotation and Shock, Two Solution Methods

Properly analyzing an impeller subjected to a single shock input while undergoing rotation at the same time is often essential in the design of rotating machinery and it is discussed next. Two solution methods from Ansys are presented: using the Full Method to solve for the transient response and the Mode Superposition Method (Superposition) which involves using a combination of static, modal, and transient analysis. The latter method may not require a static analysis; however, in this case it is used for calculating deformation and stress due to centrifugal forces from rotation.

Large deflection and stiffening effects due to rotation are accounted for; otherwise, for the Baseline impeller in particular, deformations would be 19.4% higher. Time integration effects

are also included. This is important in transient analysis where transient effects such as structural inertia are taken into account where solutions at every time step are based on a previous solution. With Time Integration turned off, the system response is zero after the time dependent loading has ended. Next, let's compare differences and similarities between the Full Method and the Mode Superposition Method.

The Full Method uses the full system matrices to calculate the transient response (no matrix reduction). It is the more general method because it allows all types of nonlinearities to be included (plasticity, large deflections, large strain, and so on) [14]. The main disadvantage of using this method is that it takes a considerable amount of time and computer resources to solve, relative to the Mode Superposition Method; it could take many hours or several days, whereas the latter method could takes a matter of minutes. Per the *Ansys Mechanical APDL Structural Analysis Guide*, advantages of the Full Method are:

- It is easier to use because you do not have to worry about choosing mode shapes.
- It allows all types of nonlinearities.
- It uses full matrices, so no mass matrix approximation is involved.
- All displacements and stresses are calculated in a single pass.
- It accepts all types of loads: nodal forces, imposed (nonzero) displacements (although not recommended), and element loads (pressures and temperatures) and allows tabular boundary condition specification via TABLE type array parameters.
- It allows effective use of solid-model loads.

The Full Method solution is used on the Baseline Impeller to solve for the transient response. In the set up of this model, the impeller is simply fixed at the center bore for simplicity; the loading conditions imposed include a counterclockwise rotation of 10,000 RPM and an axial impulse of 50 g with a 5 ms pulse width; the shape of the impulse is a half-sine wave as shown in Figure 36. The acceleration of 0 g shown in Figure 41 is the acceleration for one of the other axes

which is in fact zero. In this kind of analyses, a fixed support or a frictionless support show equivalent results. In calculation of stresses and deflections due to rotation, the code simply applies the centrifugal force to all the nodes with degrees of freedom in the radial direction; a fixed support is used in this case. These loading and support conditions will be the same as used in the Mode Superposition Method.

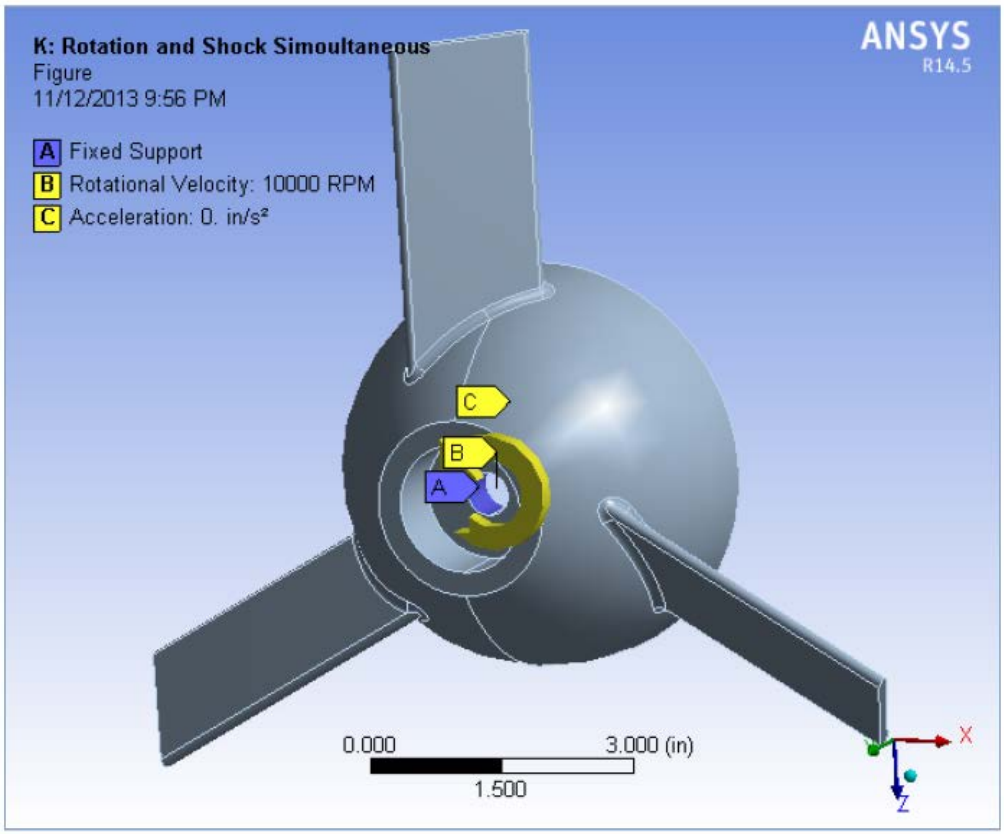

Figure 41. Initial Conditions for the Baseline Impeller Transient Analysis.

Figure 42 shows the location of the probe at the corner of the leading edge of the impeller blade tip. Tracking results at this location is helpful since it provides a discrete reference point for comparing deformation results between our two solver solutions.

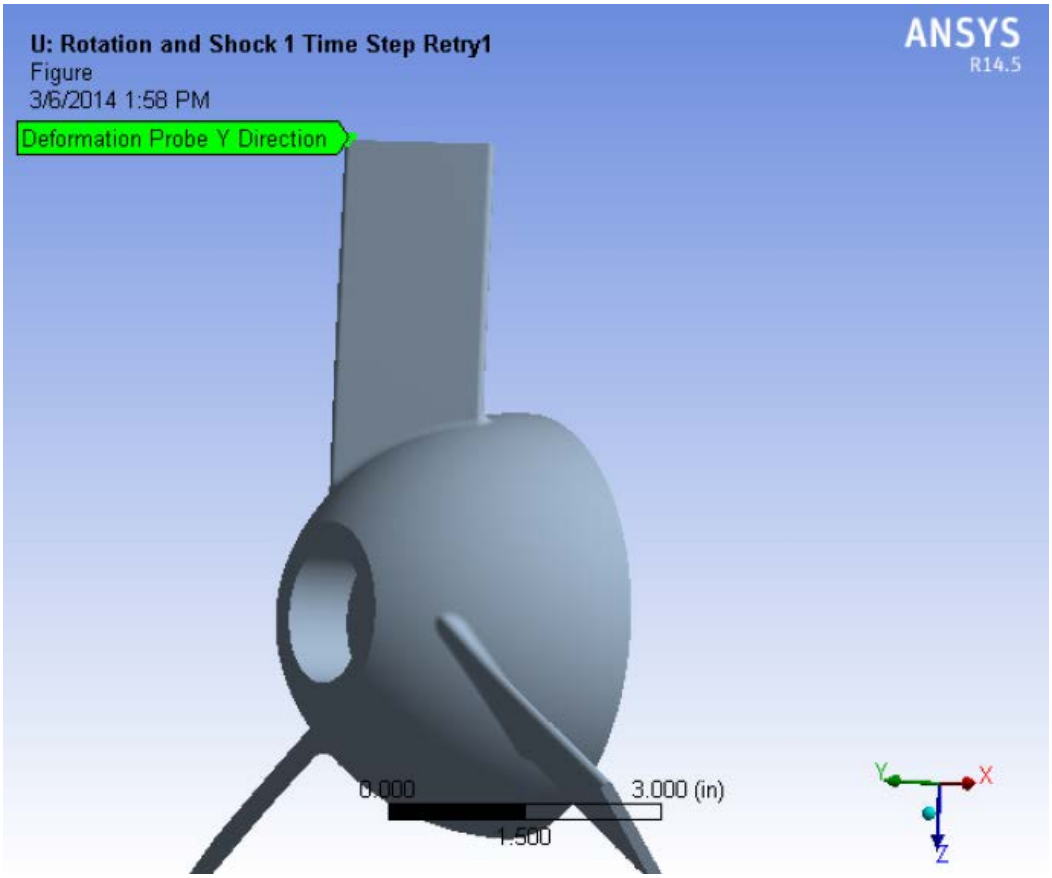

Figure 42. Probe Location for Axial Deformation Calculations.

Rotation causes deflections of the blades in the negative Y directions or rearward axial direction. The shock is in the negative Y so the response to the shock is in the positive Y direction; this impulse reaches a peak at 10.5 ms and it is approximately at this time that the maximum deflection is influenced by the shock response as seen in Figure 43. Deflections due to rotation and shock act in opposite directions. The response from the shock input is not large; in this case study, our only concern is the accuracy of the response and process. Also, for sake of comparison, only axial deflections are studied since these are a better point of reference relative to stress values, which may change locations depending on the sharpness of the shock.

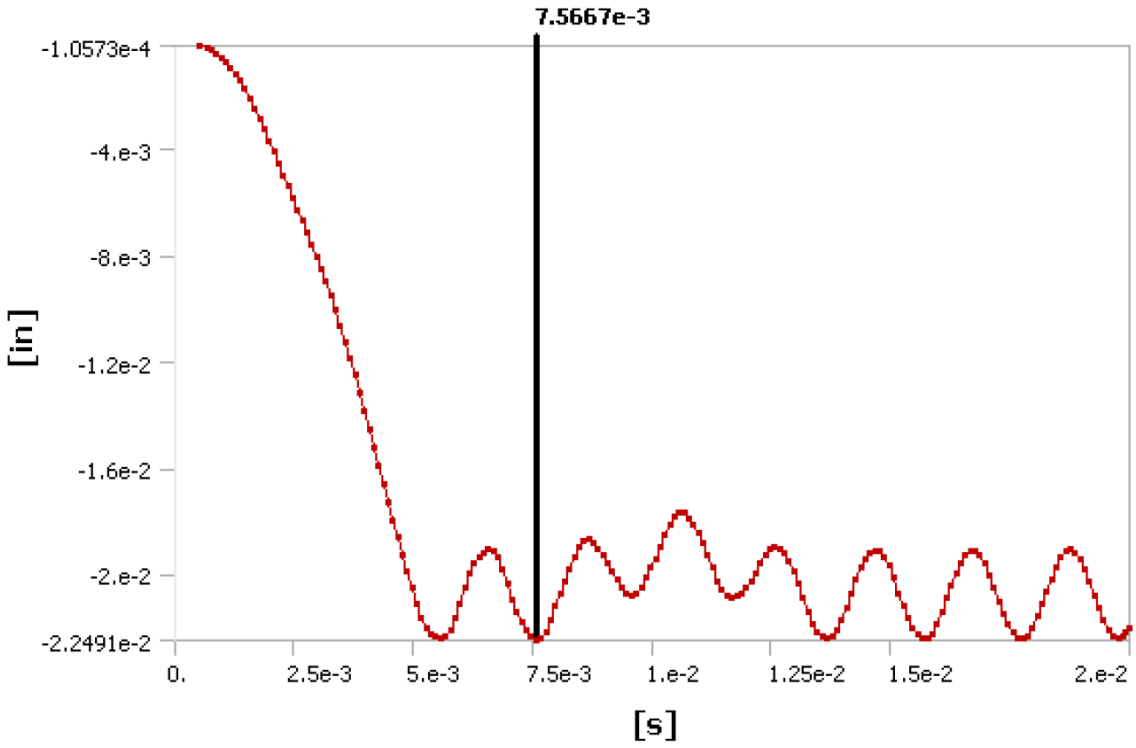

Figure 43. Full Baseline Impeller Model Solution for Axial Tip Deformation from Simultaneous Rotation and Shock Loading.

When using the Full Method, it is important to note that both the rotation and shock responses are combined and included in the same graph; this is not the case in Mode Superposition. As seen in Figure 43, an excellent resolution is obtained in this solution by using a 0.5 ms time step and a 0.1 ms minimum time step. The axial deformation at the time of the maximum acceleration input and when the impeller is already undergoing rotation is 0.01768 inches; in this particular case, the response of the shock happened to be in the opposite direction relative to the response to rotation as mentioned earlier, thus deformations decreased at the time of the shock. After the shock subsides, the steady state response of the system has a minimum deflection of 0.02249 inches beyond 15 ms.

The Mode Superposition Method takes the eigenvalues and eigenvector solutions from modal analysis and creates a transient response using a preselected number of modes. Per *Ansys Mechanical APDL Structural Analysis Guide*, disadvantages to this method include:

- The time step must remain constant throughout the transient, so automatic time stepping is not allowed.
- The only nonlinearity allowed is simple node-to-node contact (gap condition).
- It does not accept imposed (nonzero) displacements.

Some advantages are:

- It is faster and less expensive than the Full Method for many problems.
- Element loads applied in the preceding modal analysis can be applied in the transient dynamic analysis via the LVSCALE command.
- It accepts modal damping (damping ratio as a function of mode number).

The Mode Superposition Method is also used to solve the transient response of the Baseline Impeller undergoing the same loading and same support type from the Full Method discussed previously. When running this method, a similar solution is obtained relative to the Full Method yet it only takes a fraction of the time to solve. The main difference is that in the Mode Superposition Method, the analysis is broken down in several parts. In this case, three separate analyses were integrated: static, modal, and transient analyses. These separate analyses are performed in that order. Once solutions for the different systems are obtained, the total deformation values for the same locations are added to obtain an overall value. Knowing individual responses for discrete points and times could be beneficial to help understand which loading is more critical. The meshed model used is seen in Figure 37. The Ansys Workbench model used to set up the Mode Superposition analysis of the Baseline Impeller is shown in Figure 44; this model shows how the static solution is the pre-stressed condition for the Modal Analysis, and this in turn is the initial condition for the transient model where shock loading is carried out.

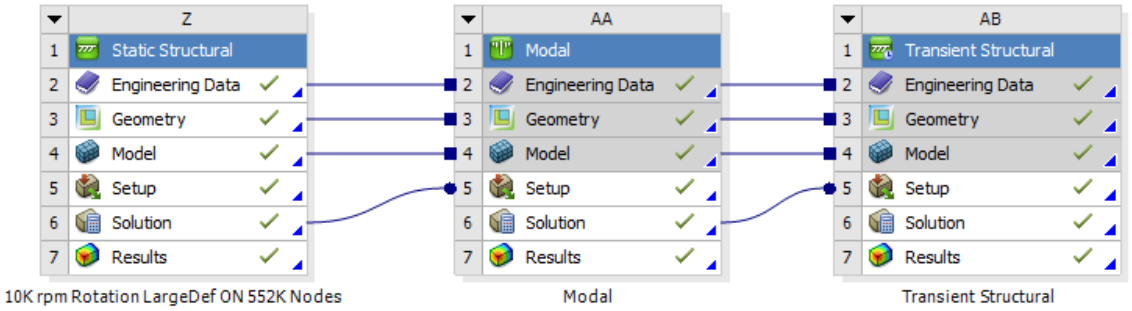

Figure 44. A Mode Superposition Model from Ansys Mechanical.

In the Mode Superposition Method for this case study, we start with static analysis to determine the effects due to the impeller rotation only. Centrifugal loading due to rotation is analyzed for a rotation of 10,000 RPM with a fixed support at the center bore, which is equivalent to a frictionless support. This loading is ramped over a period of 1 second.

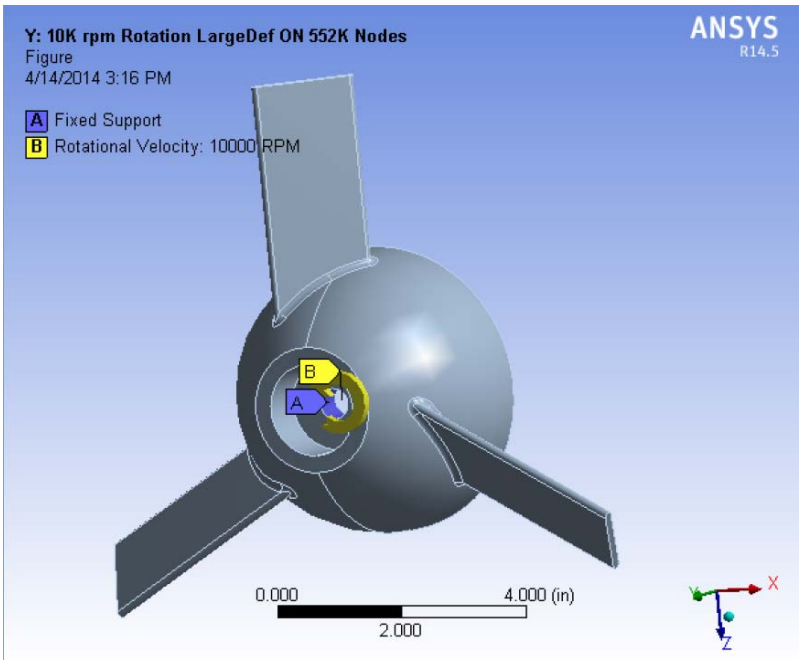

Figure 45. Static Analysis Performed as Part of Mode Superposition Method.

The axial deformation solution from the static analysis calculates a maximum axial deformation of 0.02161 inches at the leading edge tip of the impeller blades; these deflect in the

forward axial direction as shown in Figure 46. Deflection at the location of the probe seen in Figure 42 is -0.02088 inches, which is slightly different than the maximum value since the probe is not located exactly at the tip of the blade. Large deflection effects are accounted for since rotation stiffens the structure slightly which also has an effect on modal frequencies.

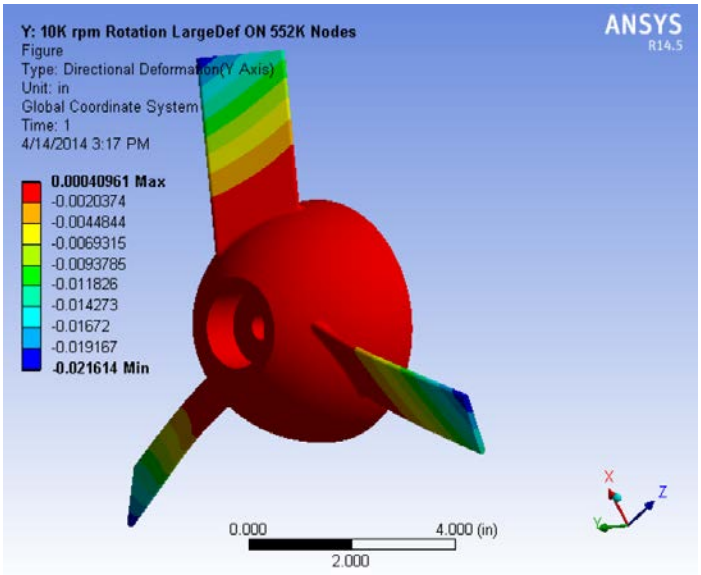

Figure 46. Baseline Impeller Axial Deformation due to Rotation Only as Part of a Superposition Three Step Solution.

Next, solution results from the static case are linked to the modal analysis. Twenty modes are solved for in this analysis with a frequency range of 400 Hz to 10000 Hz. This range is selected based on prior knowledge since we know the fundamental frequency of the impeller blades is above 400 Hz. This mode shape is the most important to account for since it is easiest to excite during testing and operation. With large deflections turned ON, as must be done for fast rotating parts such as impellers, the fundamental frequency occurs at 495 Hz which is almost 50 Hz higher compared to large deflections turned off. Higher bending and twisting modes also contribute to the overall response. Figure 47 shows the solution of 20 modes in the frequency range specified; the corresponding frequencies are included in the vertical axis. Three modes

occur for each frequency, corresponding to each of the three blades; in other words, it is the same mode occurring once for each blade.

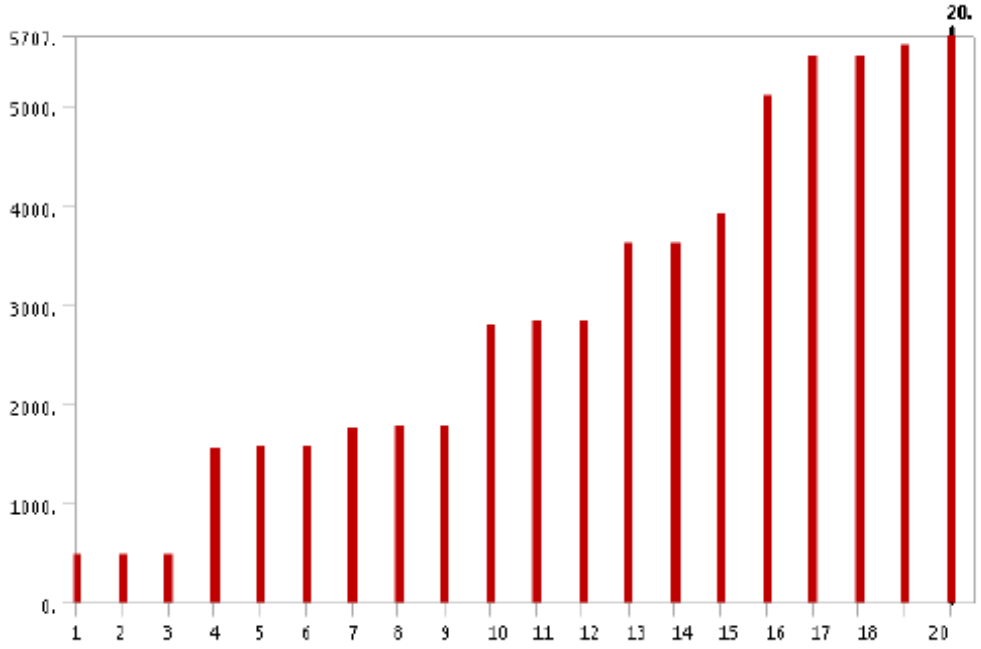

Figure 47. Baseline Impeller Modal Frequency Solution under a Pre Stressed Condition.

In the modal analysis solution for this Superposition Method it is important to check the effective mass participation in the primary loading direction; it is important to have at least 90% or better to ensure enough modes are participating in the overall response. Shock loading occurs in the axial Y direction and the calculated effective mass participation in this axial direction is 95.15% from the solver output solution.

The final analysis in Mode Superposition is the shock analysis for which the initial condition is the modal solution. The support conditions from the static analysis carry through as well. A time step of 0.1 ms is selected and provides enough definition throughout the curve. Figure 48 shows the transient axial response of the Baseline impeller to the shock input were the probe is located per Figure 42; again, the shock is in the negative axial direction and response is

in the forward axial direction as expected; it reached a maximum value of 0.0017 inches. The overall solution for axial deformation everywhere in the model is shown in Figure 49.

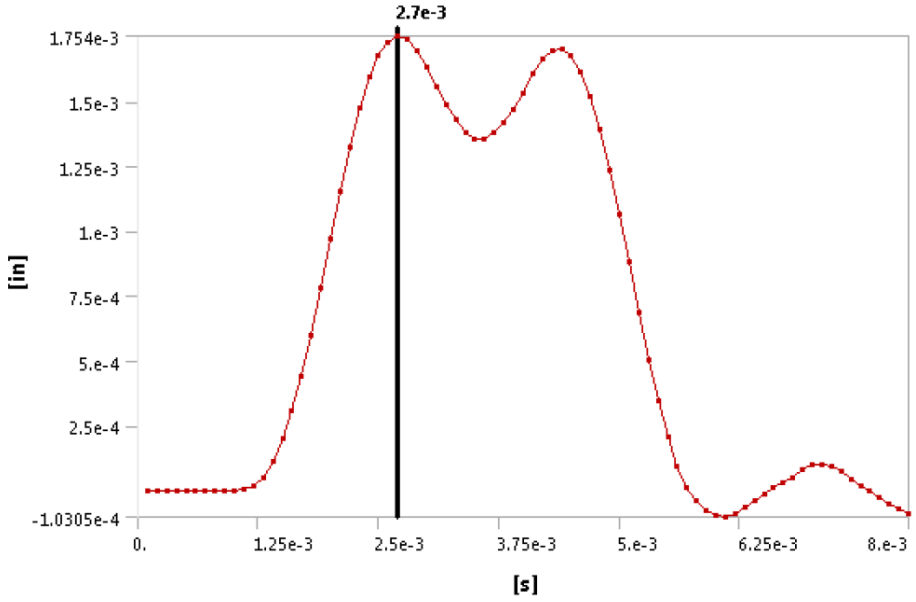

Figure 48. Axial Deformation at the Probe from Final Results from a Mode Superposition Solution.

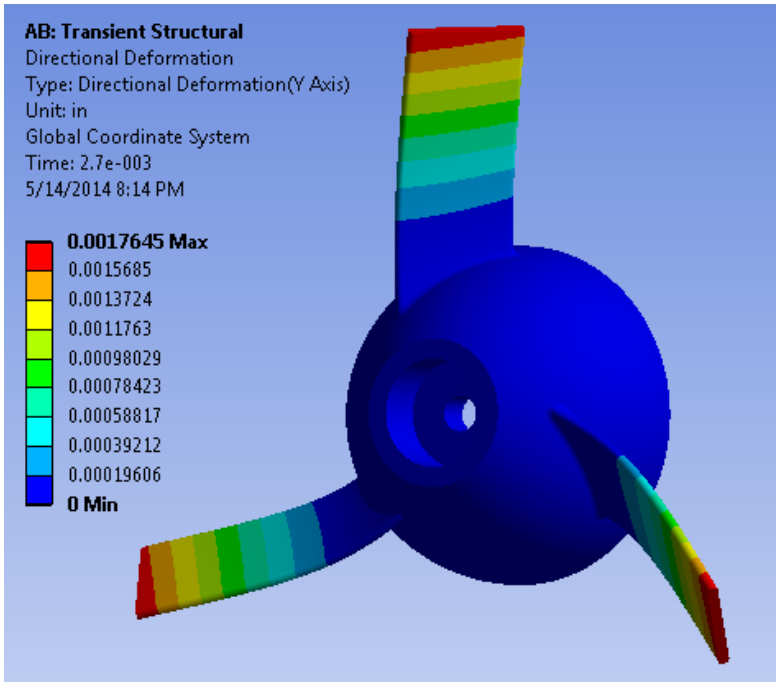

Figure 49. Axial Deformation Impeller Profile in the Final Results from a Mode Superposition Solution.

Adding the values for axial deformation, obtained from the Mode Superposition Method, at the location of the probe due to rotation and shock at 2.7 ms equates to:

$$- 0.02088 + 0.001754 = -0.0191 \text{ inches}$$

The corresponding value obtained using the Full Transient Method is -0.01768 inches; the difference in results between both methods is only 0.0014 inches for this case study.

In conclusion, the Mode Superposition Method helps tremendously with quickly evaluating changes in the 3D model and fine tuning the design; additionally, it leaves enough computer resources available to do other engineering tasks. A computer running a Full Method solver would most likely use most of the computer memory and processor power available. A Superposition Method solution allows more visibility into deformation and stress effects caused by each loading condition; changes on these loading conditions can be easily studied independently. The Full Method solution is ideal when there is little time to set up a model and when a solution is not needed right away.

4.3.3 Summary of Chapter 4

Three case studies were completed in Chapter 4: Glass Panel Undergoing a 4 g Acceleration, The I508 IGV, and Baseline Impeller Shock Analysis. An important comparison was made between two different methods available for solving shock analyses: the Full Method and Mode Superposition Method. Many sensitivity studies related to shock analysis were conducted including using static analysis as a substitute for shock analysis, analytical modal analysis of impeller blades modeled as cantilevered beams, and effects of varying acceleration pulse widths from acceleration inputs.

The study of using static analysis in place of transient analysis for evaluation of shock concluded that differences in results could be significant if the maximum input loading duration is similar or less than the natural period of the structure. Furthermore, the energy content of the input is another parameter that can influence the structural response which would only be evident

from a transient analysis. In the theoretical modal analysis of impeller blades modeled as beams, results showed that the mode frequencies of the first three modes were 10.5% or better when compared with finite element results of the blades modeled as integral parts of the impeller. Therefore, a quick theoretical modal analysis can be incorporated as a preliminary step in the initial design process of impellers and their vibration response.

A study of the variation of pulse width of acceleration inputs on different systems was completed; The Glass Panel and Baseline Impeller test cases showed similar trends, the Inlet Guide Vane Housing less so. This study shows that the structural response has a large amplitude when the time to maximum acceleration of the input (TMA) is a fraction of natural period; these curve peaks can be seen in Figures 21 and 40. When the TMA and the natural period are very similar, the response of the structure reaches a low amplitude range. The plateaus, which may become nearly constant, can also be seen in Figures 21 and 40, as well as in Figure 27.

The results from all of these studies must be kept in mind during several phases of the life of a structure, including during the design phase. When designing parts or systems to withstand shock, "we will find that structures that deal with shock well are not particularly good with regard to steady-state excitation and vice versa. Once again, this is a classic case of how we must carefully consider the different factors of a design, weigh their importance, and then come up with the best overall design that produces acceptable performance in all relevant categories [10]".

CHAPTER 5

EXPERIMENTAL AND ANALYTICAL SHOCK TESTING OF THE H200 MIXED FLOW FAN

A Mixed Flow Fan is evaluated analytically and experimentally for shock conditions per Military Standard MIL STD 810. A key focus of mechanical design of rotating machinery is to maintain tight blade tip clearances while simultaneously avoiding any potential tip rub or impact against the fan shroud due to impulse loadings or any other operating conditions. The shock testing required by this military standard describes three different levels of tests in three separate orthogonal directions as shown in Table 13. These types of shock inputs correspond to road, gunfire, and ballistic shock levels that military equipment must be able to withstand without failing to maintain operational capabilities. All major components of the fan assembly are analyzed according to the shock inputs included in Table 13. FEA results show that the ballistic shock causes the most deflections; for example, impeller ballistic shocks are 1.9X and 2.4X more severe in terms of deflections when compared to the gun firing and the road load shock, respectively. Analyses of all applicable components in the mixed flow machine, for the ballistic shock only, are discussed in the following sections. The cylindrical coordinate system is often used in these finite element models; the radial direction is comprised of both the lateral and vertical directions from the Cartesian coordinate system.

Table 13. MIL STD 810 Shock Requirements Using a Half Sine Input.

Shock Load Type	Amplitude (g)	Pulse Duration (ms)
Road Load	20 ± 3	11.1 ±1.1
Gunfire	25 ± 5	1.5 ±0.2
Ballistic	50 ± 8	0.5 ±0.1

5.1 Analytical Results

The assembly and associated components are analyzed for shock loading using finite element analyses, theoretical calculations, careful measurements, and manufacturer's tolerance specifications. A cross section of the fan assembly is shown in Figure 50 and describes the major components of this machine. Analysis of the assembly is complex, due to point contact of the ball bearings inside the bearing rings; this analysis is separated into four major parts to mitigate the complexity: analysis of the impeller-rotor subassembly, the front bearing housing (FBH), the ball bearings, and the remaining non-rotating structure which includes the fan shroud, in particular, along with the motor support, diffuser, and mounting bracket. These analyses focus on determining the maximum potential risk for impeller blade contact against the shroud. In particular, these analyses focus on deflections that could most likely cause a blade tip strike; two locations are investigated: axial deflections at the blades trailing edges (TE) at the outside diameter of the impeller and radial deflection at the blades leading edges (LE) as indicated in Figure 50.

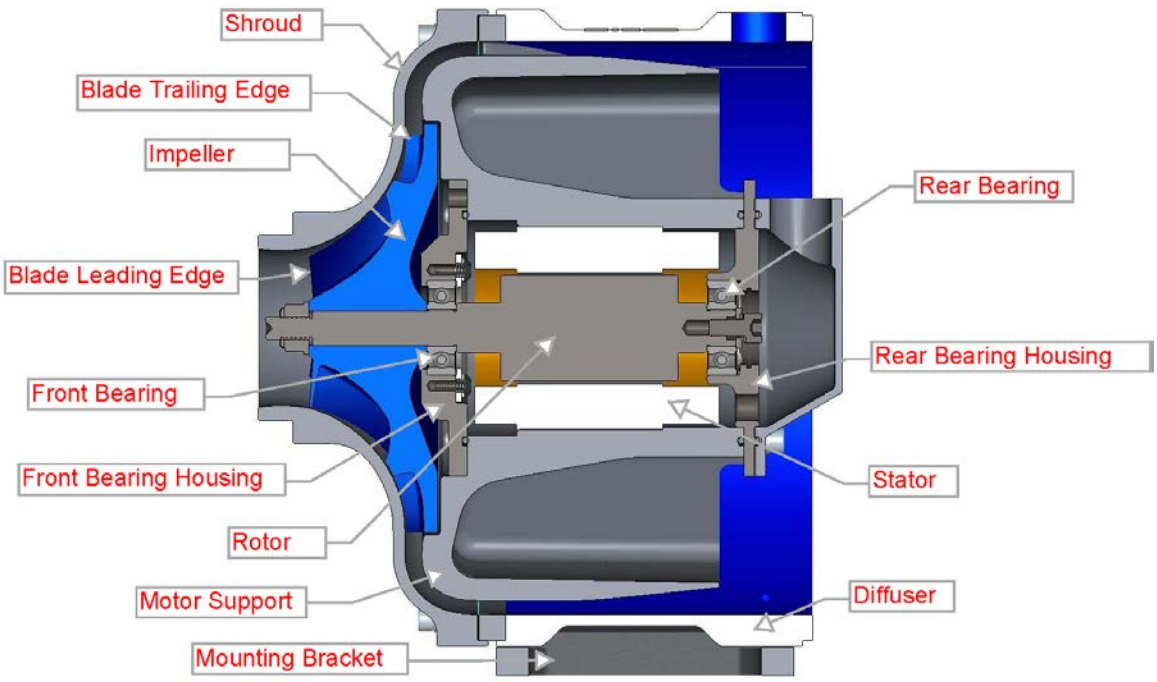

Figure 50. Cross Section of Mixed Flow Fan Assembly for Illustration Purposes.

5.1.1 Impeller and Rotor Subassembly

Analyses of the impeller-rotor include shock loading as well as rotational and aerodynamic effects. The impeller material is 6061-T6 aluminum and the rotor spindle is 17-4-PH stainless steel. The configuration of this rotor is an overhung type rotor with significant mass at the front end; the moments that are induced by a shock in one direction do cause deflection in an orthogonal direction as well. The boundary conditions of the model include two fixed supports at both bearing journals of the rotor. The impeller is securely fixed to the rotor by a shrink fit; thus, this connection is defined as bonded. All shock loads are analyzed in two different directions: axial and radial. The rotor has radial symmetry; therefore, vertical and lateral shocks are equivalent to a radial shock.

The Full Method for transient analysis is used for this impeller-rotor subassembly; the loading conditions in this model include a ballistic shock input, as well as centrifugal and aerodynamic effects. Fine meshing is driven by a curvature definition of 45°, a maximum element size of 0.100 inches, and a growth rate of 1.50. In the analysis settings, the solution is divided in two time steps: a lower definition time step for the static loads and a finer definition second step for the transient shock load. This allows for a more efficient solution in the shortest amount of time possible using a Full Method. A time delay is implemented for the ballistic shock input which starts sometime after the end of the rotation and aerodynamic loading as shown in Figure 51.

Figure 51. Impeller and Rotor Shaft Analysis Settings in Two Steps; Step 1 includes Rotation and Aerodynamic Effects and Step Two includes the Ballistic Shock Input.

Figure 52 includes the axial deformation distribution of this subassembly; maximum deflections are shown in dark blue at the outer diameter of the wheel; the rotor is hidden for clarity but it is included as part of the finite element model. The units are inches and the solution shown is at 5.447 ms which is when the maximum deformations occur as shown in Figures 52 and 53.

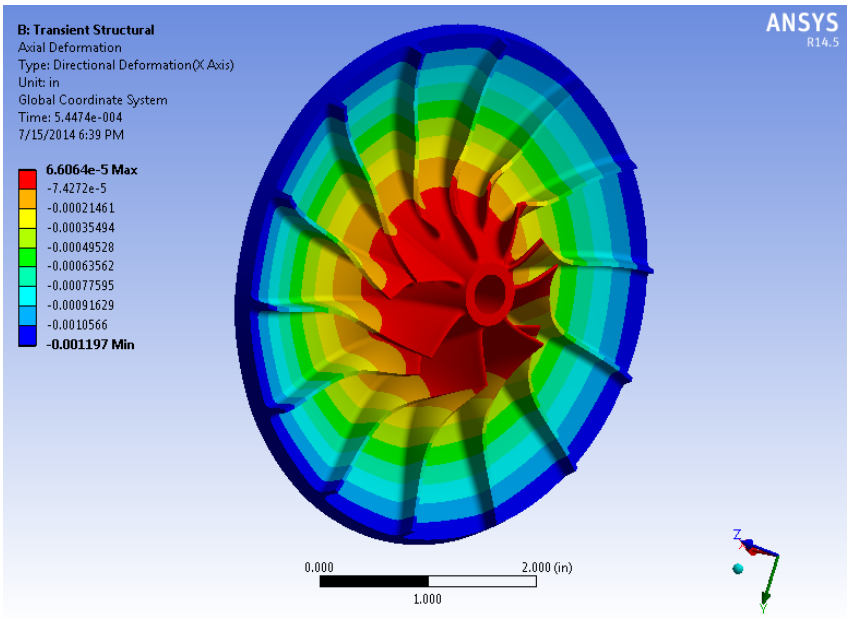

Figure 52. Impeller and Rotor Shaft Axial Deformation Results for the Axial Ballistic Shock, Rotational and Aerodynamic Loading Also Included (the Rotor part is hidden).

Deformations due to the ballistic shock are small compared to those caused by the centrifugal force. In fact, deformations due to shock are hard to detect in the solution in Figure 53; the maximum acceleration input occurs at 9.5E-4 seconds and there is barely any change in the overall response in Figure 53. For reference, when modeled separately, Figure 54 shows the axial deformation of the trailing edge tips due to the ballistic shock only; there are two orders of magnitude difference between this and the rotational effect.

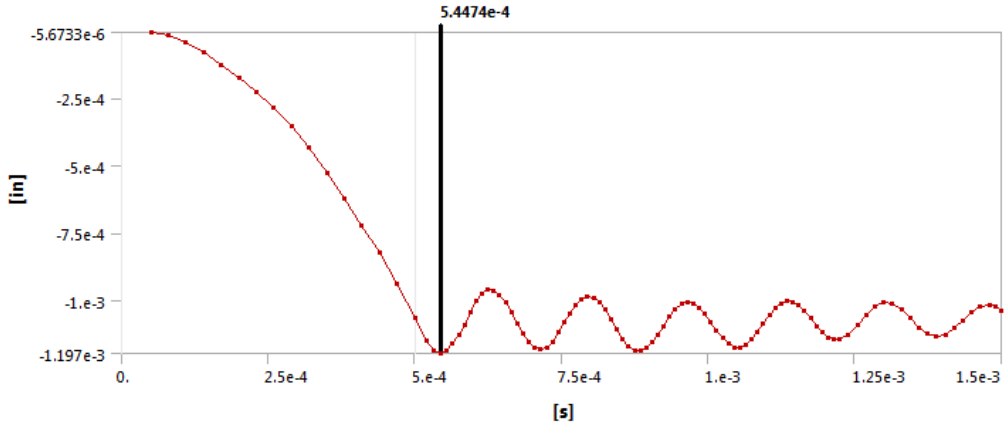

Figure 53. Impeller and Rotor Shaft Maximum Axial Deformation Results for the Axial Ballistic Shock, Rotational and Aerodynamic Loading Also Included.

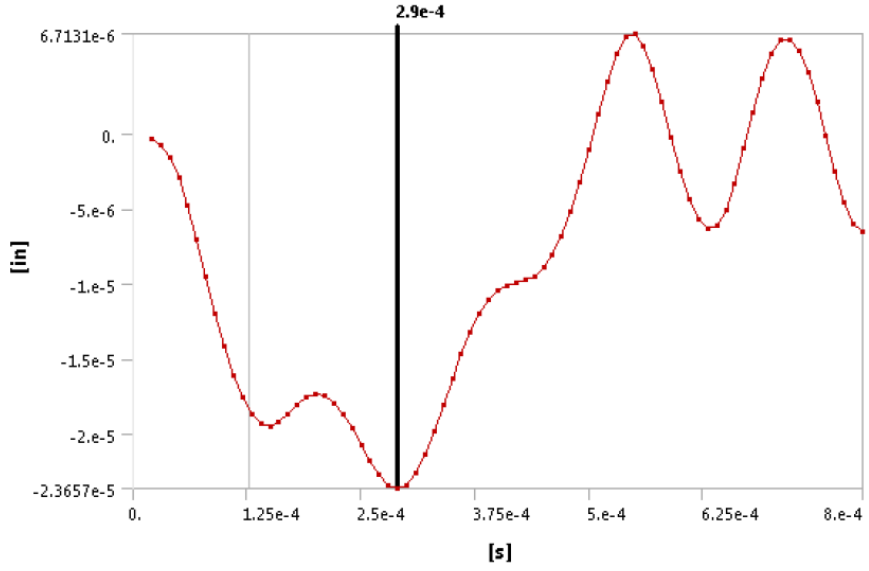

Figure 54. Impeller and Rotor Shaft Maximum Deformation Results for the Axial Ballistic Shock Only.

Maximum axial and radial deformation results for this subassembly are included in Table 14; these values include the ballistic shock, rotational, and aerodynamic effects. Radial deformations due to rotation and thrust are negligible at the blades' leading edges at the front of the impeller; the radial deflections shown are mostly due to the radial ballistic input.

Table 14. Impeller-Rotor Results for Maximum Deflection For A Ballistic Shock, Rotational and Aerodynamic Loading Also Included.

Shock Input	Ballistic
Axial Shock, Forward Deflections at TE Tip >	1.18E-03
Radial Shock & Radial Deflections at LE Tip >	2.13E-05

5.1.2 Front Bearing Housing

Analyses for the front bearing housing are also carried out in the axial and radial directions for all the shock inputs; results are included in Table 15. The rotor and rear bearing are floating at the rear bearing housing and are considered unconstrained. The front bearing housing material is 303 stainless steel; this housing is shrink fitted radially to the motor support and is also fastened by six 8-32 screws; the front ball bearing is tightly fitted inside the main bore of the housing. These analyses are carried out using the Mode Superposition Method; this part is less complex than the others, thus performing a preliminary modal analysis to identify the fundamental modes and mass participation is not difficult. Analyzing shock response using transient analysis is time efficient.

The boundary conditions include a fixed support at the six 8-32 tapped holes as well as at the axial supporting surface. Part of the boundary conditions at the main bore include the weight of the impeller-rotor subassembly, a forward bearing preload, and the axial forward fan thrust.

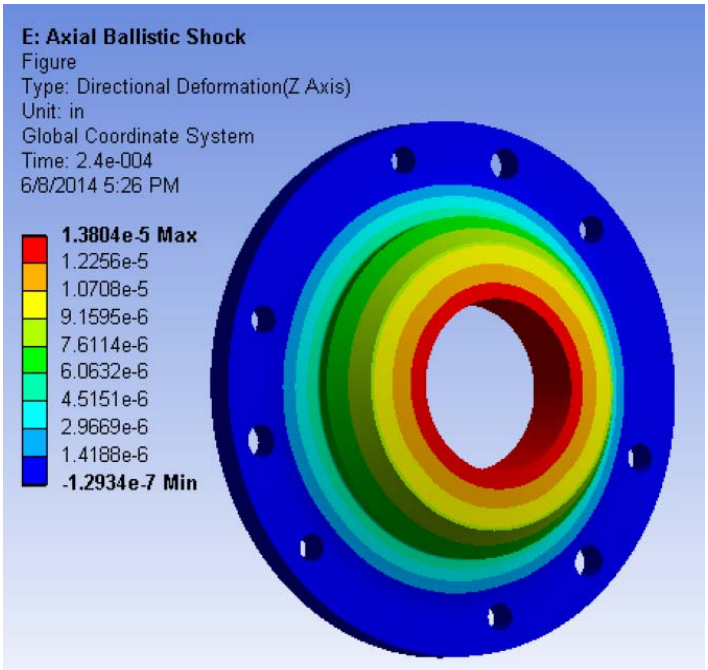

Figure 55. Front Bearing Housing Lateral Deformation due to the Lateral Ballistic Shock.

The maximum deformation for this component also occurs at peak of the shock input and it is higher when the shock is in the rearward axial direction as expected; deformation values and contours can be seen in Figure 55 and Table 15.

Table 15. FBH Results for Maximum Deflection For All Three Types of Shock (Inches).

Axial Shock and Axial Deflection	1.40E-05
Radial Shock and Radial Deflections	1.40E-06

5.1.3 Fan Shroud

Analyses of the stationary overall structure, which includes the fan shroud, are performed using the Full Method of transient analysis. The main objective is to determine the maximum inward deformations of the shroud near the impeller blades and the blade tips in particular. At the

entrance of the fan shroud, near the blade leading edges, the radial deformations are important since the impeller gap is radial; similarly, near the blade trailing edges, shroud axial deformations are important since the impeller gap is axial at this location. Everywhere else along the blade length or blade chord, the impeller gap is angular.

Table 16. Maximum Deformation of Fan Shroud in the Fan Assembly.

Shroud Deformations, Ballistic Shock			
Direction of Shock	Radial (Lateral) Deformation At Entrance (in)	Location	Relative Axial Shroud Deformation At the Impeller Trailing Edges Near the Maximum OD (in)
Axial	4.40E-04	Circular entrance deforms, sometimes into an oval shape, where sides move towards the center.	~0
Vertical	8.50E-05		2.10E-04
Lateral	2.00E-03		~0

It is important to perform analysis for shroud deflections as part of the overall structure and not by itself due to the boundary conditions and the moments induced from shock inputs. The fixed boundary condition is defined at the mounting bracket or base of the fan. For example, when the shock is in the axial direction, and since the CG of this structure is above the bracket, the fan response is to "pitch" about an axis perpendicular to the page as seen in Figure 56. Maximum deformation results for a ballistic shock input in all three directions are included in Table 16. The maximum lateral deflection at the shroud entrance occurs in the lateral shock direction; Figure 56 shows the shroud contours for the outside of the shroud. In terms of the axial deformation near the blade trailing edges, there is absolute deflection of the structure; however, relative values are approximately zero for the axial and lateral shocks, since most of the structure deflected similar amounts in the same direction. During the vertical shock there are some minor axial deformations.

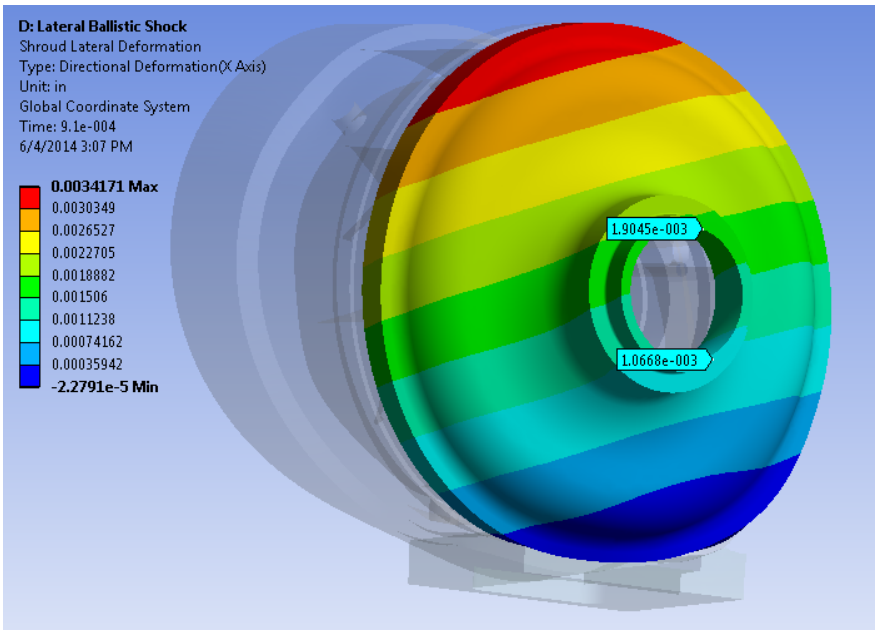

Figure 56. Fan Shroud Lateral Deformation from a Lateral Ballistic Shock, Highly Deformed Model Shown for Illustration Purposes Only.

5.1.4 Rolling Element Bearings

Deformation of the ball bearings is analyzed theoretically using the Hertz contact theory for a sphere in contact with a non-conforming surface to represent the balls and bearing rings. Under no load this is a single point contact that develops relatively high stresses when pressure develops due to normal loading. Figure 57 shows the normal deformation (α) that is calculated for a ballistic shock condition. These single row deep groove type bearings include seven ceramic balls, inner and outer rings made from bearing steel, a crown cage, synthetic grease and two high temperature resistant contact seals. The overall dimension of the bearing is 10 mm I.D. x 26 mm O.D. x 10 mm in width. Measured diameters of the bearing balls are all 4.76 mm.

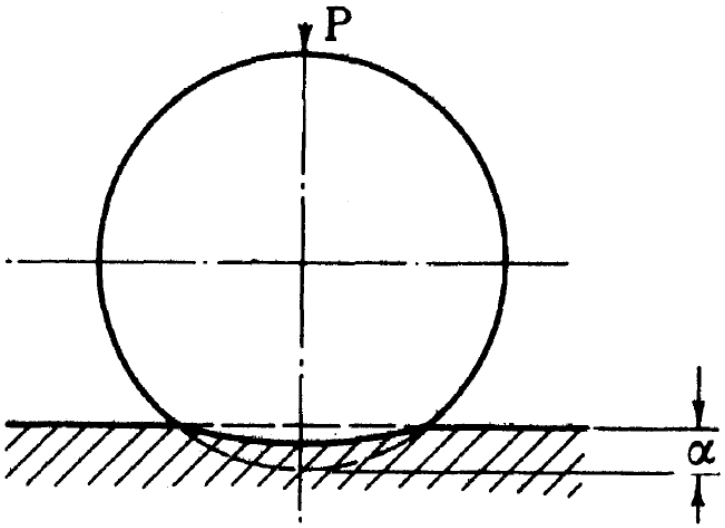

Figure 57. Hertzian Contact between a sphere and a non-conforming surface [19].

In calculating the normal deformation, it is assumed that the ball and ring materials remain in the elastic range and are homogeneous, and that both surfaces are frictionless. The ball bearing point contacts are also simplified as spheres on flat surfaces; this is the closest case for which formulas are available. Furthermore, a static analysis is conducted rather than a transient analysis and it is deemed reasonable enough since the fundamental frequency of the associated components is extremely large in the order of hundreds of thousands of hertz. The frequency of the load at the peak amplitude is 4000 Hz, the equivalent period is 0.25 ms. Per Hertz contact theory, P_0 defines the maximum contact pressure and *a* is the contact radius. "Δ is a function of Young's modulus *(E)*, and Poisson's ratio (ν) for the contacting bodies 1 and 2 [18]." When one of these bodies is a plate, its radius R is approximated as infinite in magnitude. For the ballistic shock, the maximum pressure developed at each ball is approximately 8.3 Gpa, and the contact radius is 0.189mm.

$$\Delta = \frac{1-\nu_1^2}{E_1} + \frac{1-\nu_2^2}{E_2} \qquad \text{(Eq.46)}$$

$$P_0 = 0.578\sqrt[3]{\frac{\left(\frac{1}{R_1}+\frac{1}{R_2}\right)^2}{\Delta^2}} \quad \text{(Eq.47)}$$

$$a = 0.908\sqrt[3]{\frac{P\Delta}{\left(\frac{1}{R_1}+\frac{1}{R_2}\right)}} \quad \text{(Eq.48)}$$

The deformation due to the point contact of the balls on the bearing races (α) is defined as "the total compression at the point of contact of two bodies, measured along the line of the applied force [19]" and is calculated by formulas (Eq.49) and (Eq.50). Using these formulas, the approximate deformation is 0.00084 inches for the ballistic case.

$$\alpha = \frac{(3\pi)^{2/3}}{2} P^{2/3} \left(V_1 + V_2\right)^{2/3} (1/D)^{1/3} \quad \text{(Eq.49)}$$

$$V = \frac{(1-\upsilon^2)}{\pi E} \quad \text{(Eq.50)}$$

Ball bearings include internal clearances from the manufacturer and it is specified as a radial internal clearance in the part number of each bearing; NSK deep groove ball bearings are available in five different radial clearances. Figure 58 shows how the radial and axial bearing clearances are defined; it is the relative displacement of one ring relative to the other. These clearances allow for bearing expansion and contraction due to installation or operational effects. For normal operation, however, and also to offset normal wear during service, this clearance is eliminated by preloading both bearings. For this fan, the applicable radial and axial clearances are 0.00091 inches and 0.00238 inches respectively. An axial bearing displacement is only possible for a forward acceleration or shock, in which case the bearings and rotor arrangement would displace rearward. This does not contribute to increasing the risk of impeller contact with the shroud.

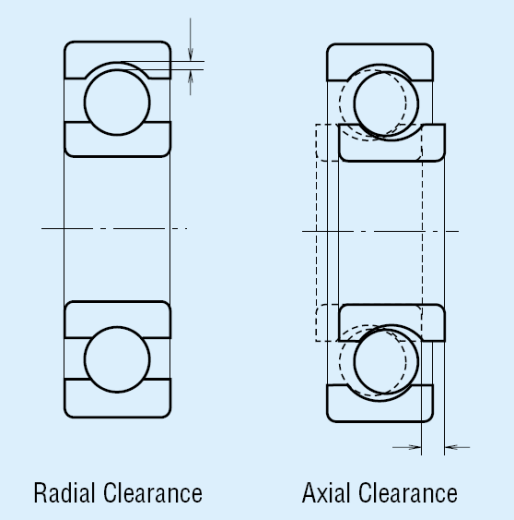

Figure 58. Ball Bearing Internal Clearances [17].

Bearing clearances are also there to account for any misalignment that may be present in the rotor spindle from the manufacturing process or from an adverse operating condition such as a shock in the radial direction. The measured maximum angular displacement present in a single bearing that is part of this assembly is approximately 1°. For a two bearing arrangement on the fan rotor, the maximum angular displacement is 0.034°. This accounts for the least material condition in the fit of the rear bearing. Figure 59 shows the set up for angular measurement of a single ball bearing. This angular range of motion of the bearing can translate into impeller deflections as well; the maximum axial deflection at the impeller trailing edges is 0.0013 inches and the maximum radial deflection at the impeller leading edges is 0.00087 inches.

Figure 59. Maximum Angular Displacement Measurement in a Single 10x26x8 mm Ball Bearing.

A steady state thermal analysis is also conducted on the impeller to determine the thermal growth due to increased temperatures during operation. Heat rejection through the impeller is a relatively small percentage compared to the total motor energy losses; regardless, it is important to determine how much these thermal effects contribute to closure of the blade tip clearances. A forced air convection of 100 W/(m^2K) is assumed on the front face of the impeller as well as 15 W energy dissipation. Radial growth at the tip of the blades leading edges at the entrance of the fan shroud is 0.0004 inches. Axial growth at the tip of the blades trailing edges is approximately 0.0001 inch since it is at a larger distance from the heat source.

5.1.5 Final Analytical Results for the Mixed Flow Fan

Taking all previous analytical results for the mixed flow fan into account, and as shown in Tables 17 and 18, the maximum radial and axial blade tip clearance closure during a ballistic

shock is 0.0042 inches and 0.0034 inches respectively. The radial closure occurs at the entrance of the fan shroud at the leading edges; the axial closure occurs near the tip of the blades trailing edges.

Table 17. Addition of All Radial Shock Deformation Results That Affect Tip Clearance.

Total Maximum Radial Closure of Blade Tip Clearance At Leading Edges At the Shroud Entrance. (Radial = Lateral or Vertical)	
From A Vertical Ballistic Shock (in) =	4.15E-03
From An Axial Ballistic Shock (in) =	1.71E-03

Table 18. Addition of All Axial Shock Deformation Results That Affect Tip Clearance.

Total Maximum Axial Closure of Blade Tip Clearance At Trailing Edges	
From A Vertical Ballistic Shock (in) =	2.79E-03
From An Axial Ballistic Shock (in) =	3.39E-03

5.2 Experimental Results for the H200 Mixed Flow Fan

The H200 fan was subjected to shock tests per MIL STD 810 and as described by Table 13. This machine was instrumented with three tri-axial accelerometers. One was located on the outside of the impeller shroud, one on the outside of the diffuser and one on the tail cone, shown in Figure 60. One uni-axial accelerometer was mounted to the slip table as the base input for the signal control. A tachometer was used to measure the fan speed. The H200 fan was run at a speed of 18,750 RPM during the shock tests and remained operational after the tests. After all the tests were completed, a detailed tear-down inspection of the unit was performed. The bearing assemblies were returned to the bearing manufacturer for detailed inspection.

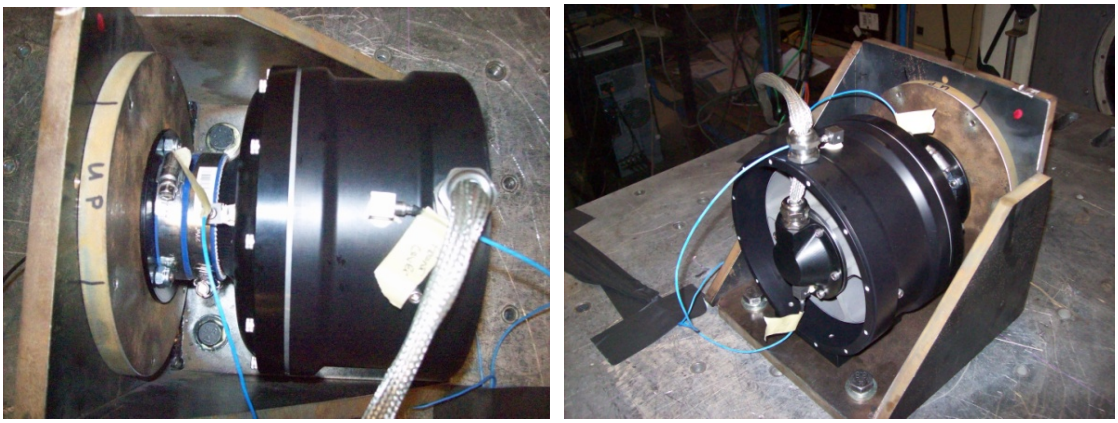

Figure 60. H200 Fan Instrumented with Accelerometers.

All shock tests and were performed using a 4,400 lbf electromagnetic shaker table (EMIC Model F-2000-BC-E07). Shock signals were supplied by an external controller, a Spectral Dynamics Inc. Puma Basic Version 4.0.0, build number 5403. The fan was mounted to the slip table using a ½" steel webbed "L" bracket to simulate installation mounting. The set up for this experiment is shown in Figure 61.

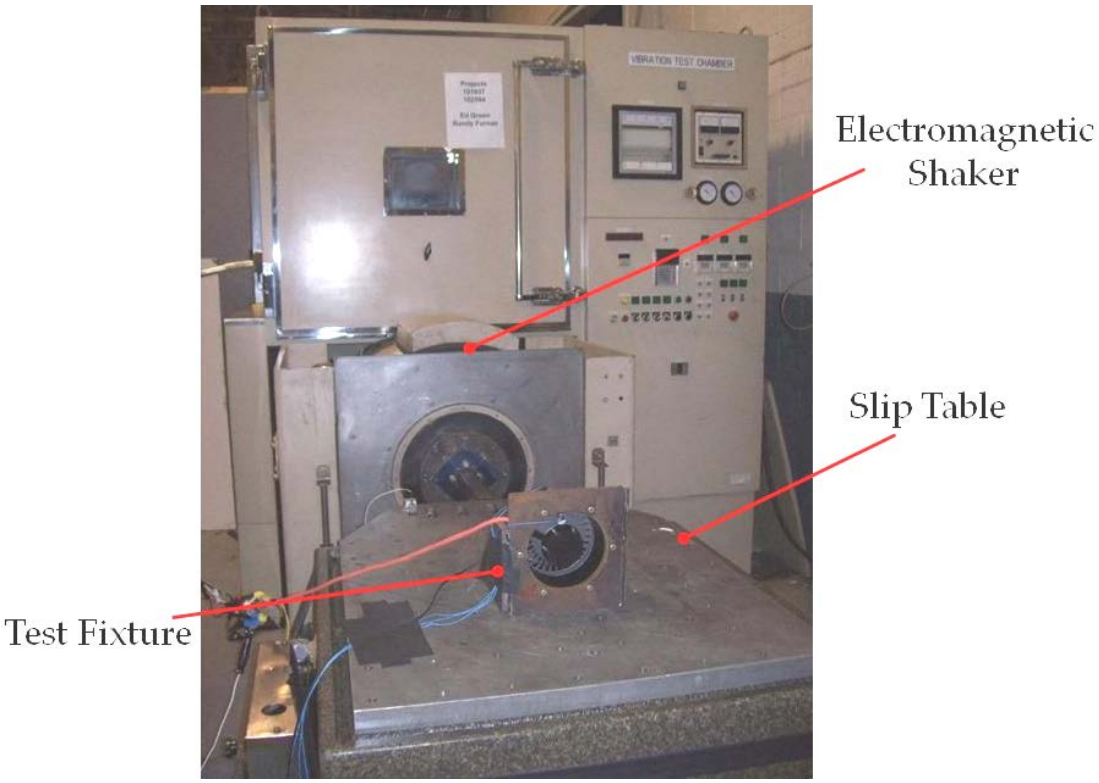

Figure 61. Electromagnetic Shaker Table and EMIC Model F-2000-BC-E07.

A total of twenty-seven shocks were imparted: three different types of shocks, three times each in succession, in three separate orthogonal directions. The directions of the shocks were axial, vertical, and lateral. Fan responses to the three shock inputs are shown in Figures 62 through 64; they show the response to a lateral ballistic shock, lateral gun firing shock, and lateral road load shock. Shock 1, 2, and 3 represent the three consecutive shocks. Figure 62 shows a filtered ballistic signal and the amplitude of the ballistic shock going slightly above 50 g but remains within the specified limits. Figures 63 and 64 show unfiltered signals for the gun firing and road load shock, respectively. As can be seen in these responses, there is a better control on the amplitude versus the pulse width of the shock. After shock testing, the fan was tested and showed no adverse effects in motor or aerodynamic performance.

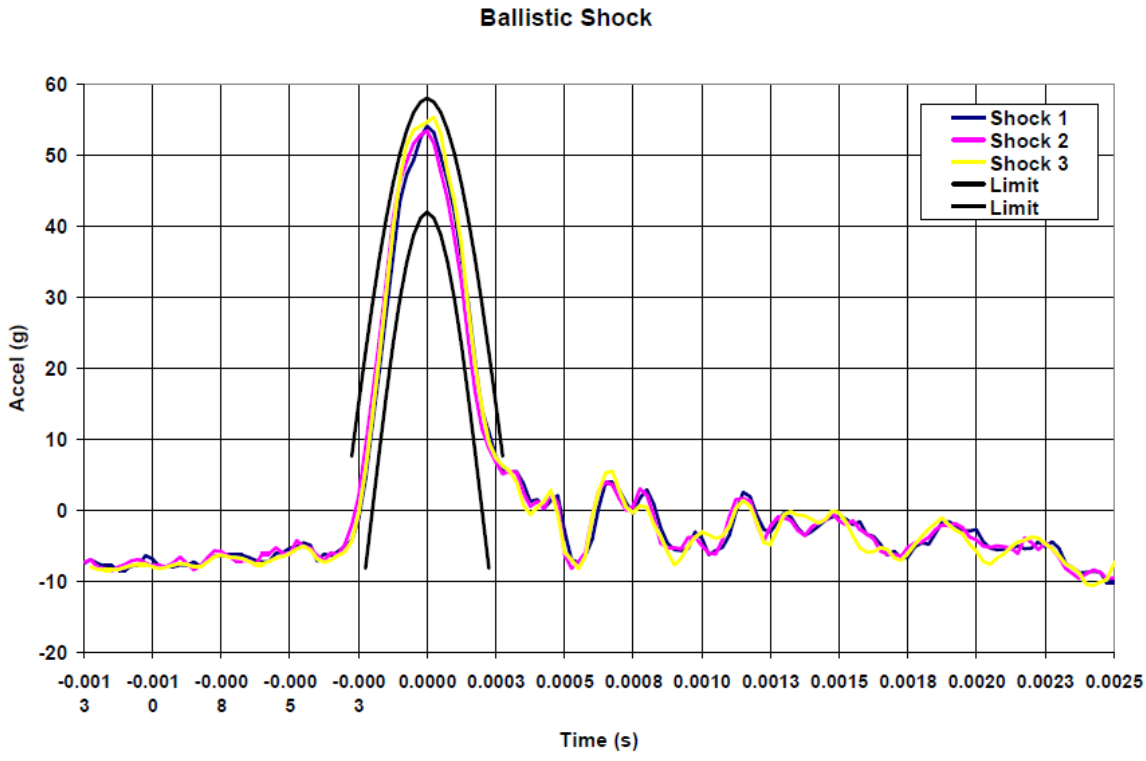

Figure 62. Fan Response to Ballistic Shock in the Lateral Direction.

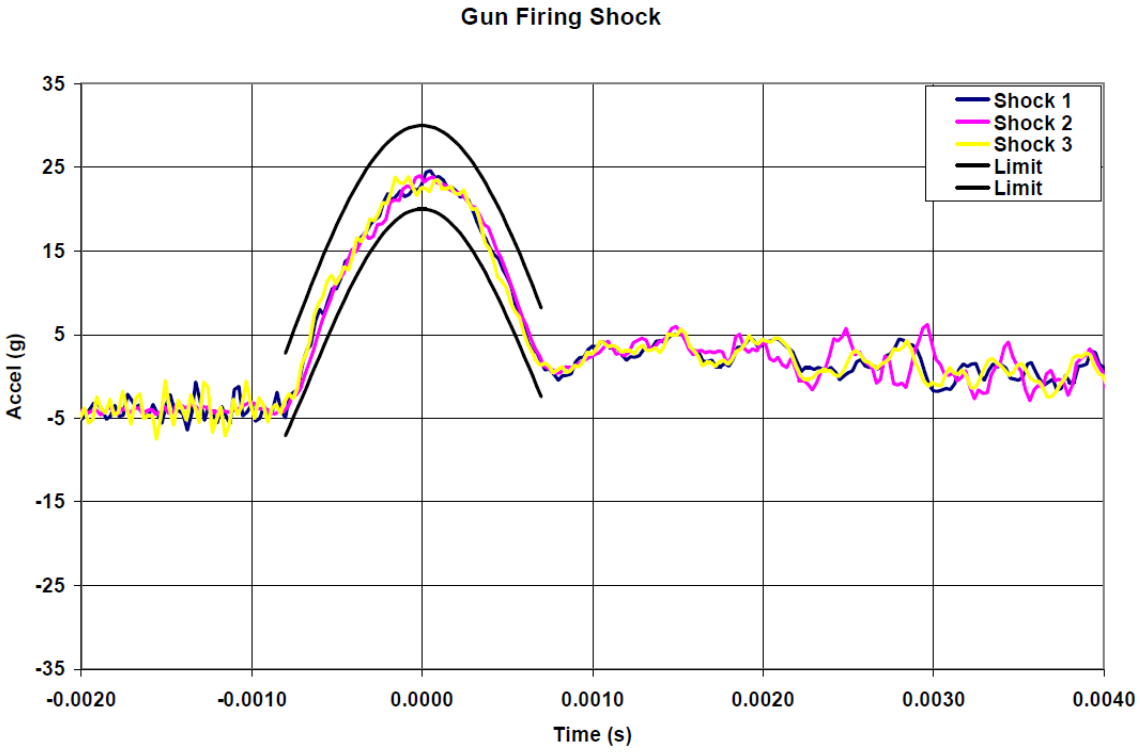

Figure 63. Fan Response to Gun Firing Shock in the Lateral Direction.

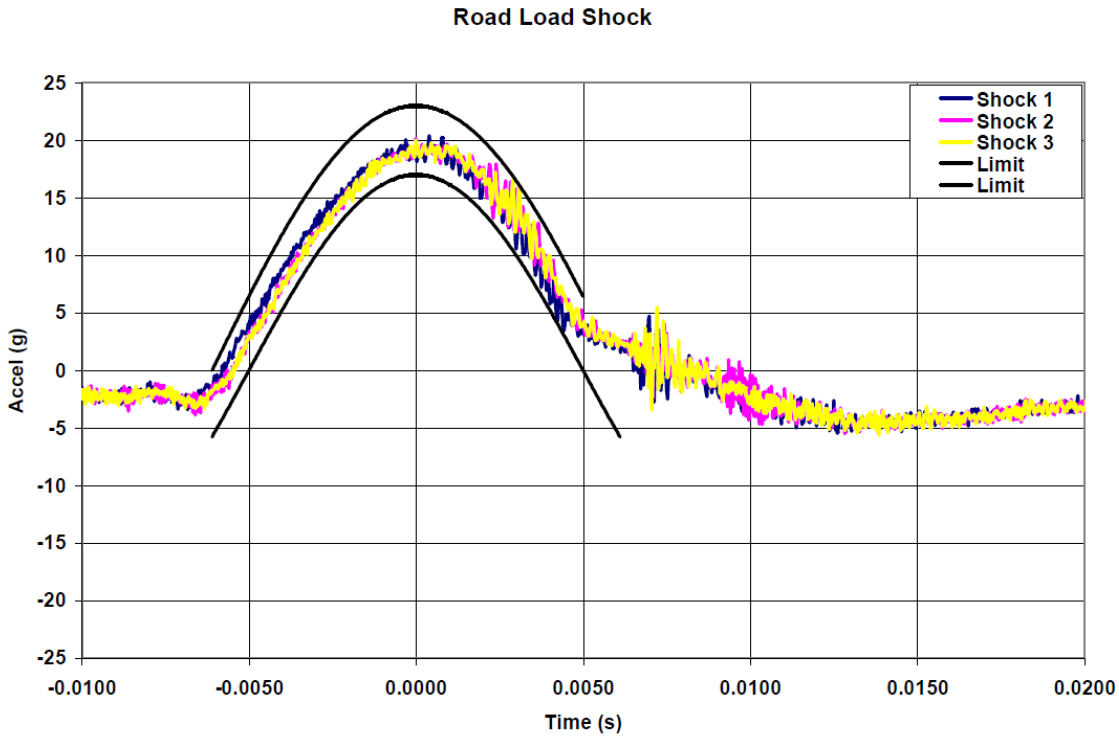

Figure 64. Fan Response to Road Load Shock in the Lateral Direction.

5.2.1 Fan Inspection After Shock Loading

During teardown inspection of the fan, the minimum clearance measured between the impeller blade tips and the shroud inner surface was 0.013 inches. The blade tips showed signs of scraping at the trailing edges where the anodized surface was grazed and aluminum was exposed; Figure 65 shows a picture of the impeller during inspection. The fan shroud had a corresponding contact line expanding in an arc of approximately 90°, as shown in Figure 66. The scrape appears to be on the surface, with no significant depth. It appears that the contact was light with no adverse effects on fan performance. There was no noticeable mark 180° at the shroud entrance region as one would expect. Fasteners on the assembly did not show any signs of loosening due to the multiple shocks.

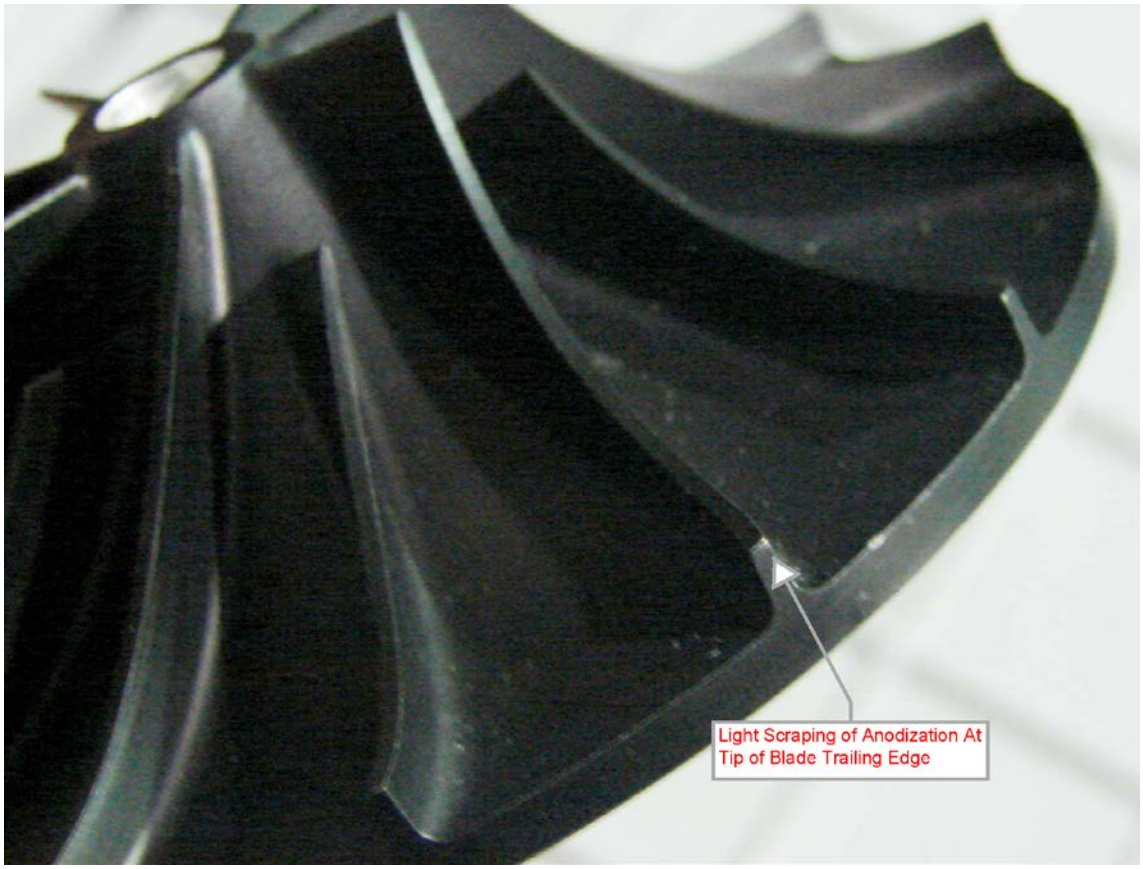

Figure 65. Light Scraping on the Fan Impeller.

Figure 66. Light Scrape Mark on Fan Shroud.

The complete rotor assembly was also sent to the bearing manufacturer for inspection. The front and rear bearings were removed and disassembled for full inspection. Both bearings showed false brinelling with no discernible depth present, as well as a typical amount of out of roundness on the ball traces. Both the balls and the retainers remained in good condition. Figure 67 shows a photo from the inspection process where axial brinells can be spotted.

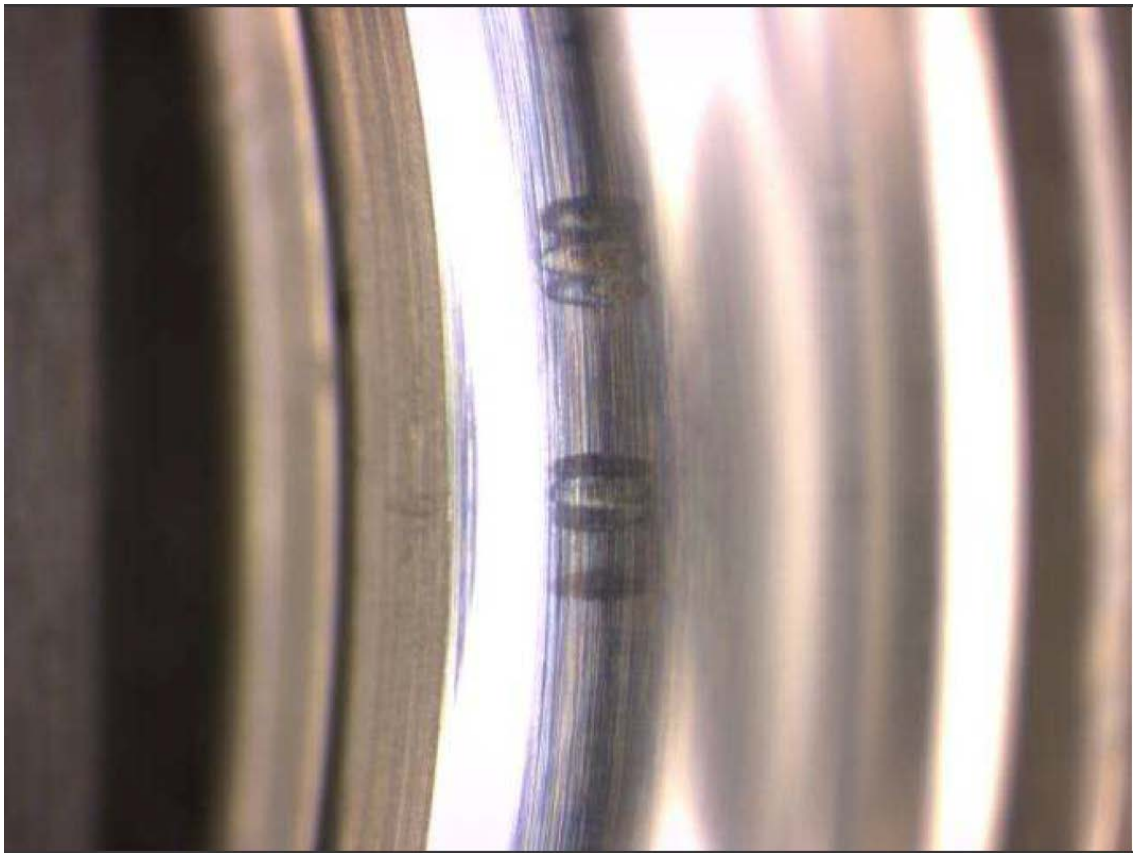

Figure 67. Inspection of Bearing Rings Showing Axial Brinells.

5.3 Summary of Chapter 5

The total calculated radial and axial closure of tip clearance is 0.0042 and 0.0034 inches respectively. These are values for the ballistic shock for which the fan components showed the largest deformation from the shock response. The radial closure was calculated at the entrance of the fan shroud near the blade's leading edges and the axial closure was calculated at the blades trailing edges. The measured minimum radial clearance calculated before experimental shock testing was 0.013 inches. There is indication of blade contact against the shroud; however, shock analyses and impeller thermal analysis results account for closure of 32.3% of the measured tip clearance. From inspection of the bearing rings on the front bearing housing, the axial brinells on the race shoulder indicate there was significant axial displacement of the bearing balls. This bearing deformation is believed to account for most of the remaining 67.8% of tip clearance

closure and contact with the fan shroud. Thermal effects could also have contributed to increased deformations, increased clearances, and loosening of shrink fits for parts with dissimilar metals, such as the motor support and the bearing housings.

CHAPTER 6

CONCLUSION

This study of shock loading includes a new graphical representation of shock response to pulse width variation through the finite element method. It is a great new tool for understanding the sensitivity of any structure to a particular pulse width of a shock input. Three different case studies were dissected and they all show the same pattern; when the input has a similar time to maximum acceleration as the natural period of the structure, the amplitude of the response is relatively large. Furthermore, using Ansys to solve FEA models offered an opportunity to study and efficiently solve complex analyses, as is the case with rotational machinery. In these types of cases, such as the Baseline Impeller case study, we have structures experiencing centrifugal and impulse loading and responding with a great variety of blade and disk modes. In this case study, the Full Method and the Mode Superposition Method are explored along with their strengths and complexities and re-introduced as tools for current and future practicing engineers.

Providing the background for this report, Chapter 3 includes a great correlation between analytical and experimental results, where the Euler-Bernoulli theory and finite element analysis are used to solve modal and shock loading of cantilevered beams. This knowledge is used in Chapter 4 of this report where blades of the baseline impeller are modeled as cantilevered beams for extracting the mode shapes and natural frequencies, a process that is currently being used in the preliminary design of bladed impellers. In the last chapter, FEA and classical theory are used to analyze a mixed flow fan undergoing shock loading; both the Full Method and the Mode Superposition Method were utilized to help in understanding how real systems respond to these types of inputs.

REFERENCES

[1] Lee, Huei-Huang. *Finite Element Simulations with ANSYS Workbench 14.* Mission: SDC Publications, 2012. Print.

[2] Szuladzinski, Gregory. *Formulas for Mechanical and Structural Shock and Impact*. Boca Raton: Taylor and Francis Group, LLC, 2010. Print.

[3] Inman, Daniel J. *Engineering Vibrations*. 2nd ed. Upper Saddle River: Prentice-Hall, Inc., 2001. Print.

[4] Repetto, C. E., Roatta, A., Welti, R. J. "Forced Vibrations of a Cantilever Beam." European Journal of Physics 33 (2012): 1187-1195. Print.

[5] Haukaas, Terje. "Euler-Bernoulli Beams." *University of British Columbia,* Nov. 2012. Web. 02 Mar. 2014.

[6] Siscribd. "Transverse Vibration of a Cantilever Beam." *Scribd* 08 Aug. 2012. Web. 02 Mar. 2014.

[7] Whitney, Scott. "Vibrations of Cantilever Beams: Deflection, Frequency, and Research Uses." *University of Nebraska-Lincoln,* 23 Apr. 1999. Web. 13 Dec. 2013.

[8] Sadd, M. H. *Wave Motion and Vibration in Continuous Media*. Kingston: University of Rhode Island, 2009. Print.

[9] Majkut, Leszek. "Free and Forced Vibrations of Timoshenko Beams Described by Single Difference Equations." *Journal of Theoretical and Applied Mechanics* 47.1 (2009): 193-210. Print.

[10] Tongue, Benson H. *Principles of Vibration.* New York: Oxford University Press, Inc, 1996. Print.

[11] Park, K. C. "Appendix C. Analytical Natural Vibration Modes and Mode Shapes of a Cantilever Beam." *University of Colorado,* 12 Feb. 2002. Web. 05 Mar. 2014.

[12] Yang, Bingen. *Stress, Strain, and Structural Dynamics: An Interactive Handbook of Formulas, Solutions, and Matlab Toolboxes*. San Diego: Elsevier Inc., 2005. Print.

[13] Soedel, Werner. *Sound and Vibration of Positive Displacement Compressors.* Boca Raton: CRC Press, 2006. Print.

[14] ANSYS, Inc. *Ansys Mechanical APDL Structural Analysis Guide*. Release 14.5. Canonsburg: SAS IP, Inc., 2012. Print.

[15] J. Luo, D. W. Shu, B. J. Shi, and B. Gu. "The Pulse Width Effect on the Shock Response of the Hard Drive Disk." *International Journal of Impact Engineering* 34 (2007): 1342-1349. Print.

[16] Rubin, Sheldon. *Shock and Vibration Handbook.* 2nd ed. Ed. Cyril M. Harris and Allan G. Piersol. New York: McGraw-Hill, 2002. Print.

[17] Rolling Bearing Catalog. CAT.No. E1102j ed. Japan: NSK Ltd., 2005. Print.

[18] Juvinal, Robert C. and Marshek, Kurt M. *Fundamentals of Machine Component Design.* 3rd ed. Hoboken: John Wiley & Sons, Inc., 2000. Print.

[19] Puttock, M. J. and Thwaite, E. G. "Elastic Compression of Spheres and Cylinders at Point and Line Contact.". *Commonwealth Scientific and Industrial Research Organization, Austrailia* National Standards Laboratory Technical Papter No. 25 (1969): 1-64. Print.

[20] Alexander, J. Edward. "Shock Response Spectrum - A Primer." *Sound and Vibration* June (2009): 6-14. Print.

[21] Stapp, J.P. "Effects of Mechanical Force on Living Tissues." *Journal of Aviation Medicine* 26.4 (1955): 268-88. Print.

[22] Viano, David C. and King, Albert I. *Biomechanics: Principles and Applications*. 2nd ed. Ed. Donald R. Peterson and Joseph D. Bronzino. Boca Raton: Taylor & Francis Group, LLC, 2008. Print.

[23] Mohammadi, S. and Hassanirad, A. "Applied and Theoretical Cantilever Beam Free Vibration Analysis." World Academy of Science, Engineering and Technology 61.305 (2012): 1619-1622. Print.

[24] Haran, Shivan. "Second Order Systems: Vibrating Cantilever Beams." *Arkansas State University: ME 3504 Process Monitoring and Control*, 03 Nov. 2005. Web. 02 Mar. 2014.

APPENDIX A: MATLAB CODE

Matlab Code for Determination of Eigen Values and Eigen Functions of a Cantilevered Beam; based on a code written by K.C. Park.

```
%input data
%rho    : density
%E      : Young's modulus
%L      : Length of the beam
%w      : width of cantilever beam
%t      : thickness
%p      : vertical or lateral force
%y      : vertical displacement due to force P
%a_x    : cross-sectional area of the beam
%rho_l  : linear density is calculated
%v      : volume
%m      : mass
%mode   : natural frequency calculated in rad/sec then converted to hertz

L = input ('enter the beams length in meters:')
w = input ('enter the beams width in meters:')
t = input ('enter the beams thickness in meters:')
E = input ('enter the beams modulus of Elasticity in N/m^2:')

rho = input ('enter the beams density in Kg/m^3:')
a_x = w*t;
v = L*w*t;
rho_L = rho*a_x;

I = w*t^3/12;
m = rho*v;
EI=E*I;

modes = zeros (3,1);
modeshapes=zeros(3,40);

betaL = [1.875, 4.694, 7.856];

%for loop for the three modes
for i = 1:3;
   modes (i) = betaL (i)^2*sqrt(EI/(rho_L*L^4));
   modes (i) = modes (i)/(2*pi);
   modes (i)

%coefficients for computing mode shapes
a1 = sin(betaL(i)) + sinh(betaL(i));
a2 = cos(betaL(i)) + cosh (betaL(i));

%CALCULATING THE Y VALUES OF THE MODE SHAPES
x = 0 ;
%how the x values will be incremented:
increment = L/40;
```

```
%beta is betaL/L and is part of the original formula
beta = betaL(i)/L;

%this j loop runs 40 times and completes, for every run of the i loop
for j=1:40
   y = a1*(cosh(x) - cos(x))- a2*(sinh(x) - sin(x)) ;
   x = x + (beta)*increment;
   modeshapes(i,j) = y;
end;
end;

%x values denoted by a beam span
beamspan = (1:40)*(L/40);

%Plot of the First Mode Shape
figure (1);
ymax = max (abs (modeshapes(1,:)));
plot (beamspan, modeshapes(1,:)/ymax);
grid on;
ylabel ('Modeshape Amplitude');
xlabel ('Beam Span')
title ('Mode Shape of the First Mode of a Cantilever Beam');
legend([' First Mode Frequency =', num2str(modes(1))]);

%Plot of the Second Mode Shape
figure (2);
ymax = max (abs (modeshapes(2,:)));
plot (beamspan, modeshapes(2,:)/ymax);
grid on;
ylabel ('Modeshape Amplitude');
xlabel ('Beam Span')
title ('Mode Shape of the Second Mode of a Cantilever Beam');
legend([' Second Mode Frequency =', num2str(modes(2))]);

%Plot of the Third Mode Shape
figure (3);
ymax = max (abs (modeshapes(3,:)));
plot (beamspan, modeshapes(3,:)/ymax);
grid on;
ylabel ('Modeshape Amplitude');
xlabel ('Beam Span')
title ('Mode Shape of the Third Mode of a Cantilever Beam');
legend([' Third Mode Frequency =', num2str(modes(3))]);

%figure 4 below show values for deflection, that are Not Normalized
figure (4);
plot (beamspan, modeshapes(1,:));
grid on;
ylabel ('modeshape amplitude');
xlabel ('beam span')
title ('Mode Shape of the First Mode of a cantilever beam Not Normalized');
legend([' first mode frequency =', num2str(modes(1))]);
```